5-4-2018

Development of Microscopy Systems for Super-Resolution, Whole-Slide, Hyperspectral, and Confocal Imaging

Kaikai Guo
University of Connecticut - Storrs, kaikai.guo@uconn.edu

Development of Microscopy Systems for Super-Resolution, Whole-Slide, Hyperspectral, and Confocal Imaging

Kaikai Guo, PhD

University of Connecticut, 2018

Optical microscope is an important tool for researchers to study small objects. In this thesis, we will focus on the improvement of traditional microscope systems from several aspects including resolution, field of view, speed, cost, compactness, multimodality. In particular, we will investigate computational imaging methods that bypass the limitations with traditional microscope systems by combining the optical hardware design and image processing algorithm. Examples will include optimizing illumination strategy for the Fourier ptychography (FP), developing field-portable high-resolution microscope using a cellphone lens, investigating pattern-illuminated FP for fluorescence microscopy, demonstrating multimodal microscopic imaging with the use of liquid crystal display, achieving fast and accurate autofocusing for whole slide imaging system.

Development of Microscopy Systems for Super-Resolution, Whole-Slide, Hyperspectral, and Confocal Imaging

Kaikai Guo

B.E., Huazhong University of Science and Technology, 2011

M.E., Zhejiang University, 2014

A Dissertation

Submitted in Partial Fulfillment of the

Requirements for the Degree of

Doctor of Philosophy

At the

University of Connecticut

2018

APPROVAL PAGE

Doctor of Philosophy Dissertation

Development of Microscopy Systems for Super-Resolution, Whole-Slide, Hyperspectral, and Confocal Imaging

Presented by
Kaikai Guo, B.E., M.E.

Major Advisor_____
Dr. Guoan Zheng

Associate Advisor _____
Dr. Kazunori Hoshino

Associate Advisor _____
Dr. Patrick D. Kumavor

University of Connecticut
2018

Acknowledgments

This work would not be possible without the help of the Smart Imaging Lab at UConn. First of all, I would like to thank Dr. Guoan Zheng for the opportunity to work in his lab. I am deeply grateful to his guidance, insights and advices on my research. I really enjoy the discussion with him for all kinds of innovative ideas. I also want to acknowledge Dr. Kazunori Hoshino and Dr. Patrick D. Kumavor for their discussions and suggestions on this work.

Many thanks to the members of the Smart Imaging Lab, Siyuan Dong, Zichao Bian, Radhika Shiradkar, Pariksheet Nanda, Jun Liao, Shaowei Jiang, Zhe Wang, Yutong Jiang for their help throughout my work at UConn. I would like to thank Dr. Zibang Zhang, You Zhou, and Dr. Pan Feng for helpful discussions. I also want to thank all my wonderful friends at UConn, Qiuchen Dong, Hasan Fiaz, Xu Zhai, Mingze Sun, Longtu Cheng, Jianan Lin, Zhen Cao and Yang Gao.

Lastly, I want to express my gratitude to my parents and my sisters for their support throughout the years. I would like to thank my dearest wife for her patience and encouragement. This dissertation is dedicated to them.

Contents

Acknowledgments iv

Chapter 1 Introduction to optical microscope 1

1.1 Traditional microscope and limitations 1

1.2 Novel imaging systems 3

1.3 Research objectives 6

Bibliography 7

Chapter 2 Fourier ptychography 9

2.1 Background 9

2.2 Epi-illumination Fourier ptychography 14

2.3 Dark-field Fourier ptychography 17

Bibliography 18

Chapter 3 Sampling optimization of Fourier ptychography 21

3.1 Background 21

3.2 Choice of scanning sequence for Fourier ptychography 24

3.3 Non-uniform sampling pattern for Fourier ptychography 27

3.4 Design of Fourier ptychographic illuminator 31

3.5 Discussion 36

Bibliography 37

Chapter 4 Field-portable Fourier ptychographic microscope 39

4.1 Background 39

4.2 System design of the FPscope 41

4.3 System characterization of the FPscope 44

4.4 Demonstration of the FPscope with biological samples 46

4.5 Discussion 47

Bibliography 48

Chapter 5 Imaging through turbid layer via translated unknown speckle illumination 50

5.1 Background 51

5.2 Modeling and simulation 53

5.3 13-fold resolution gain through turbid layers 59

5.4 Wide-field, high-resolution fluorescence imaging 61
5.5 Discussion 63
Bibliography 64
Chapter 6 Higher dimensional imaging with multiplexed structured illumination 67
6.1 Background 67
6.2 Multiplexed structured illumination 68
6.3 Higher dimensional imaging demonstration 73
6.4 Discussion 75
Bibliography 76
Chapter 7 Multilayer fluorescence imaging on a single-pixel detector 78
7.1 Background 78
7.2 Multilayer single-pixel imaging scheme and simulation results 79
7.3 Experimental validation 83
7.4 Discussion 86
Bibliography 87
Chapter 8 Multimodal imaging with a liquid crystal display 89
8.1 Background 89
8.2 Microscope illumination with LCD 92
8.3 Multimodal imaging demonstration 95
8.4 Discussion 97
Bibliography 98
Chapter 9 Autofocusing for whole slide imaging system 100
9.1 Background 100
9.2 Instant focal plane detection using pinhole-modulated cameras 103
9.3 Unveiling sample's tomographic structure using the phase correlation curve 105
9.4 Mechanical design and high-throughput gigapixel imaging 106
9.5 Discussion 109
Bibliography 110

Chapter 1 Introduction to optical microscope

1.1 Traditional microscope and limitations

Modern optical microscopes usually consist of a condenser lens for sample illumination, an infinity-corrected objective lens for light collection, a tube lens for image magnification, and a CCD camera for image recording. There are several limitations with the modern microscopes, including the trade-off between resolution and field-of-view, geometry and chromatic aberrations, focusing problem due to the shallow focus, lost phase information by detector.

Resolution: For an aberration-corrected microscope system, the objective lens acts like a low-pass filter. Its cutoff frequency is determined by the numerical aperture (NA) which characterizes the light-collection ability. As a result, an infinitely small point is not imaged to a point but rather to a diffraction-limited distribution. This distribution is called the point spread function (PSF) of the imaging system which describes the optical resolution. For incoherent imaging system, the resolution is r = 0.61 * lambda / NA, where lambda is the wavelength.

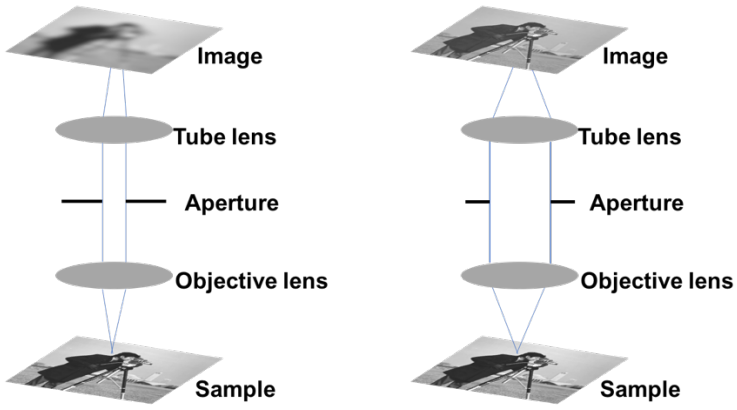

Figure 1-1: Low-pass filtering of a microscope system, the cut-off frequency is determined by the numerical aperture of the objective lens. Higher numerical aperture objective lens has better resolution (right).

Magnification: Another important parameter is magnification. For an infinity-corrected microscope system, the magnification factor is the ratio of the tube lens focal length to the objective focal length. Microscope systems using CCD or CMOS cameras to record image should satisfy the sampling theorem. It means the effective camera pixel size should be smaller than a half of the optical resolution otherwise aliasing problem occurs. The field-of-view of the microscope system determines the area of the sample that can be imaged onto an imaging sensor.

Field-of-view: After the magnification is chosen, the field-of-view is simply the imaging sensor size divided by the magnification factor. In conventional microscope systems, a higher NA objective lens requires a higher magnification factor results in a smaller field-of-view. For example, a standard 20X objective lens (MPLN 20X, 0.4 NA, Olympus) has a resolution of 0.8 microns and a field-of-view with 1.1 mm diameter. This trade-off between resolution and field-of-view is a problem for pathology applications which require a high NA of 0.75 and a large field-of-view with 15 mm diameters.

Depth-of-field: As the system resolution increases, the focusing problem merges because of the shallow depth-of-field. The depth-of-field of an imaging system is the distance along the optical axis that we can move the sample from precise focus and still get sharp image. In photography, shallow focus created by large aperture (low f-number) generates images with certain subjects in-focus and the rest out-of-focus. This is a pleasing effect to human eye because background blur puts the viewer's focus on the main subject in the foreground. In microscopy, the shallow depth-of-field makes it difficult to precisely focus the sample which is usually not perfectly flat at different areas across the sample plane. A higher NA objective lens usually has smaller depth-of-field. As an example, an objective lens with 0.75 NA used in digital pathology applications usually has a depth-of-field less than 1 microns. The shallow focus requires a Z stage with high performance and precise algorithms to find the best focal position.

Phase: Current optical detector can only measure the intensity of light field because the light oscillates too fast for detector to response. The lost phase however can reveal important information about the sample and imaging system. Transparent samples do not change the intensity of light passing through them but introduce phase delays due to variations in thickness and index of refraction. Measuring phase information allows physical properties of samples, such as unstained biological cells and tissues, to be inferred. The recovered phase also enables direct removal of system aberrations and digitally refocus an image to different plane along the optical axis by back-propagating the complex light field.

1.2 Novel imaging systems

In the section 1.1, we discussed the limitations of the conventional microscope and important parameters regarding the system design. Here, we will briefly review several new imaging techniques developed over the past years, aiming to address the microscope system limitations. Most of these imaging techniques depend on the combination of optical hardware and computational algorithm. The acquired images are usually post-processed by taking into account the property of the optical system to generate a better result with additional information. The 2014 Nobel Prize in Chemistry was awarded to super-resolved fluorescence microscopy which combines illumination design, fluorescent labeling and computational recovery.

Diffractive imaging is a technique to capture high-resolution image without using lens. Ptychography uses coherent illumination and captures multiple diffraction patterns at far field by laterally scanning the specimen [1]. The diffraction patterns are related to the exit wave emanating from the specimen by Fourier transform. The detector only records the intensity information that is proportional to the square of the modulus part of the complex diffraction pattern. In order to solve the phase problem, we can use an iterative phase retrieval algorithm call the ptychography iterative engine (PIE) to recover amplitude and phase part

of the complex image of the specimen with high-resolution. In addition, the illumination function, the scan position can also be recovered from the dataset [2-3].

Digital in-line holography is also a lensless imaging technique that is able to recover both phase and amplitude information simultaneously [4]. The specimen is placed between a partial coherent light source and an image recording detector. The measurement is an interference pattern between the wave scattered by sample and the un-scattered reference light. The complex image of a sample can be reconstructed through phase retrieval algorithm by digitally propagating between sample plane and the detector plane using angular spectrum approach [5-7].

Structured-illumination microscopy (SIM) enhances the spatial resolution by projecting non-uniform intensity patterns on a sample [8]. These non-uniform patterns modulate otherwise undetectable high-resolution information to low-resolution measurements. Observed SIM image contains superimposed high-frequency and low-frequency information. By using three illumination patterns with shifted phase, it is possible to computationally separate those frequency components and shift them back to the correct position in the Fourier domain. The reverse Fourier transform will generate the final image with much more resolution information [9-11].

Saturated structured-illumination microscopy (SSIM) is based on the nonlinear dependence of the emission rate of fluorophores on the intensity of the excitation laser [12-13]. By applying a sinusoidal illumination pattern with a peak intensity close to that needed to saturate the fluorophores, one retrieves nonlinear moiré fringes. The fringes contain high order spatial information that can be extracted by computational techniques. Once the information is extracted, a super-resolution image beyond the diffraction limit is recovered.

Stimulated emission depletion microscopy (STED) uses two laser pulses, the first one for raising the fluorophores to their fluorescent state and the second one for de-excitation of fluorophores by stimulated

emission. Due to the non-linear dependence of the stimulated emission rate on the intensity of the STED beam, all the fluorophores around the focal excitation spot will be in their off state (the ground state of the fluorophores). By scanning this focal spot across the sample, one retrieves the 2D image. The size of the excitation focal spot can theoretically be infinitely small by raising the intensity of the STED pulse [14-15].

Photoactivated localization microscopy (PALM) [16] or Stochastic optical reconstruction microscopy (STORM) [17] is another type of super resolution method that utilizes sequential activation and localization of photoswitchable fluorophores to create a precise location map of fluorophores. During imaging, only a small subset of fluorophores is activated at any given time, as such, the position of each fluorophore can be determined with high precision by locating the centroid of the single-molecule.

Confocal microscopy is an optical imaging technique for increasing the optical resolution and recovering the three-dimensional structures. Confocal microscopy uses point illumination and a pinhole detector at the image plane to eliminate out-of-focus light [18]. As only light produced by fluorescence very close to the focal plane can be detected, the image's optical resolution, particularly in the sample depth direction, is much better than that of wide-field microscopes. The shallow depth-of-field makes it particularly good at 3D imaging and surface profiling of samples. Confocal microscopy captures multiple 2D images at different depths by scanning the sample along z-direction and computer algorithm merges them into a 3D image.

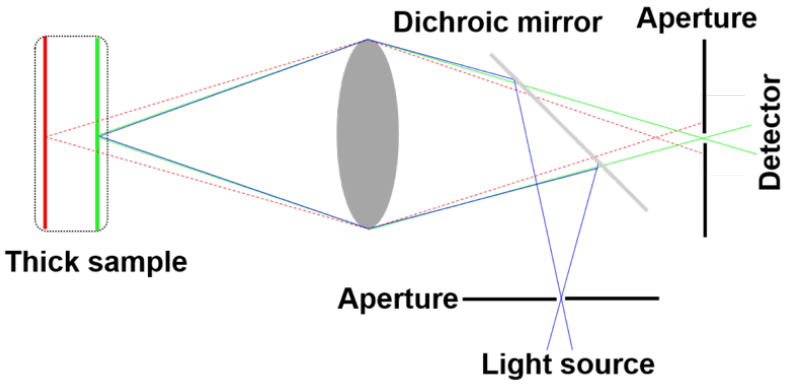

Figure 1-2: The principle of confocal microscopy. The out-of-focus light (red) is blocked by the pinhole detector.

1.3 Research objectives

Fourier ptychography is a technique to generate both high-resolution and large field-of-view image by capturing multiple low-resolution images from different illumination angles and combining information from different spatial spectrum bands in Fourier domain. We propose a non-linear sampling approach in Fourier domain to shorten the image acquisition time. We will also extend the FP imaging reconstruction algorithm for fluorescence imaging by using non-uniform illumination pattern which moves high frequency information into the low-pass filter band of the optics. Unlike the conventional structured-illumination microscopy (SIM) system, FP can jointly recover the high-resolution object image and the illumination pattern. We will demonstrate the use of FP for 3D imaging, imaging through turbid media and multilayer fluorescence imaging with single-pixel settings. We will also develop a field-portable high-resolution microscope using a low-cost cellphone lens based on FP image reconstruction algorithm. By combining low-end optics with signal processing, we can achieve high-resolution, compact, light-weight portable microscope which could benefit remote clinics and be used in resource-limited environment.

We propose to develop a programmable condenser lens for active control of the microscopy illumination. We will use a liquid crystal display (LCD) as a transparent spatial light modulator and place it at the back focal plane of the condenser lens. By setting different binary patterns on the display, we demonstrated the use of LCD based illumination for multimodal imaging, including bright-field microscopy, darkfield microscopy, phase-contrast microscopy, polarization microscopy, 3D tomographic imaging. For bright field microscopy, we can display a circular pattern and the pixel transmission is turned off outside the circle. We can adjust the diameter of the pattern to match to different NAs of the objective lenses. For the phase-contrast imaging, we can display two complementary semicircular patterns at the

liquid crystal display, capture two corresponding sample images, and get the difference between them. The programmable condenser can also be used to perform 3D tomographic imaging by showing a scanning aperture on the LCD to illuminate the sample with different incident angles. The corresponding captured images then are used to recover the 3D image with backpropagation algorithm.

Whole-slide-imaging (WSI) system generates high-resolution images of entire histology slides by scanning the sample to different x-y positions and acquiring sample images using a high-resolution objective lens at each position. One important aspect of whole slide imaging systems is to maintain the sample at the optimal focal position while performing high-speed scanning. We will study a phase-detection based autofocusing method and develop a low-cost high-throughput WSI system by adapting an add-kit to existing microscope.

Bibliography

[1] Plamann, T.; Rodenburg, J. M. (1998-01-01). "Electron Ptychography. II. Theory of Three-Dimensional Propagation Effects". Acta Crystallogr. A. 54 (1): 61–73.

[2] Humphry, M.J.; Kraus, B.; Hurst, A.C.; Maiden, A.M.; Rodenburg, J.M. (2012). "Ptychographic electron microscopy using high-angle dark-field scattering for sub-nanometre resolution imaging". Nature Communications. 3 (370): 730.

[3] Rodenburg, J. M.; Faulkner, H. M. L. (2004). "A phase retrieval algorithm for shifting illumination". Applied Physics Letters. 85 (20): 4795.

[4] W. Xu, M. Jericho, I. Meinertzhagen et al., “Digital in-line holography for biological applications,” Proceedings of the National Academy of Sciences of the United States of America, vol. 98, no. 20, pp. 11301, 2001.

[5] J. Garcia-Sucerquia, W . Xu, S. K. Jericho et al., “Digital in-line holographic microscopy,” Applied optics, vol. 45, no. 5, pp. 836-850, 2006.

[6] L. Repetto, E. Piano, and C. Pontiggia, “Lensless digital holographic microscope with light-emitting diode illumination,” Optics letters, vol. 29, no. 10, pp. 1132-1134, 2004.

[7] O. Mudanyali, D. Tseng, C. Oh et al., “Compact, light-weight and cost-effective microscope based on lensless incoherent holography for telemedicine applications,” Lab on a Chip, vol. 10, no. 11, pp. 1417, 2010.

[8] John M. Guerra (1995). “Super-resolution through diffraction-born evanescent waves,” App. Phys. Lett. 66. p. 3555.

[9] Bailey B, Farkas DL, Taylor DL, Lanni F (November 1993). “Enhancement of axial resolution in fluorescence microscopy by standing-wave excitation,” Nature. 366 (6450): 44–8.

[10] Gustafsson MG (May 2000). “Surpassing the lateral resolution limit by a factor of two using structured illumination microscopy,” J Microsc. 198 (Pt 2): 82–7.

[11] Gustafsson MG (September 2005). "Nonlinear structured-illumination microscopy: Wide-field fluorescence imaging with theoretically unlimited resolution," Proc. Natl. Acad. Sci. U.S.A. 102 (37): 13081–6.
[12] Gustafsson, M. G. L. (2005). "Nonlinear structured-illumination microscopy: Wide-field fluorescence imaging with theoretically unlimited resolution," Proceedings of the National Academy of Sciences. 102 (37): 13081–13086.
[13] John M. Guerra (1995). "Super-resolution through diffraction-born evanescent waves," App. Phys. Lett. 66 (26): 3555.
[14] Fernandes-Suares, M.; Ting, A. Y. (2008). "Fluorescent probes for super-resolution imaging in living cells," Nature Reviews Molecular Cell Biology. 9 (12): 929–943.
[15] Huang, Bo; Bates, M.; Zhuang, X. (2009). "Super resolution fluorescence microscopy," Annual Review of Biochemistry. 78: 993–1016.
[16] S. T. Hess, T. P. K. Girirajan, and M. D. Mason, "Ultra-high resolution imaging by fluorescence photoactivation localization microscopy," Biophysical journal, vol. 91, no. 11, pp. 4258-4272, 2006.
[17] M. J. Rust, M. Bates, and X. Zhuang, "Sub-diffraction-limit imaging by stochastic optical reconstruction microscopy (STORM)," Nature methods, vol. 3, no. 10, pp. 793- 796, 2006.
[18] "Memoir on Inventing the Confocal Scanning Microscope," Scanning 10 (1988), pp128–138.

Chapter 2 Fourier ptychography

2.1 Background

Fourier ptychography (FP) is a recently developed computational imaging technique for wide-field, high-resolution microscopy [1]. The development of this technique integrates two concepts in classical optics: aperture synthesizing [2-8] and phase retrieval [9-17]. In a typical implementation of FP, we use angle-varied plane waves for sample illumination and a low numerical aperture (NA) objective lens for image acquisition. By illuminating a 2D thin sample with different incident angles, the Fourier diffraction pattern at the back focal plane of the objective will shift to different positions. As such, part of the light field that would normally lie outside the lens's aperture can now be transmitted to the image plane. In FP, the captured intensity images corresponding to different incident angles are iteratively synthesized in the Fourier space to expand the passband (aperture synthesizing) and recover the lost phase information (phase retrieval) at the same time. The final achievable resolution of FP is determined by the synthesized passband at the Fourier space. As such, it is able to use a low-NA objective with low-magnification factor to produce a high-resolution sample image, combing the advantages of wide field of view and high resolution at the same time.

The recovery process of FP is to seek for a high-resolution complex sample solution that is consistent with many low-resolution intensity measurements. This process can be viewed as an optimization problem where one tries to minimize the difference between the generated low-resolution intensity images from the complex solution and the actual intensity measurements. Different phase retrieval algorithms can be used in this recovery process, including the semi-definite-programing-based methods and non-convex methods. Examples of semi-definite-programing-based methods include PhaseLift [15, 16] and PhaseCut [17]. This

type of methods could converge to a global optimum by a series of convex relaxations and have been demonstrated in the FP recovery process [18]. However, these methods require matrix lifting in a higher dimensional space and are generally not suitable to handle the large image dataset captured in a typical FP experiment. Examples of non-convex methods include alternating projection algorithms [10], where the solution iteratively switches between the spatial and Fourier domain. Different constraints for the solution are imposed in the iterative process, including measured magnitudes, non-negativity, finite support and etc [9, 11, 13, 14]. The alternating projection algorithms are computationally efficient but have the risk of non-convergence or reaching local optimums. Recently, Non-convex Wirtinger flow algorithm [19] has been proposed for phase retrieval. This method uses Wirtinger derivatives and gradient descent scheme to rigorously retrieve the exact complex information from a near minimal number of measurements. The Wirtinger algorithm with noise relaxation has been successfully demonstrated for FP experiments [20].

In the original FP setup [1], alternating projection algorithm was used to recover the high-resolution complex sample image. In brief, two types of constraints were applied in the recovery process: 1) in the spatial domain, the captured images were used as the magnitude constraint for the solution; 2) in the Fourier domain, the confined coherent transfer function of the objective (a circular aperture) was used as the support constraint for the solution. This confined aperture constraint was digitally panned across the Fourier space according to different illumination angles, synthesizing a large passband with high-frequency information of the sample.

The 5-step recovery process for the FP prototype setup is summarized in Fig. 2-1, where a high-resolution initial guess is generated in the Fourier domain (step 1) and sequentially updated with low-resolution intensity measurements (step 2-4). For each updating process, we first perform low-pass filtering of the initial guess using the confined coherent transfer function of the objective (step 2). The resulting complex image is called the targeted image. We then keep the phase component of the targeted image

unchanged while replace the magnitude component with the square root of the intensity measurement. The updated targeted image is then used to update the corresponding region of the high-resolution solution in the Fourier space (step 3). The updating process is repeated for all different incident angles and iterated until solution convergence (step 4 and 5).

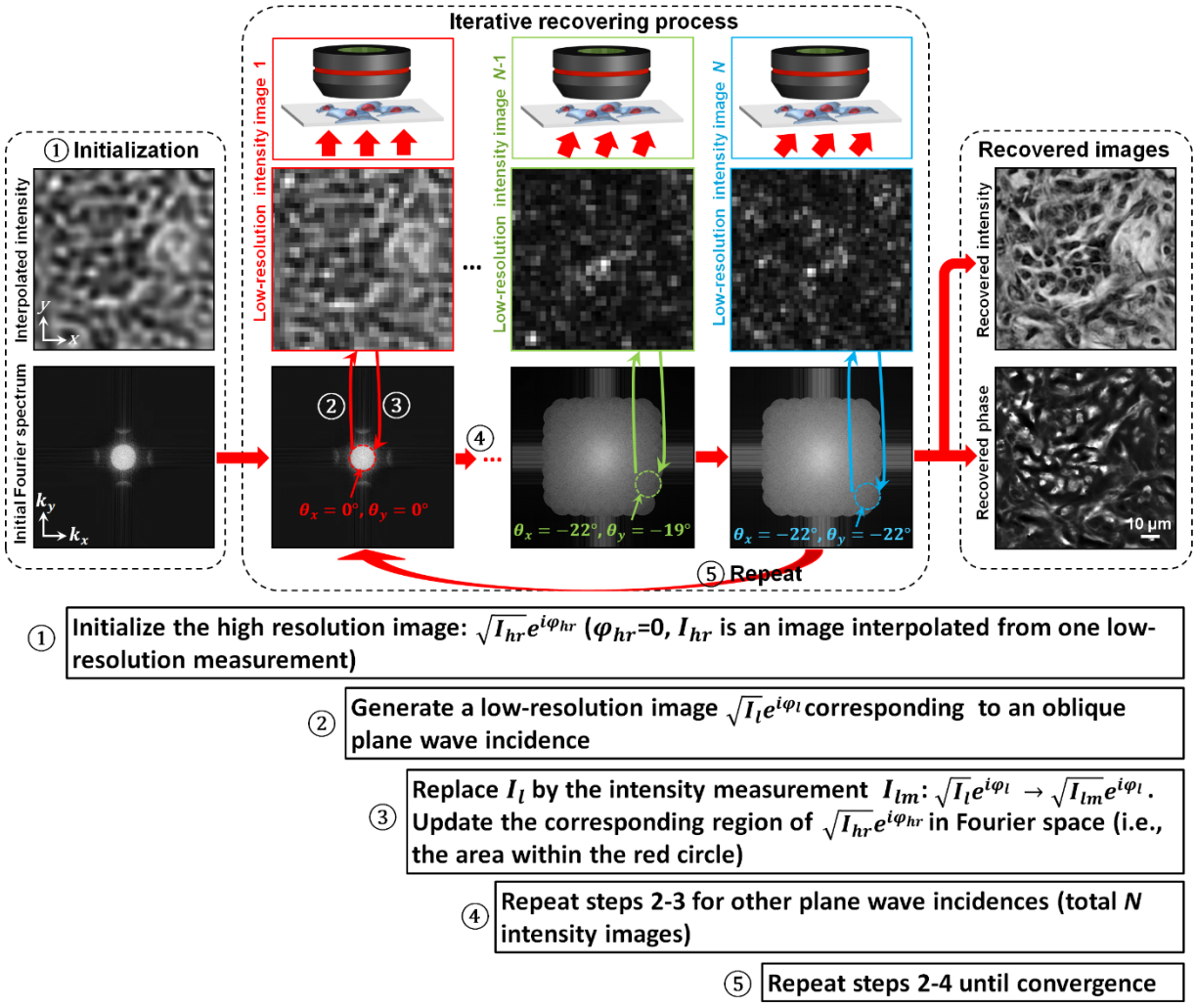

Figure 2-1: The recovery process of Fourier ptychography. The high-resolution initial guess (step 1) is sequentially updated by the low-resolution intensity measurements (step 2-4). Similar to other alternating projection methods, this process is repeated until solution convergence (step 5). Adapted from [1].

The name of 'Fourier ptychography' comes from a related imaging modality, ptychography, and here we call it real-space ptychography [21]. Real-space ptychography is a lensless phase retrieval technique that was originally proposed for transmission electron microscopy [22] and brought to fruition by Rodenburg [11, 23, 24]. It uses a focused beam for sample illumination, and the Fourier diffraction patterns are recorded at the far field as the sample is mechanically scanned to different positions. The captured Fourier diffraction patterns are then used to recover the complex sample image at the spatial domain. It is clear that both FP and real-space ptychography seek for a complex solution that is consistent with many intensity measurements. With real-space ptychography, the finite aperture support constraint is imposed in the spatial domain and the magnitude constraint is imposed in the Fourier domain. FP, on the other hand, switches the spatial domain and the Fourier domain by using a lens [1, 25, 26]. With FP, the intensity images are captured in the spatial domain and the aperture constraint is imposed by the confined coherent transfer function in the Fourier domain. To this end, FP appears as the Fourier counterpart of the real-space ptychography, justifying its name. Because of the close relationship between real-space ptychography and FP, developments of real-space ptychography can be directly applied in the FP experiments. For example, the sampling scheme [27], the coherent-state multiplexing scheme [28, 29], the multi-slice modeling approach [30, 31], and the object-probe recovering scheme [12, 32] in real-space ptychography can be directly implemented in FP experiments [21, 33-37]. We will discuss these developments in a later section. Despite the close relationship between the FP and real-space ptychography, there are several unique advantages associated with the FP scheme:

(1) By capturing images in the spatial domain, FP reduces the requirement of spatial coherence. In particular, real-space ptychography needs to maintain spatial coherence over the entire image detector. FP, on the other hand, only needs to maintain spatial coherence over the scale of the point spread function at the object plane. As such, we can use partially coherent LED illumination in FP imaging settings. This

advantage may be important for imaging modalities where high spatial coherence is difficult to achieve, such as X-ray and electron microscopy.

(2) By scanning the aperture in the Fourier domain, FP is able to recover an image with a resolution beyond the frequency limit of the employed lens. Aperture scanning in the Fourier domain can be implemented by using a simple LED array for angle-varied illumination, and thus, no mechanical scanning is needed in an optical FP platform.

(3) The FP concept can be implemented in the macroscopic photographic imaging settings, where the aperture of photographic lens naturally serves as a support constraint in the Fourier domain. By simply scanning camera over different positions, we can bypass the resolution limit set by the aperture of the photographic lens. The final achievable resolution is determined by the traveling range of the camera, not the size of the aperture [38]. Such an implementation is not possible using the real-space ptychography.

(4) In the recovery process of FP, aberrations of the employed lens can be modeled as a pupil function [34, 39]. Therefore, FP can digitally correct for unknown aberrations of an optical system. As an example, we can introduce a second-order pupil function in the recovery process to compensate for the defocus aberration. By doing so, we can extend the depth of field of a microscopy platform by ~75 folds [1]. Since aberrations can be corrected in the FP recovery process, low quality optics can also be used to achieve high-resolution imaging performance [40].

(5) The Fourier spectrum of an image typically has a very high dynamic range. The signal strength at the center of the Fourier spectrum is typically orders of magnitude higher than those at the edge. As a result, real-space ptychography requires a detector with a very high dynamic range for capturing diffraction patterns at the Fourier space. FP, on the other hand, directly captures images in the spatial domain. The overall signal strength only changes when the sample is illuminated with a different incident angle. We can, thus, simply adjust the exposure time of the detector to accommodate the change of the signal strength in

FP imaging settings [41]. In addition, the sampling overlap in FP can be adjusted in the Fourier space according to the energy level of the sample's Fourier spectrum [41, 42]. The sampling overlap for real-space ptychography, on the other hand, needs to be uniform in the spatial domain and cannot be adapted to the spatial features of the object.

2.2 Epi-illumination Fourier ptychography

Transmitted light microscope cannot handle opaque or reflective specimens such as metallic surfaces, silicon wafer, and integrated circuits. As a result, reflected light microscopes have been developed to image these specimens using an epi-illumination configuration. With the rapid development of semiconductor industry, reflected light microscope has become a vital tool for spotting and identifying defects on silicon wafer. It also finds important industrial applications in metallography and metrology.

The Fourier ptychography (FP) imaging scheme can be implemented in an epi-illuminated mode for reflective imaging. We term it epi-illuminated FP (eFP). The schematic of the eFP setup is shown in Fig. 2-2(a), where we used two LED rings for sample illumination and a 10X (0.28 NA) objective lens for image acquisition. A beam splitter was used to separate the illumination path and the detection path, similar to the conventional epi-illumination platform. The first LED ring was mounted at the epi-illumination arm of the microscope platform. The emitted light from different elements of this LED ring was focused at different off-axis positions of the objective's back-focal plane. The light wave exiting from the objective, thus, illuminated the sample from different oblique incident angles. The second LED ring was mounted outside the employed objective lens. This LED ring, thus, illuminated the sample with an illumination NA higher than the collection NA of the employed optics. This second LED ring gives us true super-resolution imaging performance (better than the incoherent diffraction limit of the employed lens).

To operate the eFP system, we simply turn on the LED elements one after one. For each LED element, we acquire one raw intensity of the sample. We used 8 elements for the first LED ring and 16 elements for the second ring. Based on all acquired images (24 in this setup), we then recover the high-resolution sample image. Figure 2-2(b) shows the raw image captured by eFP platform and Fig. 2-2(c) shows the recovered image. The 390 nm linewidth of group 10, element 3 is clearly resolved. The final synthetic NA is about three times higher than the NA of the employed objective lens in a coherent imaging setting (i.e., 1.5 times better resolution than the incoherent diffraction limit).

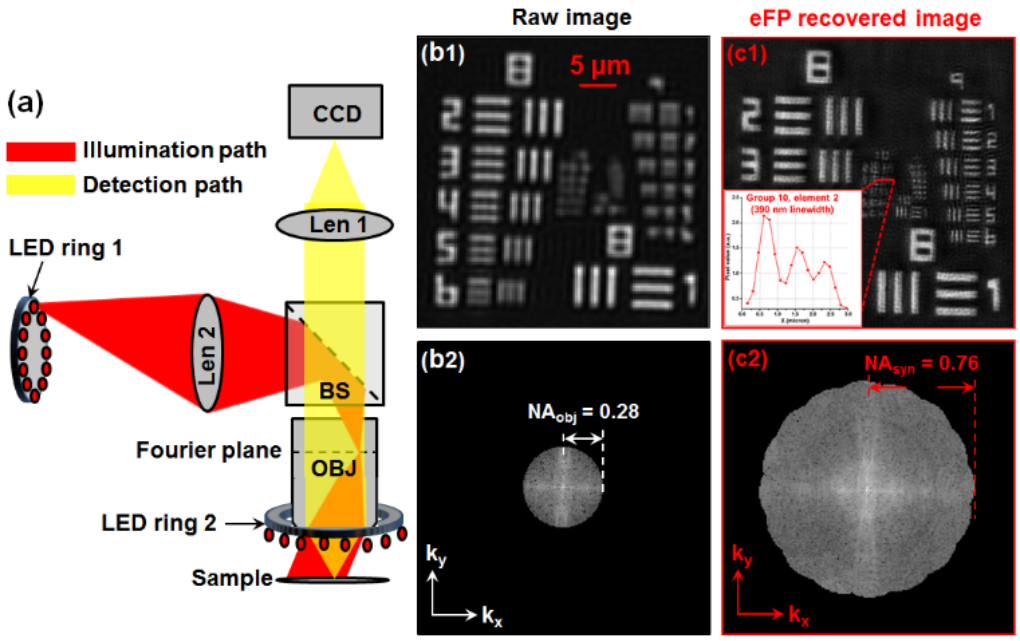

Figure 2-2: Epi-illuminated FP (eFP). (a) Schematic of the optical setup. Two LED rings were used for sample illumination. The first LED ring was mounted at the epi-illumination arm of the platform. The emitted light from this LED ring was focused at off-axis positions of the objective's back-focal plane. The second LED ring was mounted outside the objective lens. The captured images are synthesized in the Fourier domain to produce a final image with three times higher NA for coherent imaging (1.5 times better resolution than the incoherent diffraction limit).

We have tested the eFP platform with two samples, a silicon wafer with scratches and a compact disc. Figure 2-3(a1) and 2-3(a2) show the raw images of the silicon wafer. Figure 2-3(a3) shows the raw image of a compact disc. Figure 2-3(b) shows the eFP recovered images. In Fig. 2-3(c), we also show the high-resolution ground truth using a conventional microscope with a 40X, 0.75 NA objective lens. Small features are highlighted in Fig. 2-3 for comparison. We note that, the high-resolution ground truth of the compact disc cannot be taken due to a plastic layer on top of the surface (the working distance of conventional high-NA objective is not long enough).

The reported eFP can be readily employed in most existing epi-illuminated imaging platforms without major hardware modifications. It provides useful insights for the development of reflective imaging platforms using low-NA optics. In particular, we can combine the advantages of low-NA optics (large field-of-view, long working distance and etc.) with the high-resolution imaging capability for wafer inspection.

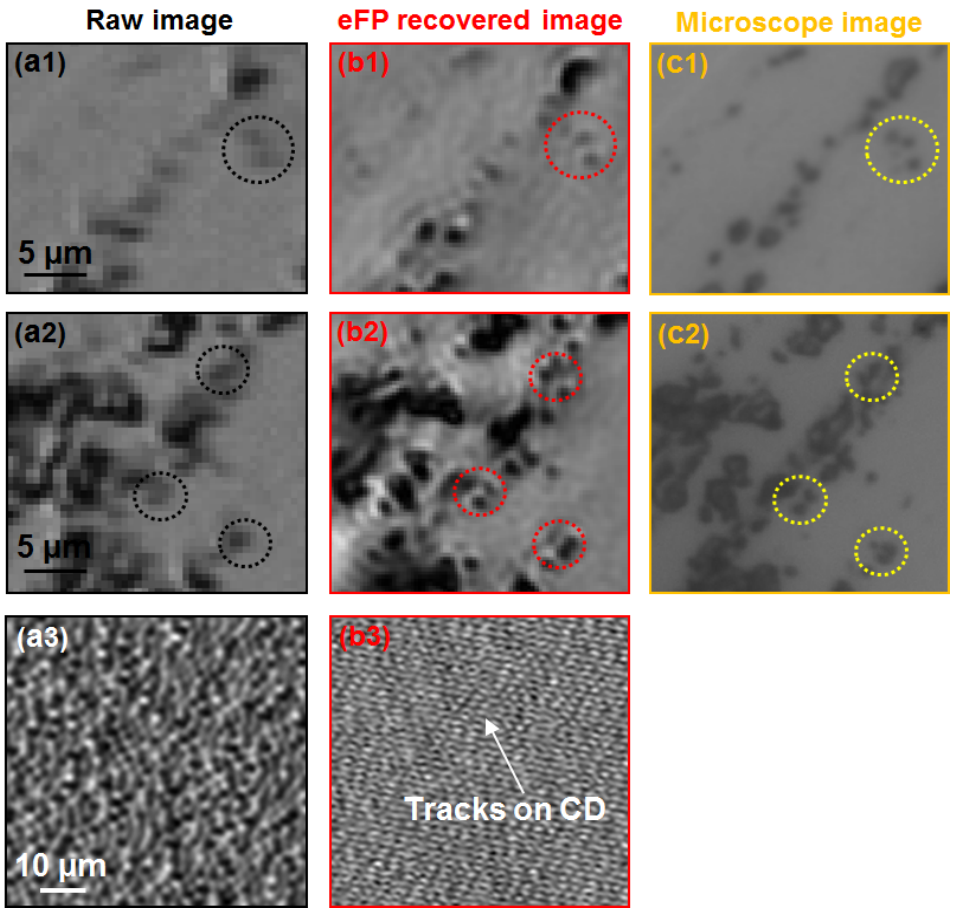

Figure 2-3: Imaging performance of the eFP platform. (a) Raw images of a silicon wafer and a compact disc. (b) eFP recovered images. (c) Conventional microscopy images using a 40X, 0.75 NA objective lens.

2.3 Dark-field Fourier ptychography

In original FP imaging, we need to illuminate the sample from small incident angles to large incident angles. The corresponding images are then synthesized in the Fourier space. As such, the recovered brightfield image contains all frequency components within the synthetic passband. However, for many applications, we only care about the high frequency component at the Fourier space. These components represent the detailed information of the sample. Therefore, a logical development of FP is to selectively capture images at the Fourier space to reduce the acquisition time.

Figure 2-4 demonstrates our recent development of darkfield FP (dFP) imaging, where we only use darkfield raw images in the FP reconstruction process. Figure 2-4(a1) shows the raw brightfield image captured with a 0.1 NA objective lens and Fig. 2-4(a2) shows the corresponding Fourier spectrum. In Fig. 2-4(b), we used raw images with an illumination NA higher than 0.2 to perform dFP recovery, and the final synthetic NA is 0.5. In Fig. 2-4(c), we used raw images with an illumination NA higher than 0.3 for dFP recovery. The empty regions in Fig. 2-4(b2) and 2-4(c2) correspond to low-frequency components of the sample. As a comparison, we also show the brightfield FP recovery in Fig. 2-4(d). In Fig. 2-4(a1)-(d1), we highlighted small features of the sample for comparison. From this comparison, we can identify the small details of the sample from both the dFP and brightfield FP recoveries.

dFP is a straight forward extension of the brightfield FP. However, we note that, dFP has the potential to perform high-resolution, high-throughput microscopy imaging with ultra large field of view. For example, we can use a low-NA lens for image acquisition and use plane waves with large incident angles

for sample illumination. The recovered dFP image only contains detailed information of the sample; the low-frequency components will not be presented. The dFP imaging modality may find applications in surface inspection, where we aim to identify small features of the sample over a large field of view and in high-throughput.

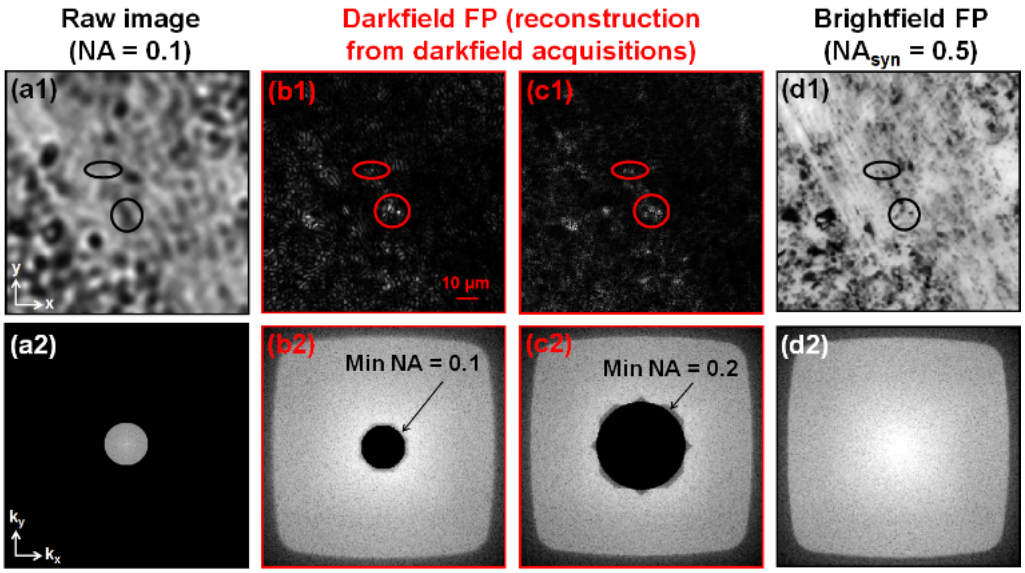

Figure 2-4: Darkfield FP (dFP). The sample is a glass slide deposited with carbon particles. (a1) The raw brightfield image captured with a 0.1 NA objective lens. (a2) The corresponding Fourier spectrum of (a1). Darkfield FP recovery using raw images with an illumination NA higher than 0.2 (b1) and 0.3 (c1). (b2) and (c2): Fourier spectrums of (b1) and (c1). (d1) The brightfield FP recovery using both brightfield and darkfield raw images. (d2) The corresponding Fourier spectrum of (d1), with a synthetic NA of 0.5. Detailed features are highlighted in (a1)-(d1) for comparison.

Bibliography

[1] G. Zheng, R. Horstmeyer, and C. Yang, "Wide-field, high-resolution Fourier ptychographic microscopy," Nature Photonics, vol. 7, pp. 739-745, 2013.
[2] V. Mico, Z. Zalevsky, P. García-Martínez, and J. García, "Synthetic aperture superresolution with multiple off-axis holograms," JOSA A, vol. 23, pp. 3162-3170, 2006.

[3] J. Di, J. Zhao, H. Jiang, P. Zhang, Q. Fan, and W. Sun, "High resolution digital holographic microscopy with a wide field of view based on a synthetic aperture technique and use of linear CCD scanning," Appl. Opt., vol. 47, pp. 5654-5659, 2008.
[4] T. R. Hillman, T. Gutzler, S. A. Alexandrov, and D. D. Sampson, "High-resolution, wide-field object reconstruction with synthetic aperture Fourier holographic optical microscopy," Optics Express, vol. 17, pp. 7873-7892, 2009.
[5] L. Granero, V. Micó, Z. Zalevsky, and J. García, "Synthetic aperture superresolved microscopy in digital lensless Fourier holography by time and angular multiplexing of the object information," Appl. Opt., vol. 49, pp. 845-857, 2010.
[6] T. Gutzler, T. R. Hillman, S. A. Alexandrov, and D. D. Sampson, "Coherent aperture-synthesis, wide-field, high-resolution holographic microscopy of biological tissue," Opt. Lett., vol. 35, pp. 1136-1138, 04/15 2010.
[7] A. Meinel, "Aperture synthesis using independent telescopes," Applied Optics, vol. 9, pp. 2501-2501, 1970.
[8] T. Turpin, L. Gesell, J. Lapides, and C. Price, "Theory of the synthetic aperture microscope," Proc. SPIE, vol. 2566, pp. 230-240, 1995.
[9] J. R. Fienup, "Phase retrieval algorithms: a comparison," Applied optics, vol. 21, pp. 2758-2769, 1982.
[10] V. Elser, "Phase retrieval by iterated projections," JOSA A, vol. 20, pp. 40-55, 2003.
[11] H. M. L. Faulkner and J. M. Rodenburg, "Movable Aperture Lensless Transmission Microscopy: A Novel Phase Retrieval Algorithm," Physical Review Letters, vol. 93, p. 023903, 07/09/ 2004.
[12] A. M. Maiden and J. M. Rodenburg, "An improved ptychographical phase retrieval algorithm for diffractive imaging," Ultramicroscopy, vol. 109, pp. 1256-1262, 2009.
[13] R. Gonsalves, "Phase retrieval from modulus data," JOSA, vol. 66, pp. 961-964, 1976.
[14] J. R. Fienup, "Reconstruction of a complex-valued object from the modulus of its Fourier transform using a support constraint," JOSA A, vol. 4, pp. 118-123, 1987.
[15] E. J. Candes, T. Strohmer, and V. Voroninski, "Phaselift: Exact and stable signal recovery from magnitude measurements via convex programming," Communications on Pure and Applied Mathematics, vol. 66, pp. 1241-1274, 2013.
[16] E. J. Candes, Y. C. Eldar, T. Strohmer, and V. Voroninski, "Phase retrieval via matrix completion," SIAM Review, vol. 57, pp. 225-251, 2015.
[17] I. Waldspurger, A. d'Aspremont, and S. Mallat, "Phase recovery, maxcut and complex semidefinite programming," Mathematical Programming, vol. 149, pp. 47-81, 2015.
[18] R. Horstmeyer, R. Y. Chen, X. Ou, B. Ames, J. A. Tropp, and C. Yang, "Solving ptychography with a convex relaxation," New Journal of Physics, vol. 17, p. 053044, 2015.
[19] E. J. Candes, X. Li, and M. Soltanolkotabi, "Phase retrieval via Wirtinger flow: Theory and algorithms," Information Theory, IEEE Transactions on, vol. 61, pp. 1985-2007, 2015.
[20] L. Bian, J. Suo, G. Zheng, K. Guo, F. Chen, and Q. Dai, "Fourier ptychographic reconstruction using Wirtinger flow optimization," Optics Express, vol. 23, pp. 4856-4866, 2015/02/23 2015.
[21] P. Li, D. J. Batey, T. B. Edo, and J. M. Rodenburg, "Separation of three-dimensional scattering effects in tilt-series Fourier ptychography," Ultramicroscopy, vol. 158, pp. 1-7, 2015.
[22] W. Hoppe and G. Strube, "Diffraction in inhomogeneous primary wave fields. 2. Optical experiments for phase determination of lattice interferences," Acta Crystallogr. A, vol. 25, pp. 502-507, 1969.

[23] J. Rodenburg, A. Hurst, A. Cullis, B. Dobson, F. Pfeiffer, O. Bunk, et al., "Hard-x-ray lensless imaging of extended objects," Physical review letters, vol. 98, p. 034801, 2007.
[24] J. Rodenburg, "Ptychography and related diffractive imaging methods," Advances in Imaging and Electron Physics, vol. 150, p. 87, 2008.
[25] R. Horstmeyer and C. Yang, "A phase space model of Fourier ptychographic microscopy," Optics Express, vol. 22, pp. 338-358, 2014/01/13 2014.
[26] G. Zheng, "Breakthroughs in Photonics 2013: Fourier Ptychographic Imaging," Photonics Journal, IEEE, vol. 6, pp. 1-7, 2014.
[27] T. B. Edo, D. J. Batey, A. M. Maiden, C. Rau, U. Wagner, Z. D. Pešić, et al., "Sampling in x-ray ptychography," Physical Review A, vol. 87, p. 053850, 05/30/ 2013.
[28] D. J. Batey, D. Claus, and J. M. Rodenburg, "Information multiplexing in ptychography," Ultramicroscopy, vol. 138, pp. 13-21, 2014.
[29] P. Thibault and A. Menzel, "Reconstructing state mixtures from diffraction measurements," Nature, vol. 494, pp. 68-71, 2013.
[30] A. M. Maiden, M. J. Humphry, and J. M. Rodenburg, "Ptychographic transmission microscopy in three dimensions using a multi-slice approach," Journal of the Optical Society of America A, vol. 29, pp. 1606-1614, 2012/08/01 2012.
[31] T. Godden, R. Suman, M. Humphry, J. Rodenburg, and A. Maiden, "Ptychographic microscope for three-dimensional imaging," Opt. Express, vol. 22, p. 12513, 2014.
[32] P. Thibault, M. Dierolf, O. Bunk, A. Menzel, and F. Pfeiffer, "Probe retrieval in ptychographic coherent diffractive imaging," Ultramicroscopy, vol. 109, pp. 338-343, 2009.
[33] S. Dong, R. Shiradkar, P. Nanda, and G. Zheng, "Spectral multiplexing and coherent-state decomposition in Fourier ptychographic imaging," Biomedical Optics Express, vol. 5, pp. 1757-1767, 2014/06/01 2014.
[34] X. Ou, G. Zheng, and C. Yang, "Embedded pupil function recovery for Fourier ptychographic microscopy," Optics Express, vol. 22, pp. 4960-4972, 2014/03/10 2014.
[35] L. Tian, X. Li, K. Ramchandran, and L. Waller, "Multiplexed coded illumination for Fourier Ptychography with an LED array microscope," Biomedical optics express, vol. 5, pp. 2376-2389, 2014.
[36] L. Tian and L. Waller, "3D intensity and phase imaging from light field measurements in an LED array microscope," Optica, vol. 2, pp. 104-111, 2015.
[37] S. Dong, Z. Bian, R. Shiradkar, and G. Zheng, "Sparsely sampled Fourier ptychography," Optics Express, vol. 22, pp. 5455-5464, 2014/03/10 2014.
[38] S. Dong, R. Horstmeyer, R. Shiradkar, K. Guo, X. Ou, Z. Bian, et al., "Aperture-scanning Fourier ptychography for 3D refocusing and super-resolution macroscopic imaging," Optics Express, vol. 22, pp. 13586-13599, 2014/06/02 2014.
[39] Z. Bian, S. Dong, and G. Zheng, "Adaptive system correction for robust Fourier ptychographic imaging," Optics Express, vol. 21, pp. 32400-32410, 2013/12/30 2013.
[40] S. Dong, K. Guo, P. Nanda, R. Shiradkar, and G. Zheng, "FPscope: a field-portable high-resolution microscope using a cellphone lens," Biomedical Optics Express, vol. 5, pp. 3305-3310, 2014/10/01 2014.
[41] K. Guo, S. Dong, P. Nanda, and G. Zheng, "Optimization of sampling pattern and the design of Fourier ptychographic illuminator," Optics Express, vol. 23, pp. 6171-6180, 2015/03/09 2015.
[42] L. Bian, J. Suo, G. Situ, G. Zheng, F. Chen, and Q. Dai, "Content adaptive illumination for Fourier ptychography," Optics Letters, vol. 39, pp. 6648-6651, 2014/12/01 2014.

Chapter 3 Sampling optimization of Fourier ptychography

In the original FP approach, a periodic LED array is used for sample illumination, and therefore, the scanning pattern is a uniform grid in the Fourier space. Such a uniform sampling scheme leads to 3 major problems for FP, namely: 1) it requires a large number of raw images, 2) it introduces the raster grid artefacts in the reconstruction process, and 3) it requires a high-dynamic-range detector. In this chapter, we investigate scanning sequences and sampling patterns to optimize the FP approach. For most biological samples, signal energy is concentrated at low-frequency region, and as such, we can perform non-uniform Fourier sampling in FP by considering the signal structure. In contrast, conventional ptychography perform uniform sampling over the entire real space. To implement the non-uniform Fourier sampling scheme in FP, we have designed and built an illuminator using LEDs mounted on a 3D-printed plastic case. The advantages of this illuminator are threefold in that: 1) it reduces the number of image acquisitions by at least 50% (68 raw images versus 137 in the original FP setup), 2) it departs from the translational symmetry of sampling to solve the raster grid artifact problem, and 3) it reduces the dynamic range of the captured images 6-fold. The results reported in this chapter significantly shortened acquisition time and improved quality of FP reconstructions. It may provide new insights for developing Fourier ptychographic imaging platforms and find important applications in digital pathology.

3.1 Background

Fourier ptychography (FP) illuminates the sample using oblique incident angles and captures the corresponding low-resolution images. Sharing its roots with ptychography [1–8] and other phase retrieval methods [9–11], the Fourier ptychographic recovery process iteratively synthesizes the

captured images in the Fourier domain to recover a high-pixel-count complex sample image [1, 12–17]. In particular, FP switches between the spatial and the Fourier domain. In the spatial domain, the captured images are used as the intensity constraint for the solution. In the Fourier domain, the confined pupil function of the objective lens is used as the support constraint for the solution. This pupil function constraint is digitally panned across Fourier space according to the illumination angle. By introducing a phase factor to model the pupil function, the FP approach is able to bypass the design constraints of a conventional microscope platform and digitally correct for aberrations associated with the employed optics [18–20]. Recently, we have also extended the FP recovery scheme for super-resolution fluorescence microscopy [21] and incoherent photography [22].

To better understand the motivation of this chapter, it is helpful to compare and contrast ptychography and FP. Both ptychography and FP capture multiple intensity images of the sample and seek a complex solution that is consistent with these measurements. In ptychography, the sample is scanned in the spatial domain and diffraction patterns are captured at the Fourier domain (i.e., the far field) without using any lens. For FP, the spatial domain and the Fourier domain are swapped using a lens. Thus, the scanning process of FP is at the Fourier domain and the images are captured at the spatial domain. A critical consideration for both approaches is the scanning pattern, which includes the scanning sequence, overlap ratio between adjacent samples, and the overlap uniformity. For ptychography, different scanning patterns in the spatial domain have been demonstrated to achieve uniform overlap and good convergence, including the raster scanned mesh pattern with random offset [23], the concentrated-circles [24], and the Fermat spiral trajectory [25]. Unlike ptychography, the scanning pattern of FP is in the Fourier domain and the signal distribution may need to be taken into consideration [26]. For most biological samples, signal energy is concentrated at low-frequencies which makes it better to start the scanning sequence from the low-

frequency regions where most of the energy is located. By doing so, the solution converges to the global minimum with fewer iterations. Furthermore, sampling overlap is applied non-uniformly at different regions to best capture signal distribution in the Fourier space [26]. In the original FP approach, a periodic LED array is placed at the far field for sample illumination, and therefore, the scan pattern is a periodic grid in the Fourier domain. Such a uniform sampling scheme leads to 3 major problems for FP, namely: 1) it requires a large number of raw images to be acquired, 2) it introduces raster grid artifacts [8] in the reconstruction process, and 3) it needs a high-dynamic-range detector.

In this chapter, we investigate the scanning sequences and sampling patterns to optimize the FP approach. We will show that signal energy criteria can be used to determine the scanning sequence in the reconstruction process. Based on the energy distribution in Fourier domain, a non-uniform sampling scheme can be used to reduce the number of acquisitions. To this end, we have designed and built an illuminator using LEDs mounted on 3D-printed plastic rings. The advantages of this illuminator are threefold: 1) it reduces the number of image acquisitions by at least 50% (68 raw images versus 137 in the original FP setup), 2) it departs from the translational symmetry of sampling to solve the raster grid artifact problem, and 3) it reduces the dynamic range of the captured images 6-fold. The results reported in this chapter significantly shortened the acquisition time and improved quality of FP reconstructions. It may provide new insights for the development of FP platforms and find important applications in digital pathology.

This chapter is structured as follows: in section 3.2, we will investigate the scanning sequence of the FP approach for fast solution convergence. In section 3.3, we will investigate the sampling pattern in the Fourier domain to reduce the number of acquisitions. In section 3.4, we will discuss the design of the Fourier ptychographic illuminator and demonstrate its advantages. Finally, we will summarize the results in section 3.5.

3.2 Choice of scanning sequence for Fourier ptychography

The choice of scanning sequence is important for fast solution convergence during the FP reconstruction process. Such a sequence defines the starting point of the optimization algorithm. If the starting point is not properly chosen, the iterative alternative projection algorithm [27] may stagnate at a local minimum instead of reaching the global minimum. In this section, we will answer the following question: If we have N raw images corresponding to different incident angles, what is the optimal sequence of these raw images for the FP reconstruction algorithm? For example, consider raw images I1, I2, and I3 with each image corresponding to a different incident angle. In the FP reconstruction algorithm, we can update the sample estimate first with I1, then with I2, and lastly with I3. We can also choose another updating sequence such as I2, I1, and I3. We note that in the experimental implementation of FP, the order of acquiring raw images is irrelevant to the algorithm (one can reorder the sequence after the data have been acquired). When processing the data post-acquisition, we need to be mindful of the sequence of raw images we use to update the sample estimate. However, implementing fast FP would require each captured raw image to be processed in real time, and in such a case the acquisition scanning sequence needs to be the same in the hardware, i.e., we need to light up the LED elements in the same optimal order.

Here, we will discuss three recovery sequences and compare the quality of the reconstructed images and convergence speeds. The three recovery sequences are 1) a random sequence, 2) the sequence ranked by the LED illumination numerical aperture (NA), and 3) the sequence ranked by the total energy of the raw image. For case 1, we will generate a random sequence of the captured images and use them to update the sample estimate. For case 2, we will update the sample estimate using the images from the smallest incident angle to largest incident angle. For case 3, we will reorder the captured images according to their total intensity values and use this to update the sample estimate. For each case, we will use the Fourier ptychographic algorithm for recovering the high-resolution images. The algorithm starts with a high-

resolution spectrum estimate of the sample. Next, this sample spectrum estimate is sequentially updated with the intensity measurements. For each updating step, we select a small sub-region of the spectrum estimate, corresponding to one position of the circular aperture, and apply Fourier transformation to generate a new low-resolution target image. We then replace the target image's amplitude component with our measurement to form an updated, low-resolution target image. This image is then used to update its corresponding sub-region of the sample spectrum. The replace-and-update sequence is repeated for all intensity measurements, and we iterate through the above process several times until solution convergence [1, 15].

Figure 3-1 shows the reconstructed images obtained from the three cases discussed above. We quantified the root-mean-square error (the difference between the FP reconstruction and the ground truth) for each of the results in Fig. 3-1(e). We can see that the image quality of the random order is worse when compared to the other two sequences and the corresponding RMS error is also much higher. This simulation study shows that, a carefully chosen recovery sequence is important for fast solution convergence. In the case of a random sequence, the solution may stagnate at a local minimum instead of the global minimum, as shown in Fig. 3-1(e). We also note that in the study shown in Fig. 3-1, the illumination-NA order and total energy order give similar results and convergence speeds. The reason can be explained as follows: the energy of sample image in the Fourier domain is concentrated at low-frequencies, and thus, the energy level decreases as the illumination NA increases. Therefore, these last two cases have the same image sequence.

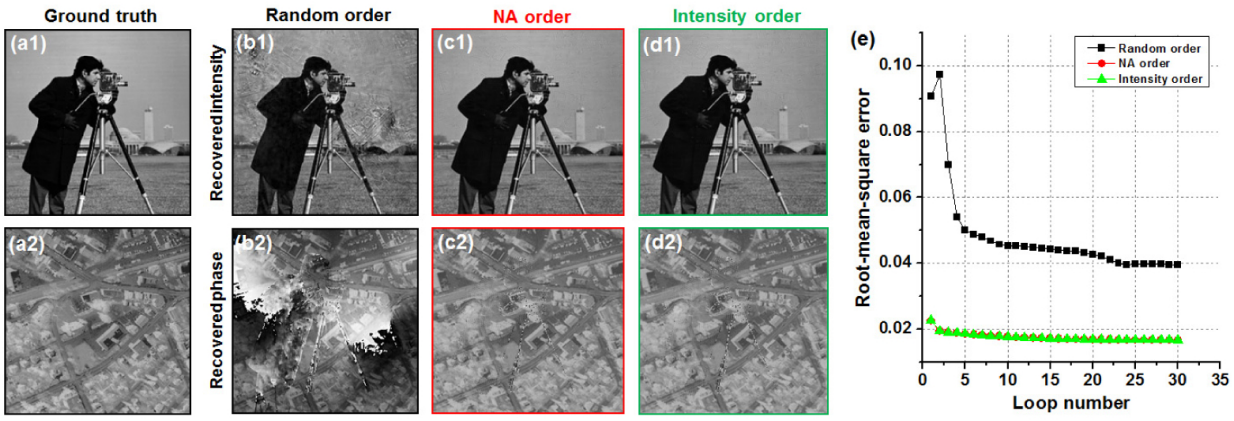

Figure 3-1: FP reconstructions with different recovery sequences. (a) Input intensity and phase images. FP reconstructions with random order (b), illumination NA order (c) and total energy order (d). (e) The RMS error of the FP reconstruction versus loop number.

To study the difference between the illumination NA order and the total energy order, we need to consider a sample image with Fourier spectrum energy not concentrated at low frequencies. In Fig. 3-2, we consider the same ground truth image (Fig. 3-1(a)) modulated by a sinusoidal pattern. In this case, the energy in the Fourier space is concentrated at two different positions, determined by the sinusoidal frequency. We repeat this simulation study with three different sequences: a random order (Fig. 3-2(a)), the illumination NA order (Fig. 3-2(b)), and the total energy order (Fig. 3-2(c)). The RMS error curves are plotted in Fig. 3-2(d) which clearly shows that the total energy order gives the best performance for solution convergence. During the iterative recovery process, raw images with high energy levels quickly guide the solution to the global minimum of the solution space. Therefore, considering the energy distribution of the sample image helps to quickly converge to the solution. This leads us to discuss non-linear sampling patterns in the next section.

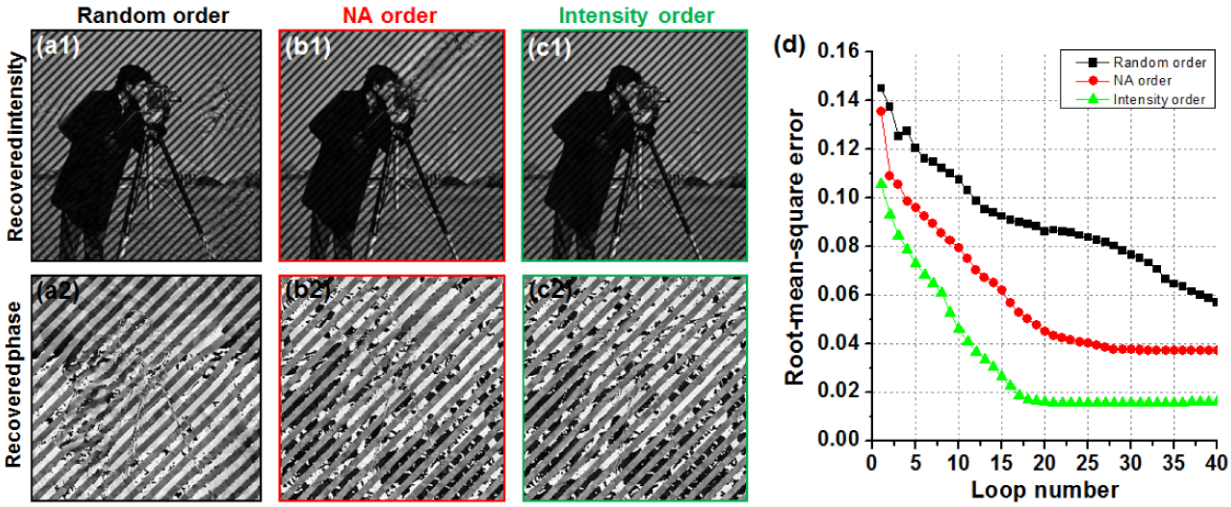

Figure 3-2 FP reconstructions with different recovery sequences. The sample image is modulated by a sinusoidal pattern, and the energy concentrates at two positions in the Fourier domain. FP reconstructions with random order (a), illumination NA order (b) and total energy order (c). (d) The RMS error of the FP reconstruction versus loop number.

3.3 Non-uniform sampling pattern for Fourier ptychography

In the previous section, we have shown that the energy criteria can be used to optimally order the reconstruction sequence. Here, we will investigate various sampling patterns in the Fourier domain. As discussed in the previous section, we will account for the energy distribution of the sample and perform non-uniform sampling in the Fourier domain.

In Fig. 3-3, we simulate various sampling patterns in the Fourier domain. We can define the Fourier overlapping percentage as the overlapping area (in the Fourier space) of two adjacent acquisitions, divided by the area of pupil function. Going from Fig. 3-3(a1) to (a5), the scanning patterns have a higher overlapping percentage at the center while the total number LED elements remains the same. In particular, Fig. 3-3(a2) shows a linear sampling pattern where the LED elements are uniformly distributed in Fourier space. The corresponding FP reconstructions are shown in Fig. 3-3(b1)-(b5). In Fig. 3(c), we plot

the overlapping percentages as a function of illumination NA for the cases shown in Fig. 3-3(a1)-(a5). We further define the sampling density ratio as the overlapping percentage at the edge divided by that at the center. Using this definition, the sampling density ratios increase from 0.7 to 2.0, going from Fig. 3-3(a1)-(a5). The RMS errors corresponding to these sampling density ratios are shown in Fig. 3-3(d). We see that a higher sampling density at the center of the Fourier space helps to recover a better FP image. This result can be explained using the same logic as the discussion in section 3.2: Since the energy of the sample concentrated at low-frequencies, a higher sampling density at the low-frequency region helps the solution converging faster to the global minimum.

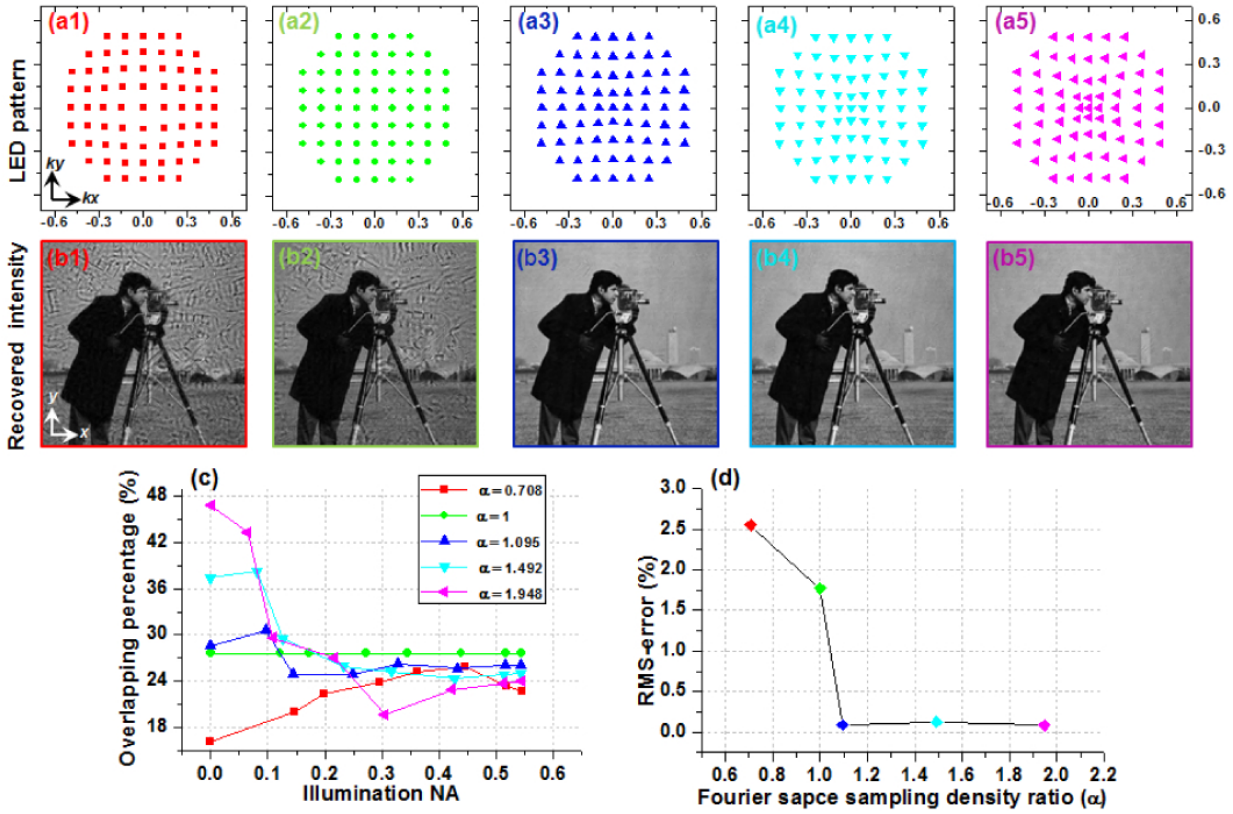

Figure 3-3 FP reconstructions with different sampling patterns in the Fourier space. (a1)-(a5) The LED sampling pattern in the Fourier space. (b1)-(b5) The FP reconstructions corresponding to (a1)-(a5). (c) The overlapping percentages as a function of illumination NA. Different curves correspond to different cases in (a1)-(a5) (see the color code). (d) The RMS error as a function of sampling density ratio.

A higher sampling density ratio helps the solution converging faster to the global minimum.

Another important consideration of the sampling pattern is the translational symmetry. In the implementation of FP, we often update the sample and the pupil function simultaneously [19, 20]. By doing so, we can recover unknown pupil aberrations and get a better high-resolution sample estimate. If the sampling pattern (the LED pattern) is a periodic pattern in the Fourier space, it leads to the raster grid pathology problem for the pupil function [8], i.e., the recovered pupil function becomes a mixture of the true aberrations and a periodic pattern. This corrupted pupil function then degrades the recovered FP image. We study this raster grid artefact problem in Fig. 3-4, where we compare two cases: a non-linear sampling pattern and a periodic pattern in the Fourier space, as shown in Fig. 3-4(a) and (b). The RMS errors are plotted as a function of the loop iteration in Fig. 3-4(c). Figure 3-4(d)-(g) show the recovered sample images and the pupil functions. We can see that with the periodic sampling pattern, the recovered image degrades with more iterations. The recovered pupil function also contains a periodic pattern, as shown in Fig. 3-4(f2) and (g2). On the other hand, with the non-linear ring pattern shown in Fig. 3-4(a), the recovered FP image continues to converge with more iterations. The recovered pupil function does not contain a periodic pattern, either.

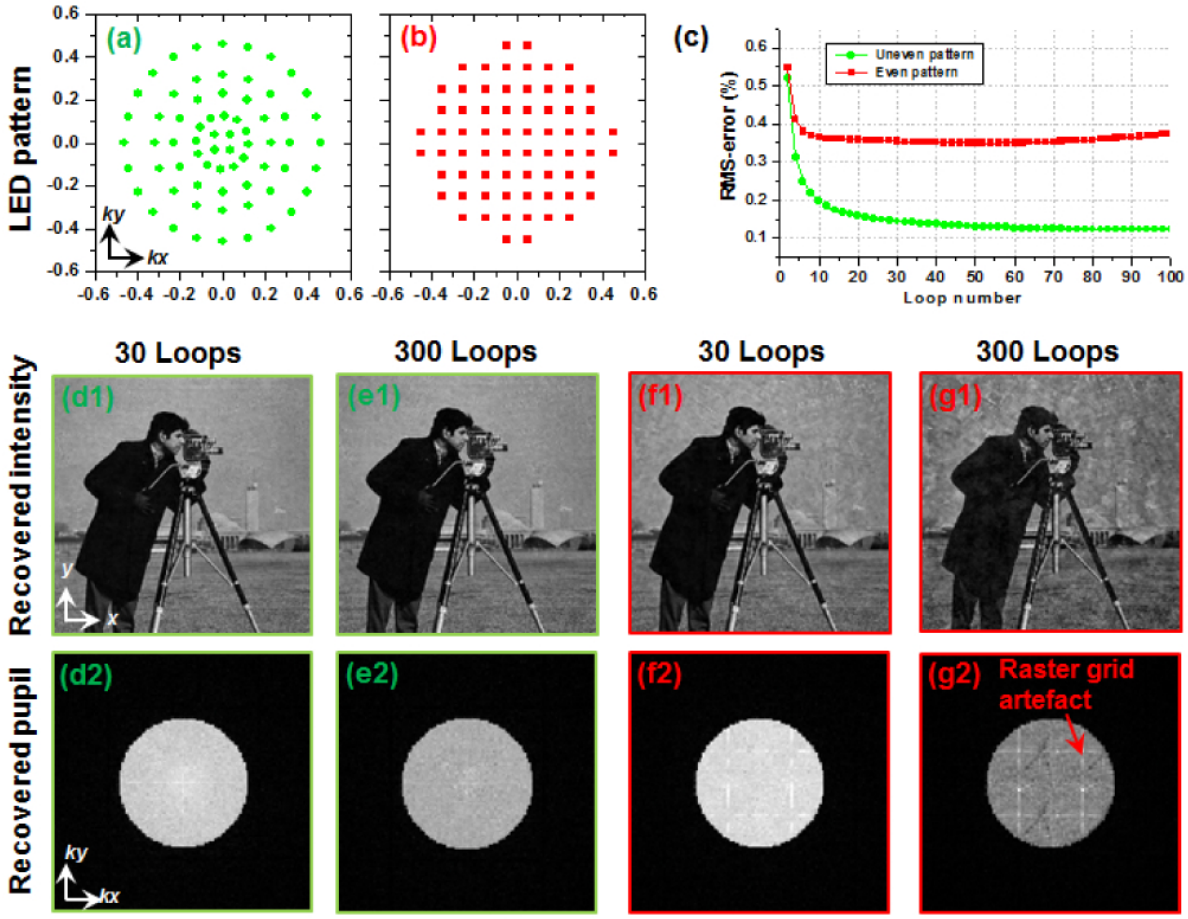

Figure 3-4 Raster grid artefact problem in FP. (a) A non-uniform sampling pattern and (b) a uniform sampling pattern. (c) The RMS errors are plotted as a function as iteration number. (d)-(e) The recovered sample images and pupil function corresponding to (a). (f)-(g) The recovered sample images and pupil function corresponding to (b). We can see the raster grid artefact problem in the recovered pupil function in (g2).

To summarize, we have demonstrated how a non-uniform sampling pattern in the Fourier space is able to 1) improve the solution convergence if the sampling density is higher at high-energy regions, 2) break the translational symmetry and solve the raster grid artefact problem. In the next section, we will discuss an experimental implementation of the non-uniform sampling pattern using ring LEDs. In particular, we aim to achieve the sampling pattern shown in Fig. 3-4(a). This sampling pattern is designed under the restriction

on the available LED ring elements. One can design other sampling patterns under a simple guideline: the spatial frequency overlapping ratio decreases from 40% at the center (bright field images) to ~15% at the edge (darkfield images).

3.4 Design of Fourier ptychographic illuminator

Based on the discussion in the previous section, we need to consider two design aspects of the Fourier ptychographic illuminator: 1) non-uniform sampling with higher density at the center, and 2) breaking the translational symmetry. Figure 3-5 shows our design of illuminator that achieves the sampling pattern shown in Fig. 3-4(a). To achieve a higher sampling density at the low-frequency region, we placed 4 LED elements and the first LED ring far away from the sample and use a mirror to direct the light to the sample. Other LED rings are positioned at larger incident angles and closer to the sample. We used a 3D printer (Makerbot) to create a plastic mount for LED rings, as shown in Fig. 3-5. A microcontroller was used to sequentially light up each LED element. Figure 3-5(a) shows the microscope setup (Olympus BX-43) with the reported illuminator. In our experiment, we used a 4X, 0.1 NA objective lens to acquire the raw image sequence and the final synthetic NA is about 0.55.

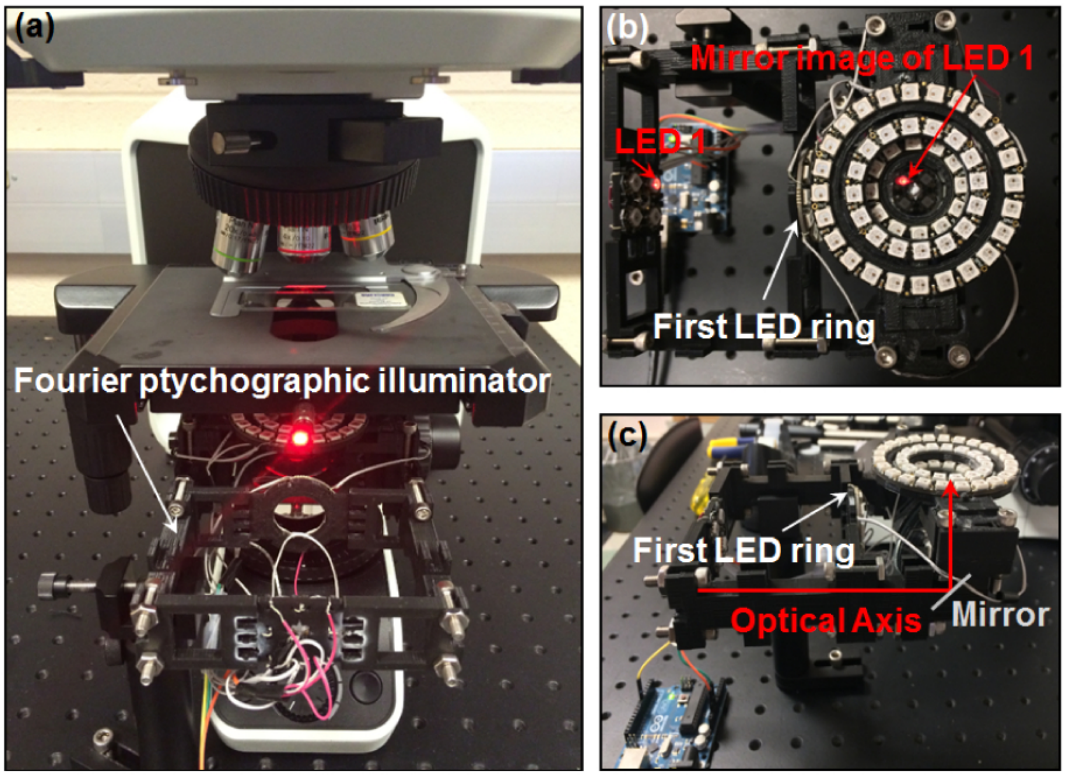

Figure 3-5: The Fourier ptychographic illuminator. (a) The illuminator is placed under the sample. (b) 4 LED elements and the first LED ring were mounted far away from the sample to achieve a higher sampling density at the low-frequency region. (c) The side view of the illuminator.

Another design consideration of the FP illuminator is the dynamic range of captured raw images. By illuminating the sample from different incident angles, FP capture both bright-field and dark-field images. Bright-field images correspond to low illumination NA and dark-field images correspond to high illumination NA. The intensity levels of the dark-field images are orders of magnitude lower than those of bright-field images. Therefore, an optimal FP illuminator needs to compensate this effect by reducing the bright-field illumination intensity while increasing the relative dark-field illumination intensity. In the reported illuminator, the 4 LED elements and the first LED ring deliver bright-field images (Fig. 3-5(c)) and they were placed far away from the sample (the illumination NA of these elements are less than the collection NA of the objective lens). As such, we reduce the relative illumination intensity for bright-field

compared with that of dark-field. Figure 3-6 shows the measured intensity of the LED elements as a function of illumination NA. This figure compares two cases, one for the uniform LED array (Fig. 3-6(a)) and the other for reported illuminator (Fig. 3-6(b)). From this comparison, we can see that the reported illuminator is able to reduce the dynamic range of FP raw image sequence 6-fold.

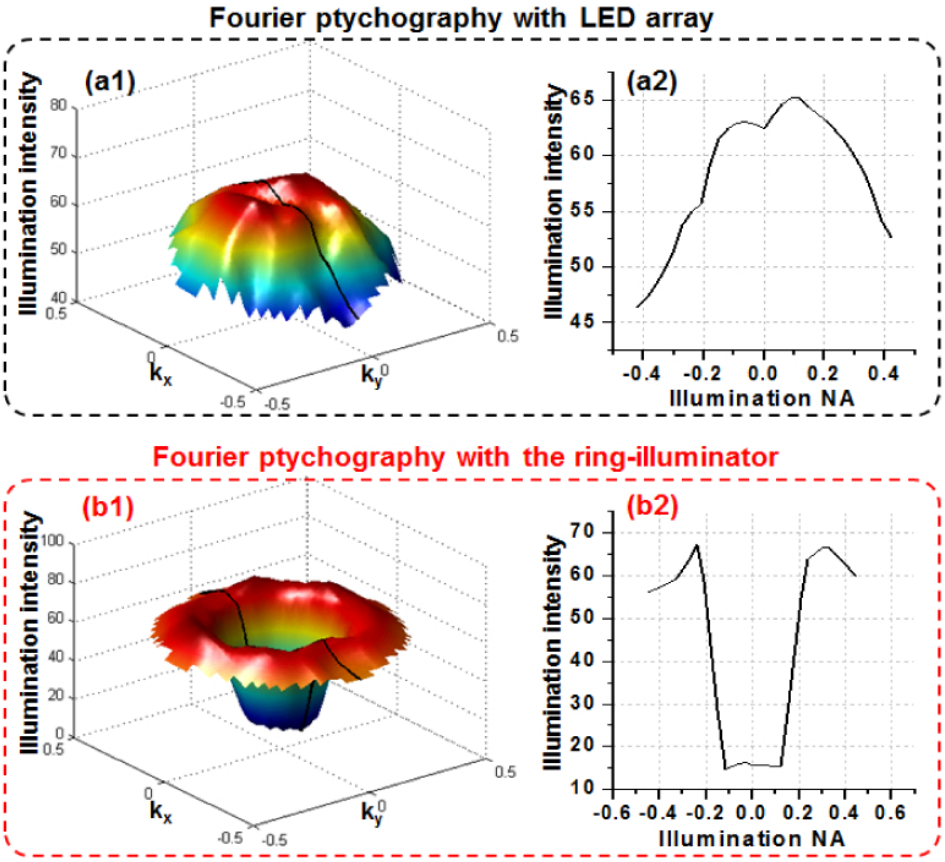

Figure 3-6: The measured intensity of the LED elements as function of illumination NA. (a) LED array illumination and (b) the reported ring-illuminator. The reported illuminator is able to reduce the dynamic range of the raw FP image sequence 6-fold.

In Fig. 3-7, we compared the FP reconstructions of the LED matrix with the reported FP illuminator. For both cases, we used 68 LED elements for sample illumination and a 4X (0.1 NA) objective for image acquisition. The final synthetic NA for both cases is ~0.55. We can see that, the image quality of the FP reconstruction using the reported illuminator is much better than that of the LED matrix. Compared to the

LED matrix illuminator, the reported FP illuminator is able shorten the acquisition time by at least 50% (68 images versus 137 images [1]). In Fig. 3-8, we recovered the color images using R/G/B illuminations and compared them to the conventional high-NA microscope objective. Again, the reported illuminator is able to deliver much better image quality.

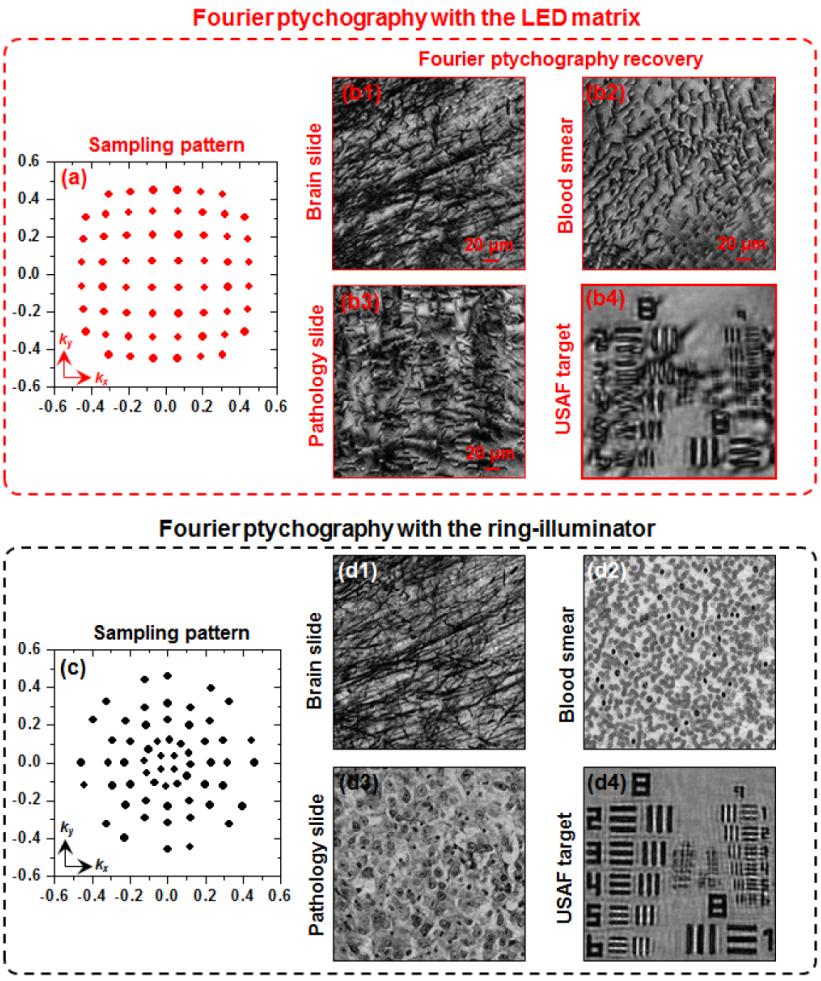

Figure 3-7: Comparison of FP reconstructions using the LED matrix (a-b) and the reported FP illuminator (c-d). The total numbers of LED elements are the same for both case (62 LEDs). (a) The sampling pattern of the periodic LED array in the Fourier space. (b) The FP reconstructions using the periodic LED array: (b1) mouse brain slice, (b2) blood smear, (b3) pathology slide, and (b4) USAF resolution target. (c) The sampling pattern of the reported FP illuminator in the Fourier space. (d) The FP reconstructions using the reported FP illuminator.

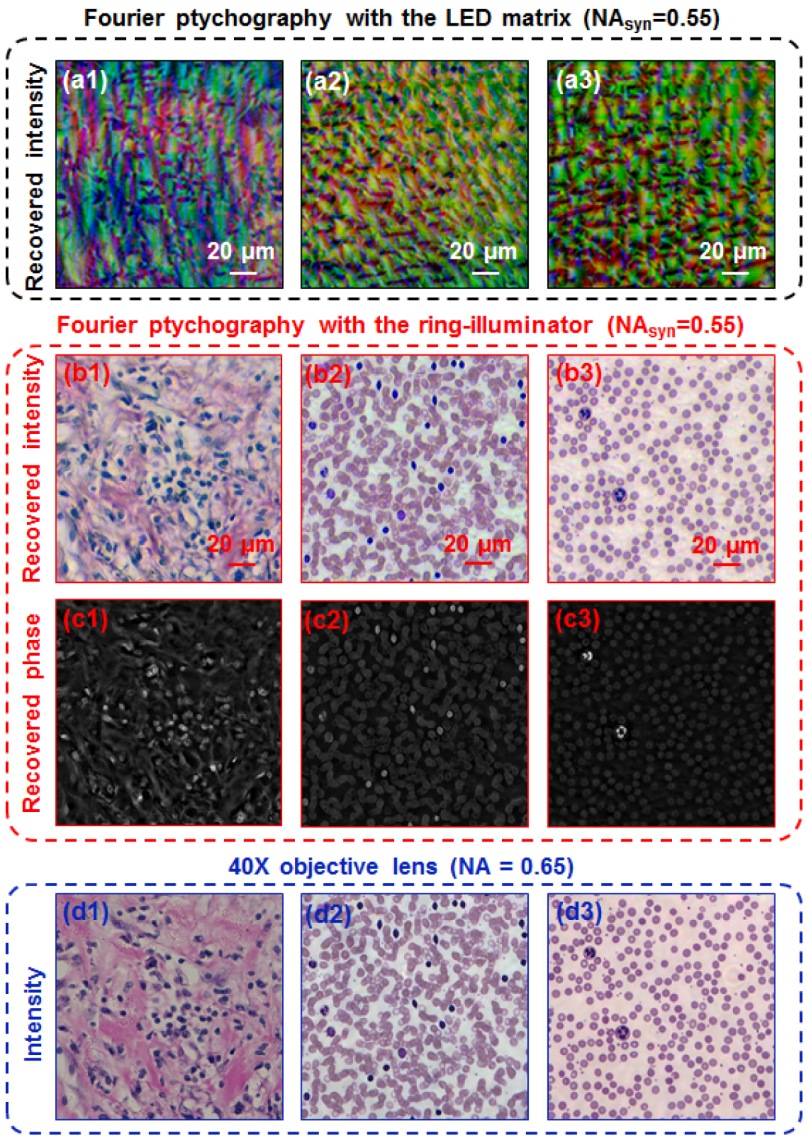

Figure 3-8: FP reconstructions using the LED array (a) and the reported FP illuminator (b-c). (d) The conventional microscope images using a 40X objective lens.

As we have discussed in section 3.3, the reported FP illuminator is able to break the translational symmetry and solve the raster grid artifact problem that plagued the original FP approach. We performed an experiment to verify this solution. In Fig. 3-9(a), we used a 15 by 15 LED matrix for sample illumination and recover both the sample image and the pupil function. In this experiment, we put the LED matrix farther away from the sample to get enough sampling overlap at the center of the Fourier space (If we only use 68

LEDs as in Fig. 3-7, we cannot get a converged solution). From Fig. 3-9(a), we can clearly see the raster grid artefact problem where the pupil function is corrupted by the periodic artifact. In Fig. 3-9(b), on the other hand, we do not see raster grid artefact problem and the recovered image has a higher quality.

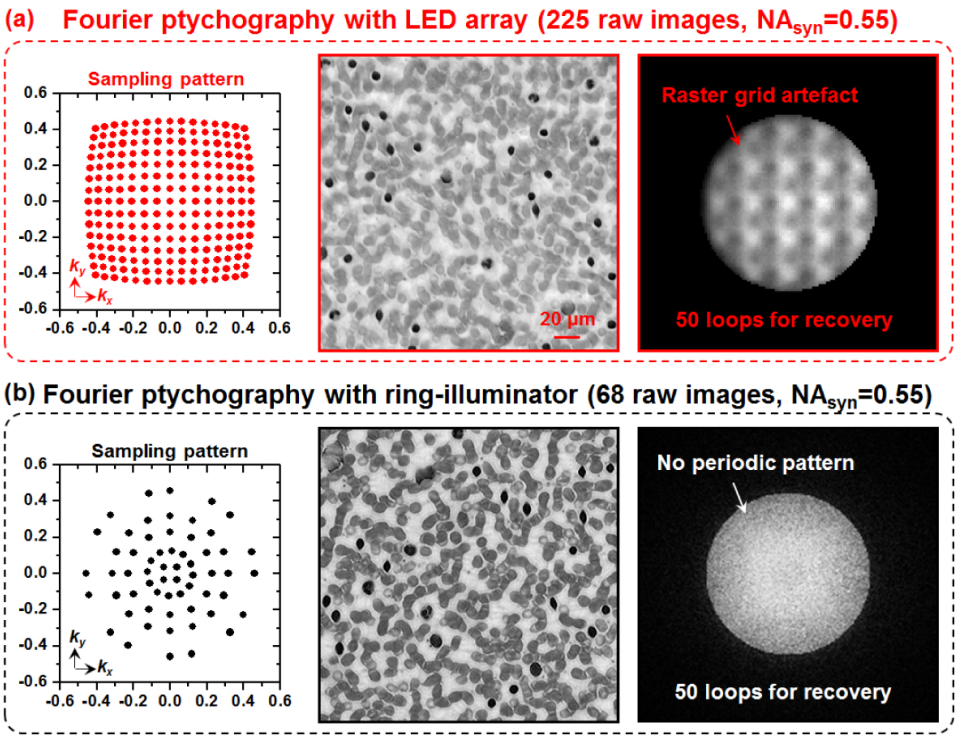

Figure 3-9: (a) FP reconstructions using the LED matrix. The image quality degrades due to the raster grid artefact problem. (b) FP reconstructions using the reported FP illuminator. The sampling pattern is not translational symmetric, and thus, it solves the raster grid artefact problem.

3.5 Discussion

We have discussed optimizing the scanning sequence and sampling pattern for the FP approach. For most biological samples, signal energy is concentrated at low-frequencies which makes it better to start the scanning sequence from the low-frequency regions where most of the energy is located. By doing so, the solution converges to the global minimum with fewer iterations. We also show that, a non-uniform sampling overlap leads to better FP reconstruction compared to the

original LED array illuminator. To implement the non-uniform Fourier sampling scheme in FP, we have designed and built an illuminator using ring LEDs and mounted on 3D-printed plastic assembly. Comparing to the original LED array illuminator, the reported FP illuminator is able to reduce the number of image acquisitions by at least 50%. It also breaks the translational symmetry of sampling and solves the raster grid artefact problem. The sampling strategy discussed in this chapter can also be implemented using a recently reported illumination engineering scheme with a low-cost liquid crystal display [28]. In this case, we do not need to worry about the size and the shape of the LED elements. One can simply place a transparent liquid crystal display at the back focal position of a condenser lens and set any open aperture on the display [28]. The results shown in this chapter may provide new insights for developing fast FP platforms and find important applications in digital pathology.

Bibliography

[1] G. Zheng, R. Horstmeyer, and C. Yang, "Wide-field, high-resolution Fourier ptychographic microscopy," Nat. Photonics 7(9), 739–745 (2013).

[2] W. Hoppe and G. Strube, "Diffraction in inhomogeneous primary wave fields. 2. Optical experiments for phase determination of lattice interferences," Acta Crystallogr. A 25, 502–507 (1969).

[3] H. M. L. Faulkner and J. M. Rodenburg, "Movable Aperture Lensless Transmission Microscopy: A Novel Phase Retrieval Algorithm," Phys. Rev. Lett. 93(2), 023903 (2004).

[4] M. Guizar-Sicairos and J. R. Fienup, "Phase retrieval with transverse translation diversity: a nonlinear optimization approach," Opt. Express 16(10), 7264–7278 (2008).

[5] J. Rodenburg, "Ptychography and related diffractive imaging methods," Adv. Imaging Electron Phys. 150, 87– 184 (2008).

[6] P. Thibault, M. Dierolf, A. Menzel, O. Bunk, C. David, and F. Pfeiffer, "High-Resolution Scanning X-Ray Diffraction Microscopy," Science 321(5887), 379–382 (2008).

[7] A. M. Maiden and J. M. Rodenburg, "An improved ptychographical phase retrieval algorithm for diffractive imaging," Ultramicroscopy 109(10), 1256–1262 (2009).

[8] P. Thibault, M. Dierolf, O. Bunk, A. Menzel, and F. Pfeiffer, "Probe retrieval in ptychographic coherent diffractive imaging," Ultramicroscopy 109(4), 338–343 (2009).

[9] R. W. Gerchberg, "A practical algorithm for the determination of phase from image and diffraction plane pictures," Optik (Stuttg.) 35, 237 (1972).

[10] J. R. Fienup, "Reconstruction of an object from the modulus of its Fourier transform," Opt. Lett. 3(1), 27–29 (1978).

[11] J. R. Fienup, "Phase retrieval algorithms: a comparison," Appl. Opt. 21(15), 2758–2769 (1982).
[12] X. Ou, R. Horstmeyer, C. Yang, and G. Zheng, "Quantitative phase imaging via Fourier ptychographic microscopy," Opt. Lett. 38(22), 4845–4848 (2013).
[13] S. Dong, R. Horstmeyer, R. Shiradkar, K. Guo, X. Ou, Z. Bian, H. Xin, and G. Zheng, "Aperture-scanning Fourier ptychography for 3D refocusing and super-resolution macroscopic imaging," Opt. Express 22(11), 13586–13599 (2014).
[14] S. Dong, R. Shiradkar, P. Nanda, and G. Zheng, "Spectral multiplexing and coherent-state decomposition in Fourier ptychographic imaging," Biomed. Opt. Express 5(6), 1757–1767 (2014).
[15] P. Memmolo, V. Bianco, F. Merola, L. Miccio, M. Paturzo, and P. Ferraro, "Breakthroughs in Photonics 2013, Holographic Imaging," IEEE Photon. J. 6(2), 0701106 (2014).
[16] A. Williams, J. Chung, X. Ou, G. Zheng, S. Rawal, Z. Ao, R. Datar, Yang, and R. Cote, "Fourier ptychographic microscopy for filtration-based circulating tumor cell enumeration and analysis," J. Biomed. Opt. 19(6), 066007 (2014).
[17] L. Tian, X. Li, K. Ramchandran, and L. Waller, "Multiplexed coded illumination for Fourier Ptychography with an LED array microscope," Biomed. Opt. Express 5(7), 2376–2389 (2014).
[18] S. Dong, K. Guo, P. Nanda, R. Shiradkar, and G. Zheng, "FPscope: a field-portable high-resolution microscope using a cellphone lens," Biomed. Opt. Express 5(10), 3305–3310 (2014).
[19] X. Ou, G. Zheng, and C. Yang, "Embedded pupil function recovery for Fourier ptychographic microscopy," Opt. Express 22(5), 4960–4972 (2014).
[20] Z. Bian, S. Dong, and G. Zheng, "Adaptive system correction for robust Fourier ptychographic imaging," Opt. Express 21(26), 32400–32410 (2013).
[21] S. Dong, P. Nanda, R. Shiradkar, K. Guo, and G. Zheng, "High-resolution fluorescence imaging via patternilluminated Fourier ptychography," Opt. Express 22(17), 20856–20870 (2014).
[22] S. Dong, P. Nanda, K. Guo, J. Liao, and G. Zheng, "Incoherent Fourier ptychographic photography using structured light," Photon. Res. 3(1), 19–23 (2015).
[23] A. M. Maiden, M. J. Humphry, M. C. Sarahan, B. Kraus, and J. M. Rodenburg, "An annealing algorithm to correct positioning errors in ptychography," Ultramicroscopy 120, 64–72 (2012).
[24] M. Dierolf, P. Thibault, A. Menzel, C. M. Kewish, K. Jefimovs, I. Schlichting, K. Von König, O. Bunk, and F. Pfeiffer, "Ptychographic coherent diffractive imaging of weakly scattering specimens," New J. Phys. 12(3), 035017 (2010).
[25] X. Huang, H. Yan, R. Harder, Y. Hwu, I. K. Robinson, and Y. S. Chu, "Optimization of overlap uniformness for ptychography," Opt. Express 22(10), 12634–12644 (2014).
[26] L. Bian, J. Suo, G. Situ, G. Zheng, F. Chen, and Q. Dai, "Content adaptive illumination for Fourier ptychography," Opt. Lett. 39(23), 6648–6651 (2014).
[27] H. H. Bauschke, P. L. Combettes, and D. R. Luke, "Phase retrieval, error reduction algorithm, and Fienup variants: a view from convex optimization," J. Opt. Soc. Am. A 19(7), 1334–1345 (2002).
[28] K. Guo, Z. Bian, S. Dong, P. Nanda, Y. M. Wang, and G. Zheng, "Microscopy illumination engineering using a low-cost liquid crystal display," Biomed. Opt. Express 6(2), 574–579 (2015).

Chapter 4 Field-portable Fourier ptychographic microscope

The large consumer market has made cellphone lens modules available at low-cost and in high-quality. In a conventional cellphone camera, the lens module is used to demagnify the scene onto the image plane of the camera, where image sensor is located. In this chapter, we report a 3D-printed high-resolution Fourier ptychographic microscope, termed FPscope, which uses a cellphone lens in a reverse manner. In our platform, we replace the image sensor with sample specimens, and use the cellphone lens to project the magnified image to the detector. To supersede the diffraction limit of the lens module, we use an LED array to illuminate the sample from different incident angles and synthesize the acquired images using the Fourier ptychographic algorithm. As a demonstration, we use the reported platform to acquire high-resolution images of biological specimens. The final achievable resolution is determined by the largest incident angle of the LED array and we demonstrate a maximum synthetic numerical aperture (NA) of 0.5. We also show that, the depth-of-focus of the reported platform is about 0.1 mm, orders of magnitude longer than that of a conventional microscope objective with a similar NA. The reported platform may enable healthcare accesses in low-resource settings.

4.1 Background

Optical microscopy pervades almost all aspects of modern bioscience and clinical applications. A typical microscope consists of an objective lens, space for relaying the image, and a tube lens to project a magnified image onto the eyepiece or a camera. To achieve high-resolution microscopic imaging, a precise and expensive objective lens is needed for collecting light over a large angle. The challenge for miniaturizing the conventional microscope platform comes from intrinsic

aberrations of the lens elements. The perfect lens obeying ray diagrams does not exist in the physical world. A microscope objective particularly highlights the lens aberrations due to the large collection angle of the entrance pupil. To improve the performance of a standard microscope, we need to pack in more lens elements to correct for both chromatic and monochromatic aberrations.

In recent years, there has been increasing interest in developing portable microscope platforms that would benefit remote clinics or be used in resource-limited environments [1-6]. Lensless microscopy is a good example of this direction. It has been shown that, sub-micron resolution can be achieved using various lensless imaging techniques, such as optofluidic microscopy [1, 3], digital in-line holography [2, 6, 7], and contact imaging microscopy [5]. Applications of these techniques range from malaria parasite screening and single cell tracking, to real-time cell culture monitoring and etc. While these techniques have been successfully demonstrated, they are limited to a small range of samples. Optofluidic microscopy requires the sample to flow across a microfluidic channel. It works well for dispersible samples such as blood, fluid cell cultures, and other suspensions of cells or organisms, but is incompatible with adherent samples or samples on glass slides. Digital in-line holographic microscopy records interference intensity distribution of a target under coherent light illumination. Reconstruction algorithms then recover the complex transmission profile of the sample. This approach works well for sparse sample such as well-isolated blood smear slides but the algorithms cannot handle confluent samples such as pathology slides. The reason for this limitation is the well-known loss of phase information during the intensity recording process. In order to recover the complex sample transmission profile, confined object constraints (sparsity constraints) need to be imposed in the spatial domain. The contact imaging approach requires the sample placed at close proximity to the sensing surface and, thus,

cannot handle conventional microscope glass slides. While techniques for mitigating these limitations have been reported [7, 8], the image quality is generally not as good as a conventional microscope.

We developed a portable high-resolution microscope platform, termed FPscope, using the Fourier ptychography (FP) approach [9, 10]. FP is a recently developed computational imaging procedure that synthesizes a number of variably illuminated, low-resolution intensity images in Fourier space to produce a high-resolution complex sample image. The FP imaging procedure transforms the general challenge of optical design that is coupled to the physical limitations of the system's aberrations to one that is solvable by computation. The final achievable resolution of FP is determined by the largest incident angle of the illumination beam, not the numerical aperture (NA) of the objective lens. The recovery information using FP is shown to be quantitative in nature. Optical aberration can also be digitally corrected by introducing a complex pupil function in the recovery process [11, 12]. Recently, we have also extended the FP procedure to multispectral imaging [13], 3D holographic imaging [14], and super-resolution macroscopic imaging beyond the diffraction limit [14].

This chapter is structured as follows: in section 4.2, we will discuss the system design of the FPscope. In section 4.3, we will characterize the imaging performance using a USAF resolution target. In section 4.4, we will demonstrate the use of the FPscope for imaging biological samples. Finally, we will summarize the results and discuss the future directions.

4.2 System design of the FPscope

The core component of the FPscope is a cellphone lens. The large consumer market has made cellphone lens modules available at low-cost and in high-quality. For a conventional cellphone camera, the lens module is used to demagnify the scene onto the image plane of the camera, where

the image sensor is located. In the FPscope, we use the cellphone lens module (Nokia 808) in the reverse manner; we replace the image sensor with sample specimen and use the cellphone lens to project the magnified image onto a low-cost CCD camera (DMM 31AU03, The Imaging Source). The magnification factor can be tuned by adjusting the distance between the sample and the cellphone lens. In our design, the magnification factor was chosen to be 4.5, to satisfy the Nyquist sampling requirement. We note that the configuration shown in Fig. 4-1(a) is not new. We have demonstrated the same configuration (using a lens in the reverse manner and projecting the magnified image onto the detector) for gigapixel imaging [15]. However, the use of a cellphone lens in conjugation with the FP algorithm enables a cost-effective solution for field-portable microscopy imaging.

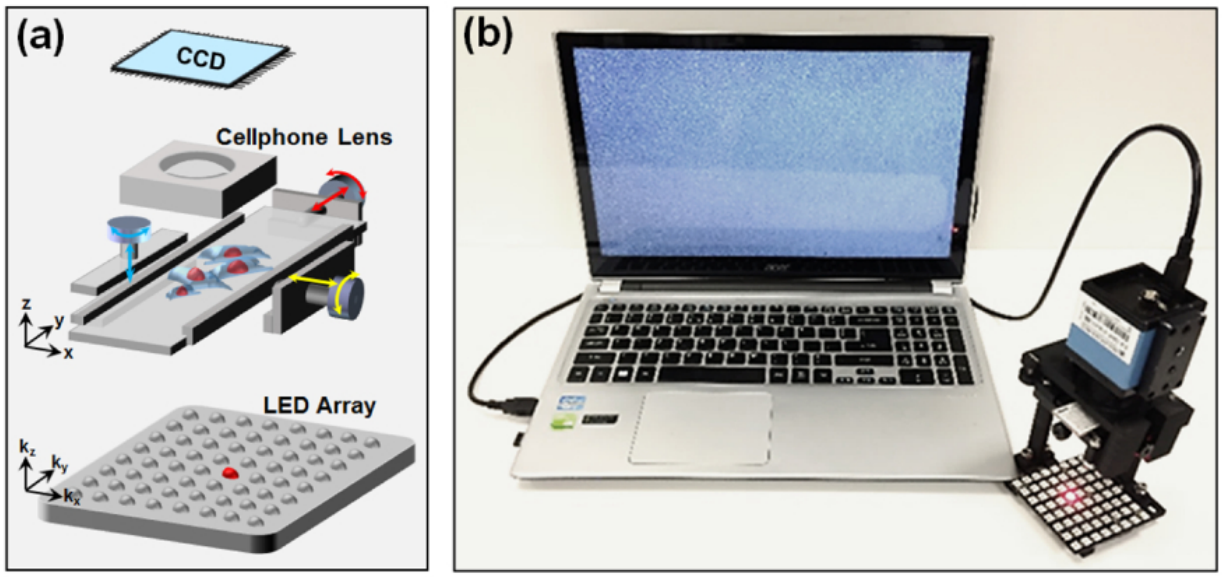

Figure 4-1: System design of FPscope. (a) A cellphone lens is used in a reverse manner. The magnified sample image is projected onto a CCD sensor. An 8 by 8 LED matrix is used for sample illumination. (b) The assembled FPscope connected to a computer.

To supersede the diffraction limit of the lens module, we used an 8 by 8 LED array for sample illumination. Each LED element of the array illuminates the sample from an oblique incident angle, and the corresponding image is acquired using the cellphone lens with a 0.15 NA. The acquired 64 images are then synthesized in Fourier space using the Fourier ptychographic algorithm. The final synthetic NA is determined by the largest incident angle of LED illumination, and it can be adjusted by changing the distance between the LED array and the sample. In our design, the distance between the LED array and the sample is chosen to be ~10 cm, corresponding to a maximum synthetic NA of 0.5. We also note that if the illumination is placed too close to the sample, there won't be enough Fourier spectrum overlap between two adjacent LEDs [16].

We designed a 3D manual stage to move the sample in the x-y plane and to adjust the focal position. Most of the components in our design were produced using a Makerbot 3D printer. The components were assembled with springs and screws. Figure 4-1(b) shows the FPscope connected to a computer.

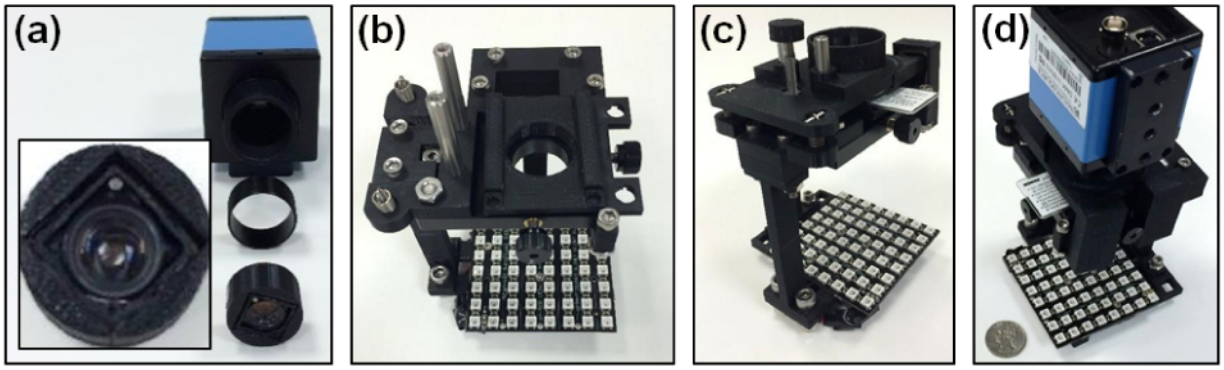

Figure 4-2: The assembling process of the FPscope. (a) A Nokia cellphone lens is fit in to a plastic case. (b) The case is assembled onto a CCD camera. (c) The assembling of the x-y stage and the slide holder. (d) The assembling of the z stage. (e) The final assembled FPscope.

Figure 4-2 shows the assembly process of the FPscope. Figure 4-2(a) and (b) show the cellphone lens mount in front of the CCD camera. Figure 4-2(c) shows the x-y stage and the slide holder assembly. Figure 4-2(d) shows the z stage assembly. The final assembled FPscope is shown in Fig. 4-2(e). The dimensions of the FPscope are 8 x 8 x 16 cm. The mass of the platform is about 250 grams, mostly of which is from the CCD camera.

4.3 System characterization of the FPscope

We characterized the system resolution performance by imaging a USAF target. In this experiment, we captured 64 low-resolution images and used them to recover a high-resolution image using the FP algorithm. The recovery process switches between the spatial and Fourier domains. In the spatial domain, the acquired low-resolution images are used to constrain the amplitude of the solution. In the Fourier domain, the coherent transfer function (i.e., the pupil function) of the cellphone lens is used as a support constraint for the solution. This support constraint is digitally panned across Fourier space to reflect the angle-varied illuminations of the 8 by 8 LED array. The detailed recovery procedure can be found in [1, 2].

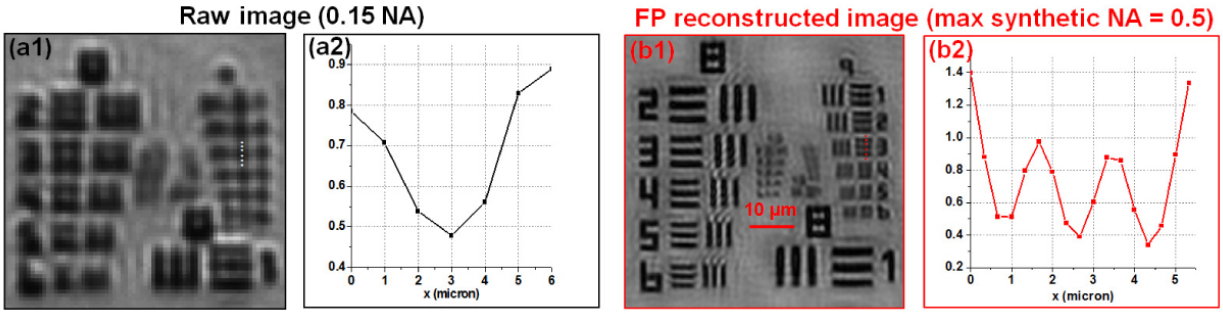

Figure 4-3: Resolution characterization of the FPscope. (a) One of the 64 low-resolution raw images captured using the cellphone lens. (b) The FP recovered image, where feature of group 9, element 3 can be clearly resolved.

Figure 4-3(a) shows the raw image captured by the cellphone lens; the NA was measured to be ~0.15. Figure 4-3(b) shows the recovered image, and the maximum synthetic NA was, as expected, about 0.5. We can clearly resolve the feature in group 9, element 3, where line-width is 0.78 µm. Another advantage of the FPscope is the ability to incorporate pupil correction in the recovery process. By introducing a second-order defocused pupil function, we can digitally tune the focal position along the optical axis. Figure 4-4 demonstrates the digital refocusing capability of the FPscope. We can see that, the depth-of-focus of the FPscope is longer than 0.1 mm without trading off resolution. This much depth-of-focus is orders of magnitude longer than that of conventional microscope objective lens with a similar NA. Therefore, the FPscope is significantly less prone to sample misalignment.

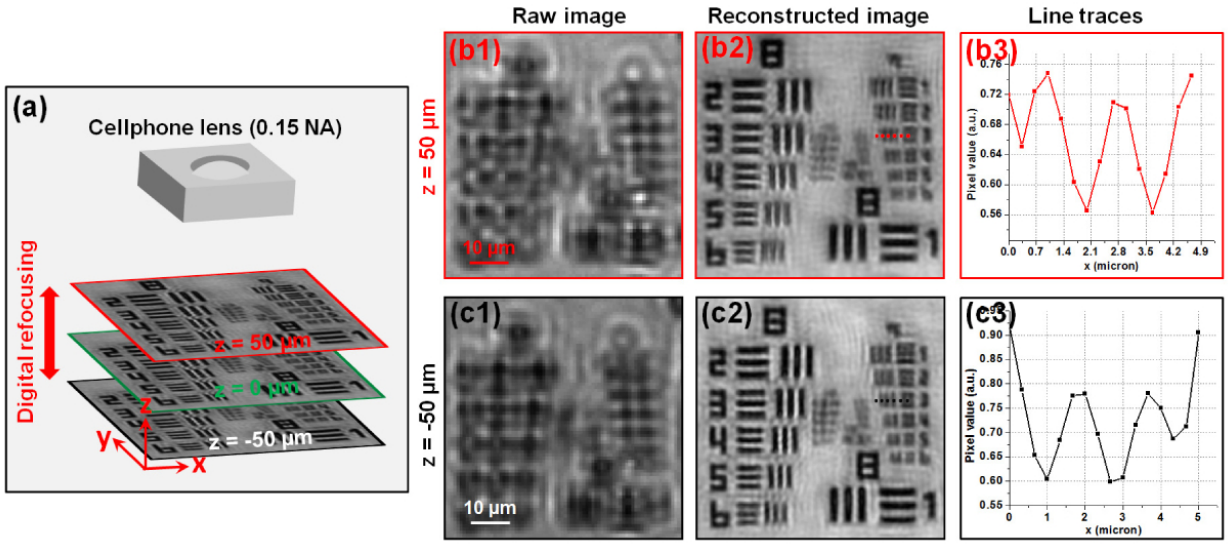

Figure 4-4: (a) Depth-of-focus characterization of the FPscope. One of the low-resolution raw images captured at (b1) z = 50 µm and (c1) z = -50 µm. (b2-b3), (c2-c3) The FP reconstructions by introducing a second-order defocused pupil function at the recovery process. The depth-of-focus is orders of magnitude longer than that of conventional microscope objective lens with similar NA.

4.4 Demonstration of the FPscope with biological samples

We also used the FPscope to image biological samples. In the first experiment, we used a blood smear as our sample. Figure 4-5(a) shows the low-resolution raw image of the blood smear. Figure 4-5(b)-(c) show the recovered intensity, phase images of the sample. We also recovered the high-resolution color image of the sample by combining the FP constructions from R/G/B illuminations. Figure 4-5(e) shows the image captured using a conventional microscope with a 40X, 0.75 NA objective lens.

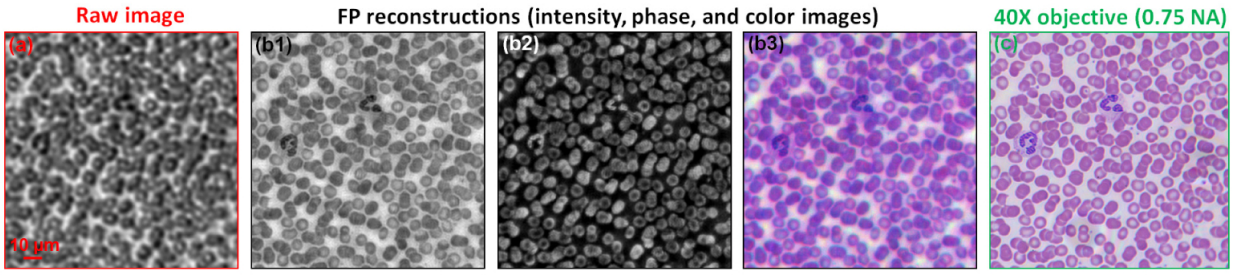

Figure 4-5: (a) Raw image of a blood smear (0.15 NA). FP recovered intensity image (b), phase (c), and color image (d). The maximum synthetic NA is 0.5. (e) The image captured using a conventional microscope with a 40X, 0.75 NA objective lens.

In the second experiment, we used a pathology slide as our sample (human adenocarcinoma of breast section, Carolina), as shown in Fig. 4-6. The full field-of-view is about 1.2 mm by 0.9 mm and corresponding computational time is about 50 seconds in MATLAB using a personal computer with an i7 CPU. High-resolution views are provided for two regions, one at the central field-of-view, and the other one at the edge. Images captured with a conventional microscope with a 0.75 NA objective lens are also provided for comparison.

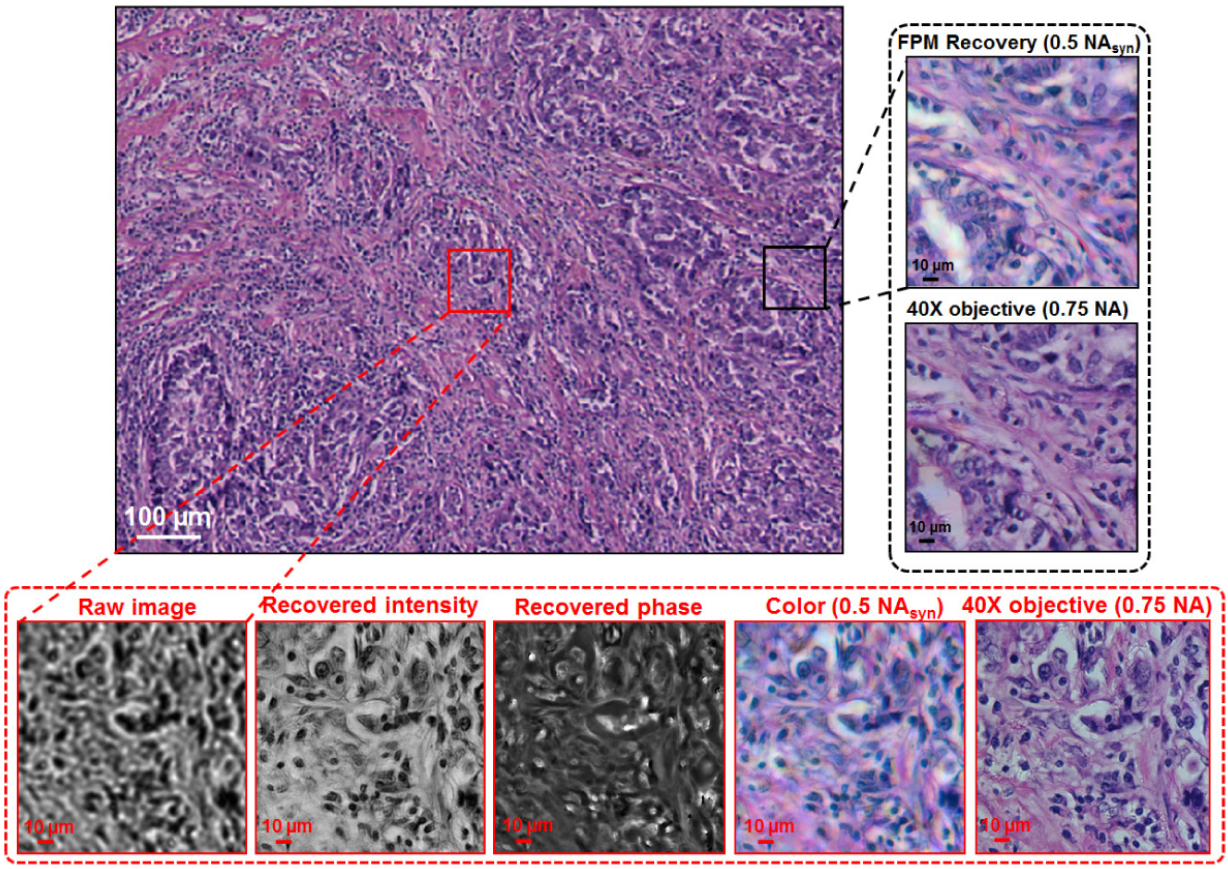

Figure 4-6: Demonstration of the FPscope using a pathology slide. The full field-of-view is about 1.2 mm by 0.9 mm. The maximum synthetic NA is 0.5. Images captured using conventional microscope with a 0.75 NA objective lens are also shown for comparison.

4.5 Discussion

We have reported a compact, lightweight, low-cost, and high-resolution microscope platform that we termed FPscope. There are several advantages of the reported platform: 1) the resolution of the reported platform is determined by the largest incident angle of the illumination, not the NA of the cellphone lens and, therefore, we are able to eliminate the traditional reliance on a high-NA lens. 2) Aberrations of the cellphone lens are compensated by the complex pupil function introduced to the FPscope. We have demonstrated the use of a second order defocused pupil

function to extend the depth-of-focus beyond the physical limit of the lens. 3) The rich literature on FP can be integrated into the reported framework. For example, the pupil correction scheme [12] and the adaptive system correction scheme [11] in FP can be integrated into the reported framework for factoring out system uncertainties, such the position of the sample, the intensity of the LED array, the position of the LED array and etc. The sparsely sampled FP scheme [16] can be used in the reported framework to bypass the pixel aliasing problem. The multispectral scheme can also be used in the FPscope to perform information multiplexing [13].

Finally, we reiterate that the use of a lens in the reverse manner is not a new idea. It has been demonstrated in our previous work on gigapixel imaging [15]. However, the use of a reversed cellphone lens in conjunction with the FP algorithm enables a cost-effective solution for field-portable microscopy imaging, which may allow healthcare access in resource-limited environments.

Bibliography

[1] X. Heng, D. Erickson, L. R. Baugh, Z. Yaqoob, P. W. Sternberg, D. Psaltis, and C. Yang, "Optofluidic microscopy—a method for implementing a high resolution optical microscope on a chip," Lab on a Chip 6, 1274-1276 (2006).

[2] W. Bishara, T.-W. Su, A. F. Coskun, and A. Ozcan, "Lensfree on-chip microscopy over a wide field-of-view using pixel super-resolution," Optics Express 18, 11181-11191 (2010).

[3] G. Zheng, S. A. Lee, S. Yang, and C. Yang, "Sub-pixel resolving optofluidic microscope for on-chip cell imaging," Lab on a Chip 10, 3125-3129 (2010).

[4] O. Mudanyali, W. Bishara, and A. Ozcan, "Lensfree super-resolution holographic microscopy using wetting films on a chip," Optics Express 19, 17378-17389 (2011).

[5] G. Zheng, S. A. Lee, Y. Antebi, M. B. Elowitz, and C. Yang, "The ePetri dish, an on-chip cell imaging platform based on subpixel perspective sweeping microscopy (SPSM)," Proceedings of the National Academy of Sciences 108, 16889-16894 (2011).

[6] W. Xu, M. Jericho, I. Meinertzhagen, and H. Kreuzer, "Digital in-line holography for biological applications," Proceedings of the National Academy of Sciences 98, 11301-11305 (2001).

[7] S. O. Isikman, A. Greenbaum, M. Lee, W. Bishara, O. Mudanyali, T.-W. Su, and A. Ozcan, "Lensfree computational microscopy tools for cell and tissue imaging at the point-of-care and in low-resource settings," Analytical Cellular Pathology 35, 229-247 (2012).

[8] A. Greenbaum, U. Sikora, and A. Ozcan, "Field-portable wide-field microscopy of dense samples using multi-height pixel super-resolution based lensfree imaging," Lab on a Chip 12, 1242-1245 (2012).
[9] G. Zheng, R. Horstmeyer, and C. Yang, "Wide-field, high-resolution Fourier ptychographic microscopy," Nature Photonics 7, 739-745 (2013).
[10] X. Ou, R. Horstmeyer, C. Yang, and G. Zheng, "Quantitative phase imaging via Fourier ptychographic microscopy," Optics Letters 38, 4845-4848 (2013).
[11] Z. Bian, S. Dong, and G. Zheng, "Adaptive system correction for robust Fourier ptychographic imaging," Optics Express 21, 32400-32410 (2013).
[12] X. Ou, G. Zheng, and C. Yang, "Embedded pupil function recovery for Fourier ptychographic microscopy," Optics Express 22, 4960-4972 (2014).
[13] S. Dong, R. Shiradkar, P. Nanda, and G. Zheng, "Spectral multiplexing and coherent-state decomposition in Fourier ptychographic imaging," Biomedical Optics Express 5, 1757-1767 (2014).
[14] S. Dong, R. Horstmeyer, R. Shiradkar, K. Guo, X. Ou, Z. Bian, H. Xin, and G. Zheng, "Aperture-scanning Fourier ptychography for 3D refocusing and super-resolution macroscopic imaging," Optics Express 22, 13586-13599 (2014).
[15] G. Zheng, X. Ou, and C. Yang, "0.5 gigapixel microscopy using a flatbed scanner," Biomedical Optics Express 5, 1-8 (2014).
[16] S. Dong, Z. Bian, R. Shiradkar, and G. Zheng, "Sparsely sampled Fourier ptychography," Optics Express 22, 5455-5464 (2014).

Chapter 5 Imaging through turbid layer via translated unknown speckle illumination

Fluorescence imaging through a turbid layer holds great promise for various biophotonics applications. Conventional wavefront shaping techniques aim to create and scan a focus spot through the turbid layer. Finding the correct input wavefront without direct access to the target plane remains a critical challenge. In this chapter, we explore a new strategy for imaging through turbid layer with a large field of view. In our setup, a fluorescence sample is sandwiched between two turbid layers. Instead of generating one focus spot via wavefront shaping, we use an unshaped beam to illuminate the turbid layer and generate an unknown speckle pattern at the target plane over a wide field of view. By tilting the input wavefront, we raster scan the unknown speckle pattern via the memory effect and capture the corresponding low-resolution fluorescence images through the turbid layer. Different from the wavefront-shaping-based single-spot scanning, the proposed approach employs many spots (i.e., speckles) in parallel for extending the field of view. Based on all captured images, we jointly recover the fluorescence object, the unknown optical transfer function of the turbid layer, the translated step size, and the unknown speckle pattern. Without direct access to the object plane or knowledge of the turbid layer, we demonstrate a 13-fold resolution gain through the turbid layer using the reported strategy. We also demonstrate the use of this technique to improve the resolution of a low numerical aperture objective lens allowing to obtain both large field of view and high resolution at the same time. The reported method provides insight for developing new fluorescence imaging platforms and may find applications in deep-tissue imaging.

5.1 Background

Imaging through turbid layer holds great promise for many biophotonics applications. Various approaches have been reported in recent years, including wavefront shaping techniques [1-9], measurement of the transmission matrix [10], object recovery from its autocorrelation [11, 12], accumulation of single-scattered waves [13], among others. In the context of wavefront shaping, a common strategy is to generate a pre-distorted wavefront that creates focus at the target plane. Since there is no direct access to the target plane, different guide stars can be used as reference beacons for wavefront shaping. Once the correct wavefront is found, the focus spot is raster scanned at the target plane using the optical memory effect [14-16]. Despite exciting progress on the development of wavefront shaping techniques, finding the correct wavefront without direct access to the target plane remains a challenge. In addition, the field of view is limited by the angular [14] or the translational range [15] of the single focused spot.

In this chapter, we explore a new strategy for improving imaging resolution through a turbid layer with a large field of view using speckle illumination and iterative recovery. Our setup is shown in Fig. 5-1(a), where a fluorescence sample is sandwiched between two turbid layers. Instead of generating one focus spot on the sample via wavefront shaping, we use an unshaped beam to illuminate the turbid layer and generate an unknown speckle pattern on the sample. By tilting the input wavefront, we then raster scan the unknown speckle pattern via the memory effect and capture the corresponding low-resolution fluorescence images through the turbid layer. Different from the wavefront-shaping-based single-spot scanning, the proposed approach employs many spots (i.e., speckles) in parallel. Based on all captured images, we jointly recover the fluorescence object and the unknown speckle pattern. Without direct access to the object plane or knowledge of the illumination pattern, we achieve one order of magnitude resolution enhancement using the reported strategy (Fig. 5-1(b)-(c), will be discussed later).

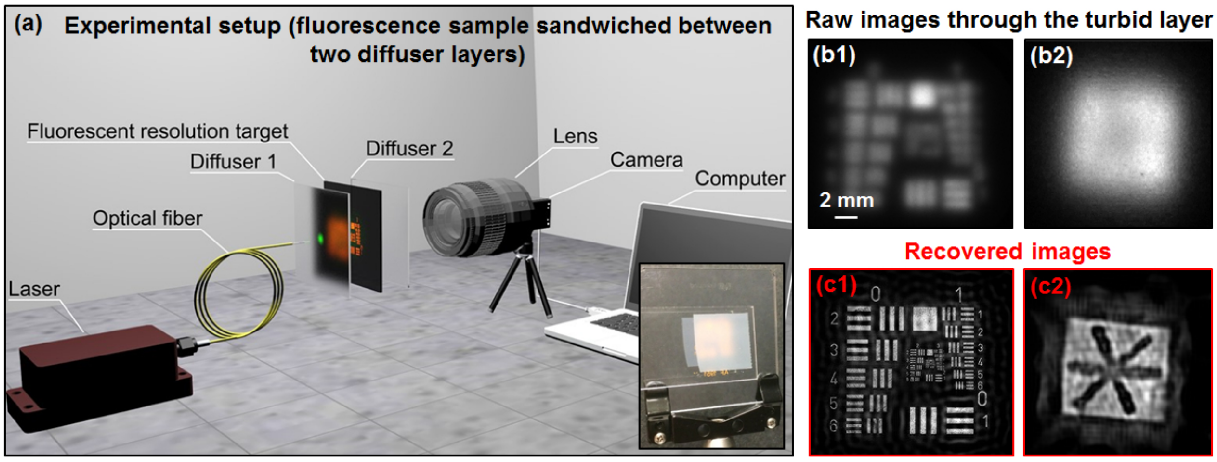

Figure 5-1: The reported strategy for imaging through turbid layer. (a) The experimental setup. The inset shows the fluorescence USAF target through the turbid layer (a scotch tape). (b) The captured raw fluorescence images through the turbid layer. (c) The recovered images with one order of magnitude resolution gain.

The use of illumination patterns to encode high-resolution information into low-resolution measurements is well-known and has been demonstrated in various types of structured illumination (SI) setups [16-21]. Typical linear SI techniques are targeted at 2-fold resolution improvement with known system point spread function (PSF). With certain support constraints, 3-fold resolution gain has been reported [22]. However, getting at least one order of magnitude resolution improvement with neither direct access to the targeted object nor the PSF has not been addressed before. In this work we explore such super resolution by relying on the memory effect which allows to obtain many images from a single unknown speckle pattern. This strategy is different from previous SI demonstrations which uses multiple speckle patterns and allows us to achieve more than one order of magnitude resolution gain without direct access to the object plane.

This chapter is structured as follows: in Section 5.2, we discuss the forward modeling and recovery methods of the reported scheme. Section 5.3 reports experimental results and demonstrates a 13-fold resolution gain through turbid layers. In Section 5.4, we discuss the use of

the proposed scheme to improve the resolution of a regular fluorescence microscope platform. We demonstrate the use of a 0.1 numerical aperture (NA) objective lens to achieve the resolution of a 0.4 NA. Finally, we summarize the results and discuss future directions in Section 5.5.

5.2 Modeling and simulation

We model the effect of the turbid layer in Fig. 5-1(a) as an unknown low-pass filter, with the point-spread-function (PSF) denoted as $PSF(x, y)$. In the acquisition process, the captured image can be expressed as

$$I_n(x,y) = (Object(x,y) \cdot P_{unknown}(x - x_n, y - y_n)) * PSF(x,y) \tag{5.1}$$

where $I_n(x, y)$ is the nth fluorescence intensity measurement (n = 1,2,3…), $Object(x, y)$ is the fluorescence object we wish to recover, $P_{unknown}(x, u)$ is the unknown illumination pattern on the sample, (x_n, y_n) is the nth positional shift of the illumination pattern, and '*' stands for convolution. In our experiment, we tilt the incident angle of the laser light to shift the unknown speckle pattern to different positions on the sample. For each position of the speckle pattern, the resulting fluorescence signal is detected through the turbid media (i.e., convolved with the PSF). The goal of our imaging scheme is to recover $Object(x, y)$ from many measurements $I_n(x, y)$ (n = 1, 2, 3…), a problem referred to as blind deconvolution.

In Eq. (5.1), there are four unknown terms in the right-hand side: the fluorescence object $Object(x, y)$, the illumination pattern generated by the turbid layer $P_{unknown}(x, y)$, the PSF of the turbid layer $PSF(x, y)$, and the step size of the positional shift. To jointly recover the first three unknown terms, we seek to minimize the cost function $\sum_n D_n$ where

$$D_n = | I_n(x,y) - (Object(x,y) \cdot P_{unknown}(x - x_n, y - y_n)) * PSF(x,y) |^2 \tag{5.2}$$

For efficient implementation, we perform stochastic gradient descent to update the three unknowns which leads to the iterations:

$$Object(x,y)^{update} = Object(x,y) - a \cdot \partial D_n / \partial Object \tag{5.3}$$

$$P_{unknown}(x-x_n, y-y_n)^{update} = P_{unknown}(x-x_n, y-y_n) - b \cdot \partial D_n / \partial P \tag{5.4}$$

$$PSF(x,y)^{update} = PSF(x,y) - c\frac{\partial D_n}{\partial PSF} \tag{5.5}$$

where 'a', 'b' and 'c' are step sizes. This stochastic gradient descent scheme is able to accelerate the recovery process [23, 24] and it is similar to our previous demonstrations of jointly recovering the object and speckle patterns [25, 26]. In our implementation, we choose

$$a = 1/\left|\max(P_{unknown}(x-x_n, y-y_n))\right|^2 \tag{5.6}$$

$$b = 1/\left|\max(Object(x,y))\right|^2 \tag{5.7}$$

$$c = 1/\left|\max(FT(Object(x,y)\cdot P_{unknown}(x-x_n, y-y_n)))\right|^2 \tag{5.8}$$

where *FT* denotes the Fourier transform. These step sizes are chosen based on the ptychographic algorithm [27] and are related to Lipschitz constants [28]. A detailed implementation can be found in the appendix.

We initialize the object by averaging all measurements, i.e., $Object(x,y) = \sum_n I_n / N$, where N is the total number of acquired images. We initialize the unknown pattern by setting it to an all-ones matrix. To initialize the unknown $PSF(x, y)$, we first perform a Fourier transform on the initialized object. We estimate the cutoff frequency f_{cutoff} to be the point where the Fourier spectrum intensity drops to 5% of its maximum. The *PSF* is then initialized as an Airy function with a cutoff frequency f_{cutoff}. To obtain the step size of the positional shift, we assume the step size is the same

for all measurements so that we only need to recover one parameter. In our implementation, we define the convergence index as the difference between the measurements and the generated low-resolution data from the recovery [29]. We then iterate over different step sizes and pick the one that generates the highest convergence index. Figure 5-2 summarizes the recovery process.

Algorithm outline

Input: Raw image sequence I_n $(n = 1,2,\cdots,N)$
Output: High-resolution object $O(x,y)$, unknown speckle pattern $P(x,y)$, and $PSF(x,y)$

Initialize $O(x,y)$, $P(x,y)$, $PSF(x,y)$, and the step size of positional shift
for $j = 1$:*loopNum*
  for $n = 1:N$
    update object: $O(x,y)^{update} = O(x,y) - a\frac{\partial D_n}{\partial O}$
    $= O(x,y) - a[(O(x,y) \cdot P_{unknown}(x - x_n, y - y_n)) * PSF(x,y) - I_n(x,y)]$
    $* PSF(x,y) \cdot P_{unknown}(x - x_n, y - y_n)$, with $a = 1/|\max(P_{unknown}(x - x_n, y - y_n))|^2$

    update pattern: $P_{unknown}(x - x_n, y - y_n)^{update} = P_{unknown}(x - x_n, y - y_n) - b\frac{\partial D_n}{\partial P}$
    $= P_{unknown}(x - x_n, y - y_n) - b[(O(x,y) \cdot P_{unknown}(x - x_n, y - y_n)) * PSF(x,y) - I_n(x,y)]$
    $* PSF(x,y) \cdot O(x,y)$, with $b = 1/|\max(Object(x,y))|^2$

    update PSF (we perform this in the Fourier domain): $PSF(x,y)^{update} = PSF(x,y) - c\frac{\partial D_n}{\partial PSF}$
    $= PSF(x,y) - c\,[(O(x,y) \cdot P_{unknown}(x - x_n, y - y_n)) * PSF(x,y) - I_n(x,y)]$
    $*(O(x,y) \cdot P_{unknown}(x - x_n, y - y_n))$, with $c = 1/|\max\left(FT\left(Object(x,y) \cdot P_{unknown}(x - x_n, y - y_n)\right)\right)|^2$
  end
end

Figure 5-2: Outline of the recovery process.

Figure 5-3 shows a simulation result of the resolution-improvement scheme. Figure 5-3(a) shows the simulated ground truth. We model the turbid layer as a low-pass filter for fluorescence emission of the object and Fig. 5-3(b) shows the low-resolution measurement through the turbid layer. Figures 5-3(c) and 5-3(d) show the recovered object and the unknown translated speckle patterns with different speckle NAs. The resolution of the raw image and the recovery can be quantified by the radius of the dashed lines in Fig. 5-3(b) and 5-3(c1)-(c3). The resolution improvement factor is shown in Fig. 5-3(e), where the resolution gain increases as the speckle pattern cutoff frequency increases. In our imaging setting, the detection NA is much smaller than

the speckle NA, and thus, the final achievable resolution is determined by the speckle NA. As shown in Fig. 5-3(e), we can achieve one order of magnitude resolution gain without knowledge of the speckle pattern or the system PSF.

For the unknown incoherent PSF, we assume it is shift-invariant across the entire field of view. As such, we only need to update one PSF in each iteration. In our implementation, the PSF updating process was performed in the Fourier domain, i.e., we updated the optical transfer function (OTF) of the turbid layer in each iteration. Figure 5-4(a) shows the ground-truth recovery assuming the OTF is known. Figure 5-4(b) and 5-4(c) show a comparison between the cases with and without the OTF updating process. In Fig. 5-4(b), we set the initial OTF cutoff frequency to be 1.5 times larger than that of the ground truth. By updating the OTF in the gradient descent process, we can recover both the object and the correct OTF in Fig. 5-4(b1) and 5-4(b2). Figure 5-4(b3) and 5-4(b4) show the results without updating the OTF. Similarly, we set the initial OTF cutoff frequency to be half of that of the ground truth in Fig. 5-4(c). Figure 5-4(c1) and 5-4(c2) show the results with the OTF updating process. Figure 5-4(c3) and 5-4(c4) show comparisons without updating the OTF.

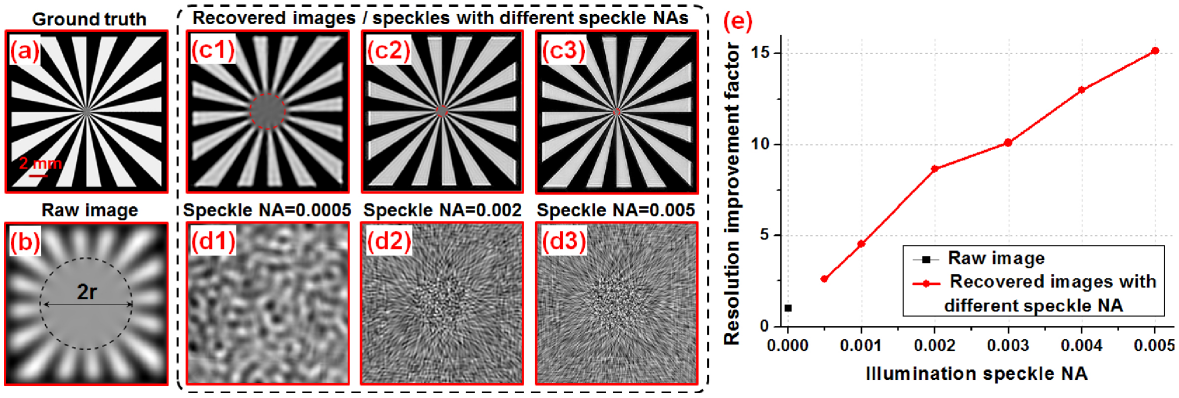

Figure 5-3: Simulation of the proposed strategy for improving resolution through turbid layer. (a) The simulation ground truth. (b) The simulated raw image through the turbid layer. (c) The recovered images with different speckle NAs. 81 by 81 raw

images are used for recovery in this simulation. (d) The recovered speckle patterns. (e) The resolution improvement factor as a function of different speckle NAs.

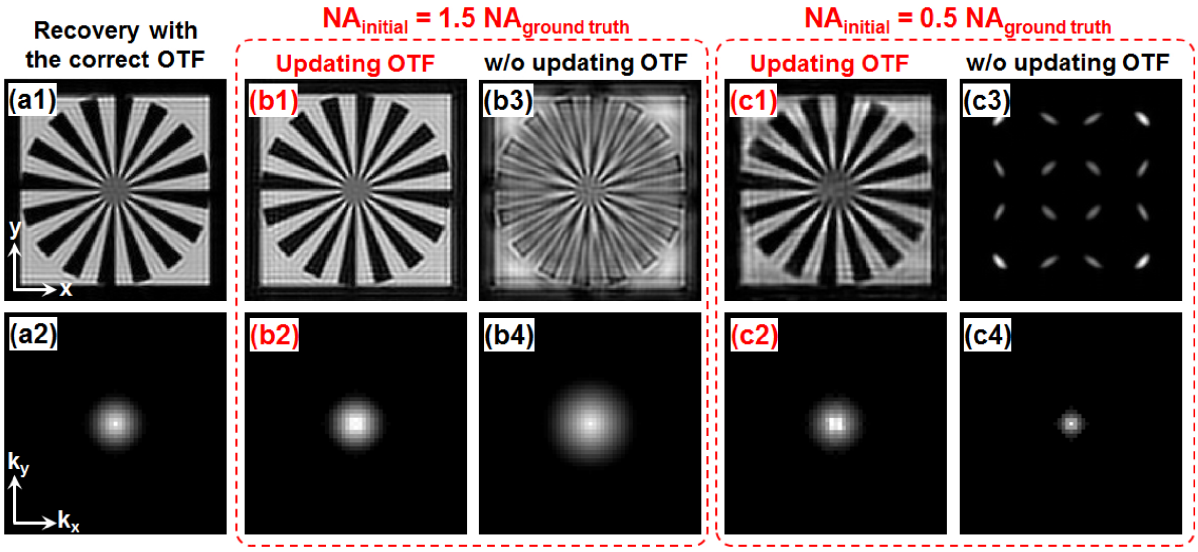

Figure 5-4: Simulation of the proposed strategy for updating the object (top row) and the unknown incoherent OTF (bottom row). (a) The ground-truth recovery assuming the OTF is known. (b) We set the cutoff frequency of the initial OTF to be 1.5 times larger than that of the ground truth. The results with (b1-b2) and without (b3-b4) the OTF updating process. (c) We set the cutoff frequency of the initial OTF to be half of that of the ground truth. The results with (c1-c2) and w/o (c3-c4) the OTF updating process.

Figure 5-5 shows the process for recovering the step size of the positional shift. Figure 5-5(a1)-(a3) shows the recovered object image with different step size errors. In Fig. 5-5(b1), the convergence index [29] increases as the loop number increases. To recover the step size, we iterate over different step sizes and pick the one that generates the highest convergence index, as shown in Fig. 5-5(b2).

In Fig. 5-6, we analyze the performance of the reported scheme with respect to the number of translated patterns and different noise levels. Figures 5-6(a1)-(a4) show the recovered object using different numbers of translated patterns. Figure 5-6(a5) quantifies the result using mean square

error (MSE) and structural similarity (SSIM) index. We can see that more translated patterns lead to improved image quality of the reconstruction (lower MSE and higher SSIM). The achievable resolution, on the other hand, is determined by the speckle size and remains the same in Fig. 5-6(a1)-(a4). In Fig. 5-6(b), we analyze the effect of additive noise. Different amounts of Gaussian noise are added into the simulated raw images. The reconstructed images are shown in Fig. 5-6(b1)-(b4). The corresponding MSEs and SSIMs are quantified in Fig. 5-6(b5). Evidently, the reported scheme is robust against additive noise.

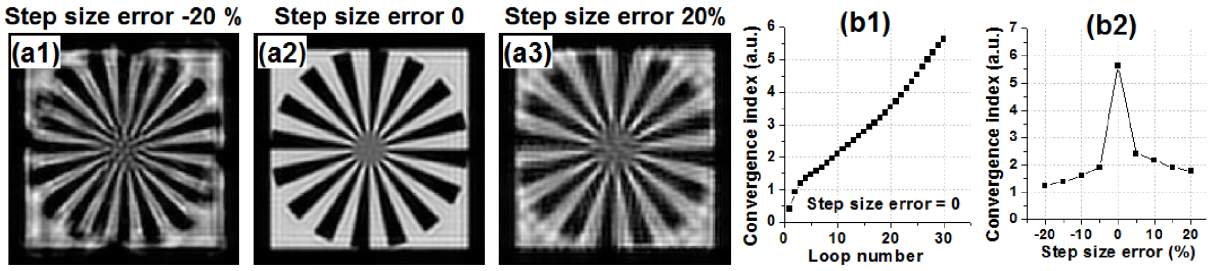

Figure 5-5: Simulation of the proposed strategy for recovering the step size. (a) The recovered object images with different step size errors. (b1) The convergence index as a function of loop number. (b2) The convergence index as a function of different step size. We pick the step size that generates the highest convergence index.

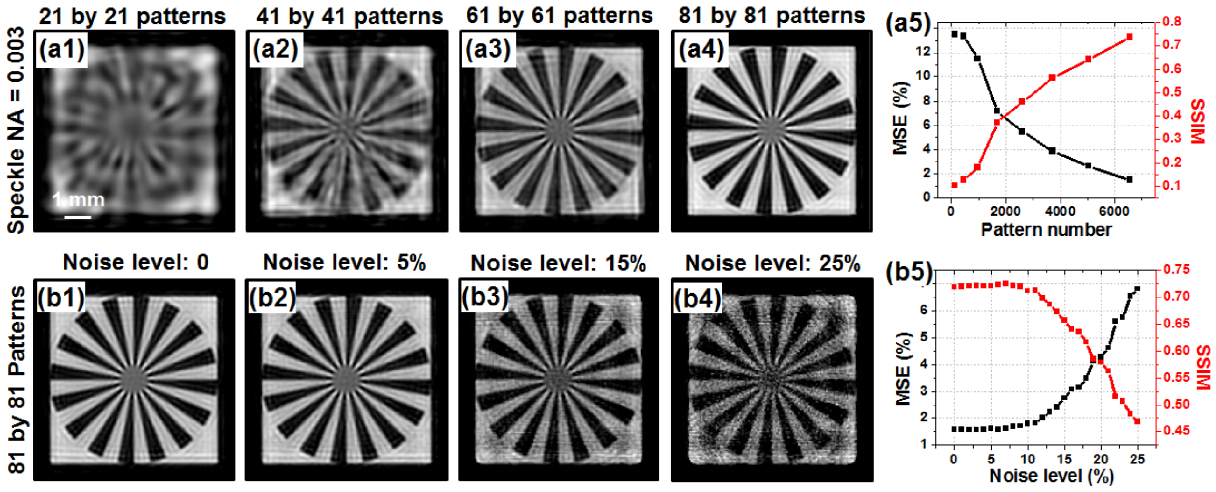

Figure 5-6: The performance of the reported scheme with different numbers of translated patterns and different noise levels. 81 by 81 raw images are used for recovery in this simulation. (a1)-(a4) Recovered object images with different numbers of translated patterns; the performance is quantified using SSIM and MSE in (a5). No noise is added into the raw images. (b1)-(b4) Recovered object images with different noise levels; the performance is quantified in (b5).

5.3 13-fold resolution gain through turbid layers

Next we consider experimental results using the setup in Fig. 5-1(a), where the fluorescence object is sandwiched between two turbid layers (two scotch tapes as shown in the inset of Fig. 5-1(a)). A 532-nm laser diode is coupled to a single mode fiber and illuminates the object with turbid layers. The fiber is 1 cm away from the first turbid layer. The distance between the object and first turbid layer is ~8 cm and the distance between the object and the second turbid layer is about ~2 cm. The 532-nm excitation light forms a random speckle pattern on the sample through the first turbid layer. The resulting fluorescence emission is low-pass filtered by the second turbid layer and detected by a camera with 550-nm long-pass filter and a photographic lens (Nikon 50mm f/1.2). In our implementation, we mechanically moved the fiber to different positions with a 0.5-μm motion step size and generated slightly tilted wavefronts for illumination. Based on the memory effect, the tilted wavefront laterally translates the unknown speckle pattern on the fluorescence object, resulting in the forward imaging model of Eq. (5.1).

In the first experiment, we use a fluorescence USAF target as the object. Figure 5-7(a) shows the raw fluorescence image through the turbid layer. Clearly no detail can be resolved from the fluorescence USAF resolution target. Figures 5-7(b) and 5-7(c) show the recovered image of the resolution target and Fig. 5-7(d) shows the recovered speckle patterns. Based on Fig. 5-7(a) and 5-7(c4), we achieve 13-fold resolution gain through the turbid layer using the reported strategy. In

the second experiment, we draw some lines on a fluorescence microsphere slide and use it as the object. Figure 5-8(a) depicts the raw fluorescence image through the turbid layer. Figure 5-8(b) demonstrates the ground truth image by removing the two turbid layers. Figure 5-8(c) and 5-8(d) show the recovered images and speckle patterns. The line features of the fluorescence object are clearly resolved from the recovered images.

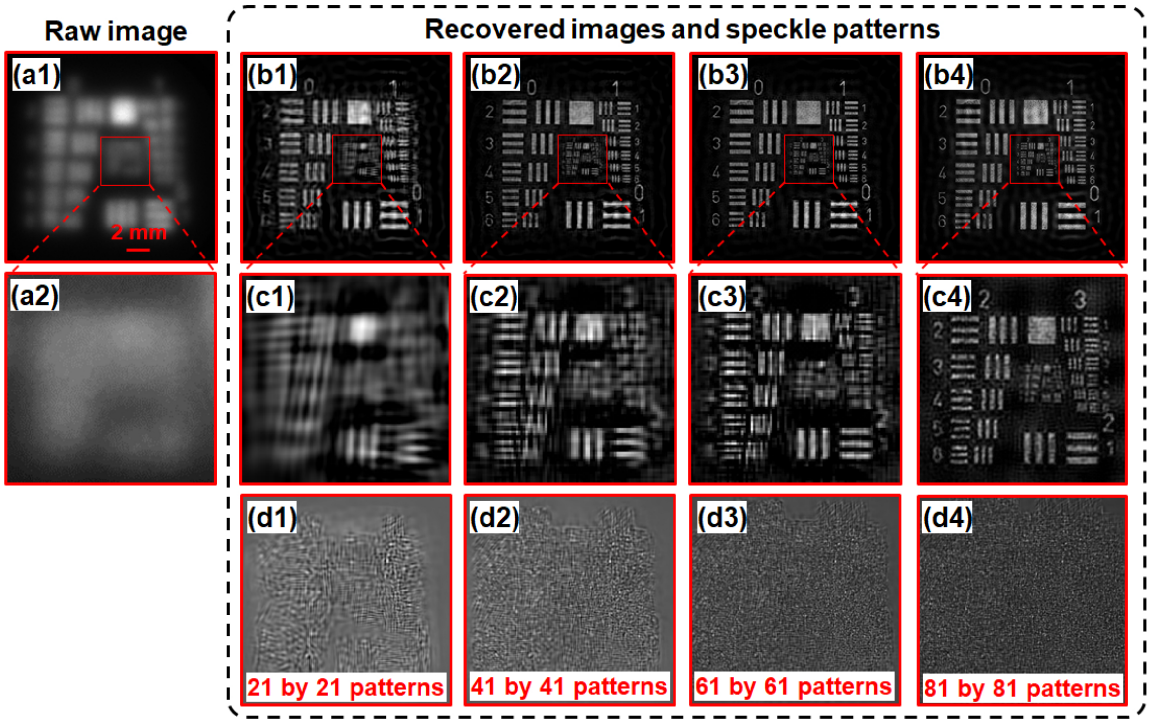

Figure 5-7: 13-fold resolution gain through the turbid layer. (a) The captured raw image through the turbid layers. (b) The recovered object image using different numbers of translated speckle patterns (refer to the bottom textbox of (d)). (c) Magnified views of (b). (d) The recovered speckle patterns corresponding to (b).

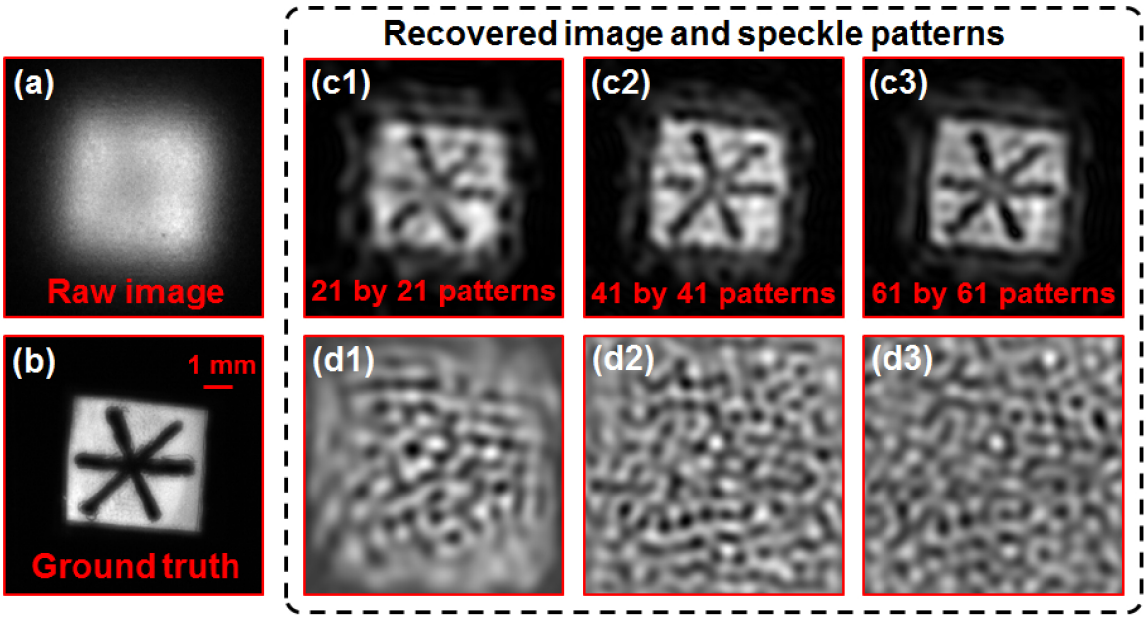

Figure 5-8: Experimental demonstration of the reported strategy using a fluorescence object. (a) The captured raw image through the turbid layers. (b) The ground truth image of the fluorescence object. (c) The recovered object images using a different number translated patterns. (d) The recovered speckle patterns corresponding to (c).

5.4 Wide-field, high-resolution fluorescence imaging

For many microscopy imaging applications, it is important to get both wide field of view and high resolution at the same time [30]. The reported scheme provides a potential solution to achieve this goal, as we show next.

In Fig. 5-9(a), we use a low-NA objective lens (4X, 0.1 NA) to acquire raw images of a sample and use a high-NA condenser lens (0.9 NA) to generate a speckle pattern on the object. A diffuser is placed at the back focal plane of the condenser lens in the setup. We also place an aperture stop at the center of the back focal plane of the condenser lens to block the direct-transmitted light to the fluorescence detection system (Fig. 5-9(a)). In this experiment, we translate the sample to 30 by 30 different positions with 0.3 μm step size and capture the corresponding images through the

0.1 NA objective lens. There is no scattering layer between the sample and the objective lens. The captured images are then used to recover both the high-resolution object and the unknown speckle pattern. Figure 5-9(b1) shows the captured raw image of a fluorescence resolution target. Figure 5-9(b2) and (b3) show the recovered object and the speckle pattern. The resolution of the recovered images corresponds to a NA of 0.4. The resolution improvement factor in this experiment is 4, limited by the precision of the employed motorized stage (Newport LTA-HS).

In Fig. 5-9(c), we demonstrate the use of the reported scheme to recover a wide-field, high-resolution fluorescence image of a microsphere sample. Figure 5-9(c1) depicts the recovered image where the field of view is determined by the employed 4X objective. Figure 5-9(c2) and 5-9(c3) show the recovered object image and the speckle pattern and Fig. 5-9(c4) shows the raw image captured using the 0.1 NA objective lens.

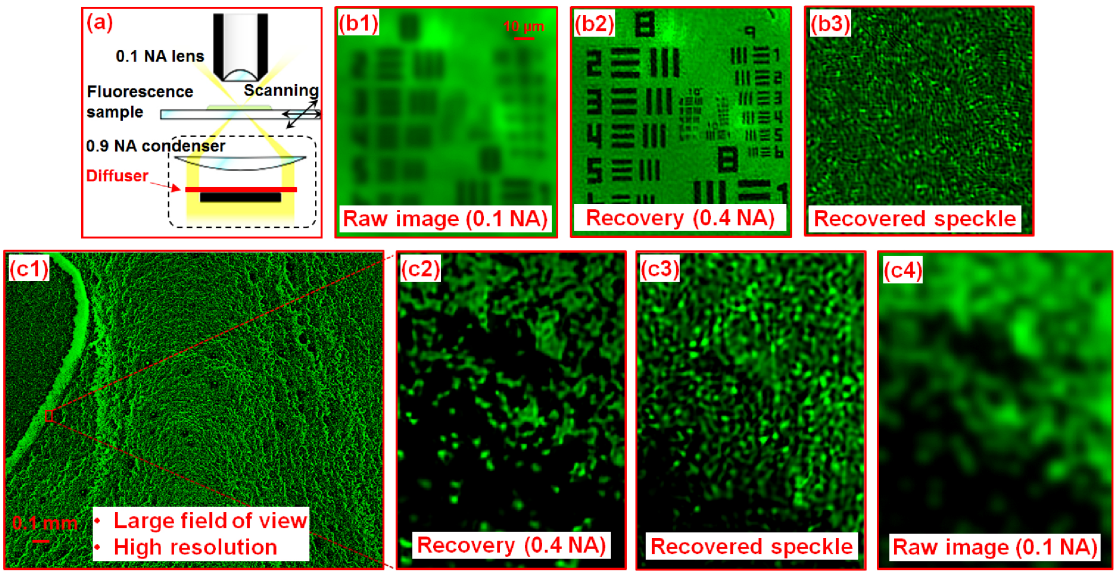

Figure 5-9: Wide-field, high-resolution fluorescence imaging using the reported strategy. (a) The experimental setup where we generate a high-NA speckle pattern on the sample. (b1) The captured raw image of the fluorescence resolution target. (b2)-(b3) The recovered object and the recovered speckle pattern. (c1) The wide-field, high-resolution fluorescence image recovered using the reported strategy.

(c2) The magnified view of the microspheres. (c3) The recovered speckle pattern corresponding to (c2). (c4) The raw image of (c2).

5.5 Discussion

We report a new strategy for improving fluorescence imaging resolution through a turbid layer with a large field of view. Instead of generating one focus spot on the sample via wavefront shaping, we use an unshaped beam to illuminate the turbid layer and generate an unknown speckle pattern on the sample. By tilting the input wavefront, we raster scan the unknown speckle pattern via the memory effect and capture the corresponding low-resolution fluorescence images through the turbid layer. Without direct access to the object plane or knowledge of the illumination pattern, we achieve 13-fold resolution gain using the reported strategy. While the idea of structured illumination is well-known for improving resolution in microscopy platform, previous demonstrations, to the best of our knowledge, are targeted at 2-fold resolution gain with a known system PSF. In this work we explore super resolution by relying on the memory effect which allows to obtain many images from a single unknown speckle pattern. This strategy is different from previous SI demonstrations which uses multiple speckle patterns [18, 21] and allows us to achieve more than one order of magnitude resolution gain without direct access to the object plane. Our work shares some roots with Refs. [11, 12] which recover the object from its autocorrelation measurements. In our work, we use a joint object-pattern recovery scheme to reconstruct both the object and the pattern. The scattering layer may not be needed in our scheme and we demonstrate the use of a 0.1 NA objective lens to obtain a 0.4-NA resolution with a large field of view.

The limitations of the reported strategy are threefold. First, it is based on the traditional memory effect where the target plane is at a distance from the diffusing layer. For imaging inside thick scattering media, we may need to exploit the translational memory effect [15] for the reported

scheme. Second, we need a large number of acquisitions in the reconstruction process. This may be due to the low modulating efficiency for converting the high-frequency information to the low-frequency band, especially when we aim at one order of magnitude resolution gain. Third, we assume the PSF is shift-invariant in the recovery process. If needed, we can divide the captured images into many smaller segments, and jointly recover the object, the illumination pattern and the PSF for each segment. This is similar to the pupil recovery process in Fourier ptychographic microscopy, where the pupil aberrations are recovered at different spatial locations independently [30, 31].

There are also a few directions for improving the reported scheme. First, we can use a scanning galvo mirror to better control the tilted beam and achieve better positional accuracy. Second, we can employ motion correction [32] in the reconstruction process to address the positional error of the scanning process. Third, we may incorporate support constraints [22] including signal sparsity [33, 34] in the reconstruction to reduce the number of acquisitions. Fourth, multi-layer modeling [35] can be integrated into the reported scheme to handle 3D fluorescence sample.

Bibliography

[1] I. M. Vellekoop and C. M. Aegerter, "Scattered light fluorescence microscopy: imaging through turbid layers," Optics letters 35, 1245-1247 (2010).
[2] I. M. Vellekoop, "Feedback-based wavefront shaping," Optics express 23, 12189-12206 (2015).
[3] M. Nixon, O. Katz, E. Small, Y. Bromberg, A. A. Friesem, Y. Silberberg, and N. Davidson, "Real-time wavefront shaping through scattering media by all-optical feedback," Nat Photon 7, 919-924 (2013).
[4] A. P. Mosk, A. Lagendijk, G. Lerosey, and M. Fink, "Controlling waves in space and time for imaging and focusing in complex media," Nature photonics 6, 283-292 (2012).
[5] X. Xu, H. Liu, and L. V. Wang, "Time-reversed ultrasonically encoded optical focusing into scattering media," Nature photonics 5, 154-157 (2011).
[6] Y. M. Wang, B. Judkewitz, C. A. DiMarzio, and C. Yang, "Deep-tissue focal fluorescence imaging with digitally time-reversed ultrasound-encoded light," Nature communications 3, 928 (2012).

[7] O. Katz, E. Small, and Y. Silberberg, "Looking around corners and through thin turbid layers in real time with scattered incoherent light," Nature photonics 6, 549-553 (2012).
[8] J.-H. Park, C. Park, H. Yu, J. Park, S. Han, J. Shin, S. H. Ko, K. T. Nam, Y.-H. Cho, and Y. Park, "Subwavelength light focusing using random nanoparticles," Nature photonics 7, 454-458 (2013).
[9] J. Tang, R. N. Germain, and M. Cui, "Superpenetration optical microscopy by iterative multiphoton adaptive compensation technique," Proceedings of the National Academy of Sciences 109, 8434-8439 (2012).
[10] S. M. Popoff, G. Lerosey, R. Carminati, M. Fink, A. C. Boccara, and S. Gigan, "Measuring the Transmission Matrix in Optics: An Approach to the Study and Control of Light Propagation in Disordered Media," Physical Review Letters 104, 100601 (2010).
[11] J. Bertolotti, E. G. van Putten, C. Blum, A. Lagendijk, W. L. Vos, and A. P. Mosk, "Non-invasive imaging through opaque scattering layers," Nature 491, 232-234 (2012).
[12] O. Katz, P. Heidmann, M. Fink, and S. Gigan, "Non-invasive single-shot imaging through scattering layers and around corners via speckle correlations," Nature photonics 8, 784-790 (2014).
[13] S. Kang, S. Jeong, W. Choi, H. Ko, T. D. Yang, J. H. Joo, J.-S. Lee, Y.-S. Lim, Q.-H. Park, and W. Choi, "Imaging deep within a scattering medium using collective accumulation of single-scattered waves," Nature Photonics 9, 253-258 (2015).
[14] I. Freund, M. Rosenbluh, and S. Feng, "Memory effects in propagation of optical waves through disordered media," Physical review letters 61, 2328 (1988).
[15] B. Judkewitz, R. Horstmeyer, I. M. Vellekoop, I. N. Papadopoulos, and C. Yang, "Translation correlations in anisotropically scattering media," Nature physics 11, 684-689 (2015).
[16] G. Osnabrugge, R. Horstmeyer, I. N. Papadopoulos, B. Judkewitz, and I. M. Vellekoop, "Generalized optical memory effect," Optica 4, 886-892 (2017).
[17] M. G. Gustafsson, "Surpassing the lateral resolution limit by a factor of two using structured illumination microscopy," Journal of microscopy 198, 82-87 (2000).
[18] E. Mudry, K. Belkebir, J. Girard, J. Savatier, E. Le Moal, C. Nicoletti, M. Allain, and A. Sentenac, "Structured illumination microscopy using unknown speckle patterns," Nature Photonics 6, 312-315 (2012).
[19] N. Chakrova, B. Rieger, and S. Stallinga, "Deconvolution methods for structured illumination microscopy," JOSA A 33, B12-B20 (2016).
[20] H. Yilmaz, E. G. van Putten, J. Bertolotti, A. Lagendijk, W. L. Vos, and A. P. Mosk, "Speckle correlation resolution enhancement of wide-field fluorescence imaging," Optica 2, 424-429 (2015).
[21] L.-H. Yeh, L. Tian, and L. Waller, "Structured illumination microscopy with unknown patterns and a statistical prior," Biomedical optics express 8, 695-711 (2017).
[22] J. Min, J. Jang, D. Keum, S.-W. Ryu, C. Choi, K.-H. Jeong, and J. C. Ye, "Fluorescent microscopy beyond diffraction limits using speckle illumination and joint support recovery," Scientific Reports 3, 2075 (2013).
[23] N. Chakrova, B. Rieger, and S. Stallinga, "Deconvolution methods for structured illumination microscopy," Journal of the Optical Society of America A 33, B12-B20 (2016).
[24] N. Chakrova, R. Heintzmann, B. Rieger, and S. Stallinga, "Studying different illumination patterns for resolution improvement in fluorescence microscopy," Optics express 23, 31367-31383 (2015).
[25] S. Dong, P. Nanda, R. Shiradkar, K. Guo, and G. Zheng, "High-resolution fluorescence imaging via pattern-illuminated Fourier ptychography," Optics Express 22, 20856-20870 (2014).

[26] S. Dong, P. Nanda, K. Guo, J. Liao, and G. Zheng, "Incoherent Fourier ptychographic photography using structured light," Photon. Res. 3, 19-23 (2015).
[27] A. M. Maiden and J. M. Rodenburg, "An improved ptychographical phase retrieval algorithm for diffractive imaging," Ultramicroscopy 109, 1256-1262 (2009).
[28] R. Hesse, D. R. Luke, S. Sabach, and M. K. Tam, "Proximal heterogeneous block implicit-explicit method and application to blind ptychographic diffraction imaging," SIAM Journal on Imaging Sciences 8, 426-457 (2015).
[29] Z. Bian, S. Dong, and G. Zheng, "Adaptive system correction for robust Fourier ptychographic imaging," Optics Express 21, 32400-32410 (2013).
[30] G. Zheng, R. Horstmeyer, and C. Yang, "Wide-field, high-resolution Fourier ptychographic microscopy," Nature Photonics 7, 739-745 (2013).
[31] X. Ou, G. Zheng, and C. Yang, "Embedded pupil function recovery for Fourier ptychographic microscopy," Optics Express 22, 4960-4972 (2014).
[32] L. Bian, G. Zheng, K. Guo, J. Suo, C. Yang, F. Chen, and Q. Dai, "Motion-corrected Fourier ptychography," Biomedical Optics Express 7, 4543-4553 (2016).
[33] E. Hojman, T. Chaigne, O. Solomon, S. Gigan, E. Bossy, Y. C. Eldar, and O. Katz, "Photoacoustic imaging beyond the acoustic diffraction-limit with dynamic speckle illumination and sparse joint support recovery," Optics Express 25, 4875-4886 (2017).
[34] Y. C. Eldar and G. Kutyniok, Compressed sensing: theory and applications (Cambridge University Press, 2012).
[35] S. Dong, K. Guo, S. Jiang, and G. Zheng, "Recovering higher dimensional image data using multiplexed structured illumination," Optics Express 23, 30393-30398 (2015).

Chapter 6 Higher dimensional imaging with multiplexed structured illumination

Structured illumination (SI) using non-uniform intensity patterns is well-known for improving lateral resolution in microscopy. In this chapter, we propose a multiplexed SI technique for recovering images with higher lateral resolution and with higher dimensional information at the same time. We use unknown non-uniform intensity patterns for incoherent sample illumination and use the corresponding acquisitions for image recovery. In the first example, we use the reported framework to recover sample images with higher lateral resolution and separate different sections of the sample along the z-direction. In the second example, we recover the sample images with higher lateral resolution and separate the images at different spectral bands. The reported multiplexed-SI framework may find applications in general imaging settings where higher dimensional information is mixed in 2D image measurements. It can also be used in microscopy settings for computational sectioning and multispectral imaging.

6.1 Background

Higher information content in images is desired in many application areas. However, typical images are in 2D and represent a mixture of higher dimensional data. Dedicated hardware is needed to separate the mixture and fit it into a higher dimensional data cube (such as 3D confocal imaging and multispectral imaging). We consider an example of fluorescence microscopy, where the emission from the sample is captured by a 2D image sensor. The captured 2D image represents a mixture of 2D data at different z-sections and a mixture of 2D data at different wavelengths. The information at different z-sections and at different spectral bands are considered higher dimensional data in this case.

In this chapter, we explore a multiplexed framework for recovering sample images with higher lateral resolution and with higher dimensional information at the same time. The reported framework, termed multiplexed structure illumination (multiplexed-SI), builds upon the conventional structured illumination (SI) technique, where non-uniform intensity patterns are used for sample illumination and the corresponding acquisitions are used for image recovery [1, 2]. In a typical implementation of SI, sinusoidal patterns are used for modulating the high-frequency component into the passband of the objective lens. Therefore, the recorded images contain sample information that is beyond the resolution limit of the employed optics [1, 2]. Along the same line, speckle patterns have been used in SI for the same purpose. Resolution improvement has been demonstrated using different reconstruction methods, including phase retrieval, optimization, Bayes estimation and etc [3-13]. However, to the best of our knowledge, these different techniques are mainly targeted at resolution improvement and the acquired images have not been modeled as a mixture of higher dimensional data. We propose a multiplexed framework that allows us to improve the lateral resolution and to recover higher dimensional data at the same time. The reported multiplexed-SI framework may find applications in general incoherent imaging settings where higher dimensional data is mixed in 2D image measurements.

6.2 Multiplexed structured illumination

The basic idea of the reported multiplexed-SI framework is shown in Fig. 6-1. Similar to the concept of conventional SI, we use unknown speckle patterns for sample illumination. The captured images are then used to recover sample images with higher lateral resolution and with higher dimensional information. Fig. 6-1(a) shows the case of recovering different z sections of the sample and Fig. 6-1(b) shows the case of recovering images at different spectral bands. The forward imaging model of these two cases can be described as follows:

$$\mathrm{F}\left(I_n\right)=\sum_m OTF_m \cdot \mathrm{F}\left(I_{obj\_m}\cdot P_{mn}\right) \tag{6.1}$$

where F stands for Fourier transform, *In* stands for 2D image measurements, *OTFm* stands for the optical transfer function (OTF) of the objective lens (a known parameter in our implementation), *Iobj_m* stands for the ground-truth image of the sample, and *Pmn* stands for illumination patterns. In Eq. (6.1), the summation over subscript '*m*' stands for the mixture of higher dimensional data. For example, we can model the captured images *In* as a summation of red, green, blue channels with m=1, m=2, and m=3. The second example is to model the captured images as a summation of *m* different 2D sections along the z direction. In Eq. (6.1), we assume the no interaction between different incoherent modes. For each mode '*m*', we have '*n*' different intensity patterns for sample illumination, and thus, we have two subscripts for '*Pmn*'. In our implementation, we will translate the unknown illumination pattern to '*n*' different spatial positions to get the corresponding 2D image measurements. As a result, we only have '*m*' unknown illumination patterns. The goal here is to recover different modes of the object *Iobj_m* as well as the unknown illumination patterns *Pmn* (m=1,2…) from the 2D image measurements *In*. If m=1, Eq. (6.1) reduces to the forward imaging model of conventional SI [3, 4, 13].

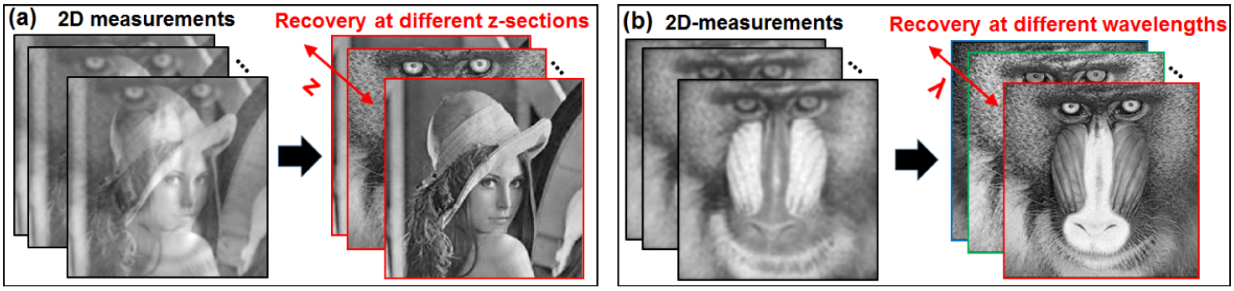

Figure 6-1: Images corresponding to different illumination patterns are used to recover resolution-enhanced images at different z sections (a) and at different wavelengths (b).

The recovery process is inspired and modified from the mode multiplexing and decomposition scheme in ptychography [14-16]. It starts with initial guesses of the different modes of the object *Iobj_m* and the unknown illumination pattern *Pmn* (m=1,2…). We first define *Ipm* and *Itm* as follows: $I_{pm} = I_{obj\_m} \cdot P_{mn}$ and $\mathrm{F}\left(I_{tm}\right) = OTF_m \cdot \mathrm{F}\left(I_{pm}\right)$. Based on these definitions and the measurements *In*, we have the following updating procedures for mode *m* of the object and the unknown illumination pattern (the illumination pattern is different for different modes):

$$I_{tm}^{update} = \frac{I_{tm} \cdot I_n}{\sum_m I_{tm}} \tag{6.2}$$

$$\mathrm{F}\left(I_{pm}^{updated}\right) = \mathrm{F}\left(I_{pm}\right) + OTF_m \cdot \left(\mathrm{F}\left(I_{tm}^{updated}\right) - \mathrm{F}\left(I_{tm}\right)\right) \tag{6.3}$$

$$I_{obj\_m}^{updated} = I_{obj\_m} + \frac{P_{mn}}{(\max(P_{mn}))^2}(I_{pm}^{updated} - I_{pm}) \tag{6.4}$$

$$P_{mn}^{updated} = P_{mn} + \frac{I_{obj\_m}^{updated}}{(\max(I_{obj\_m}^{updated}))^2}(I_{pm}^{updated} - I_{pm}) \tag{6.5}$$

Eq. (6.2)-(6.5) represent 4**m* equations. The updating process will be repeated for all n measurements and the entire process is terminated until convergence, which can be measured by the difference between two successive recoveries. In a practical implementation, we can simply terminate it with a predefined loop number, typically 10-100. We can draw connections between the above procedures and the ptychography approach [14, 15]. The key part of ptychography algorithms is an operation called Fourier magnitude projection, where the magnitude of exit wave estimate is replaced by the square root of measured intensity and the phase is kept unchanged. In multi-state ptychography, the summation of all coherent state's amplitude is used in the replacement process of Fourier magnitude projection. Here, in the case of incoherent imaging, we only consider intensity of the images, and we used Eq. (6.2) as an updating process

that is similar to the Fourier magnitude projection in ptychography [14, 15]. The rest of the equations are the same as those reported in Ref. [4].

We will validate the reported approach with two simulations. In the first simulation, we assume a two-layer object is separated by 6 microns and a 0.3 numerical aperture (NA) objective is used for image acquisition. We assume the NA of speckle pattern is 0.9 (can be generated by large-angle interference). We propagate the light field of the speckle to the two corresponding z-sections. We then multiply the intensity of the speckle patterns to the two object sections. We sum the resulting intensity from the two sections and low-pass filter it with the objective. Fig. 6-2(a) shows the raw image under speckle illumination. We can see that, the raw image contains information of the two sections at different z positions (Fig. 6-2(b1) and 6-2(c1)). In this simulation, we translate the speckles to 220 different positions and generate the corresponding low-resolution images. The recovered images and speckles are shown in Fig. 6-2(b2)-(b3) and 6-2(c2)-(c3). We can see that, the reported framework is able to separate the two sections and improve the lateral resolution. In Fig. 6-2(d1), we use mean square error (MSE) to characterize the imaging performance as a function of different noise level. We can see that, the performance gradually degrades as the noise increases. In Fig. 6-2(d2) and 6-2(d3), we plotted the MSE as a function of pattern number (with a loop number of 75) and loop number (with a pattern number of 220). We note that, the sectioning effective of conventional SI technique is to recover one section of the 3D sample. The reported approach, on the other hand, is able recover multiple sections and improve lateral resolution at the same time.

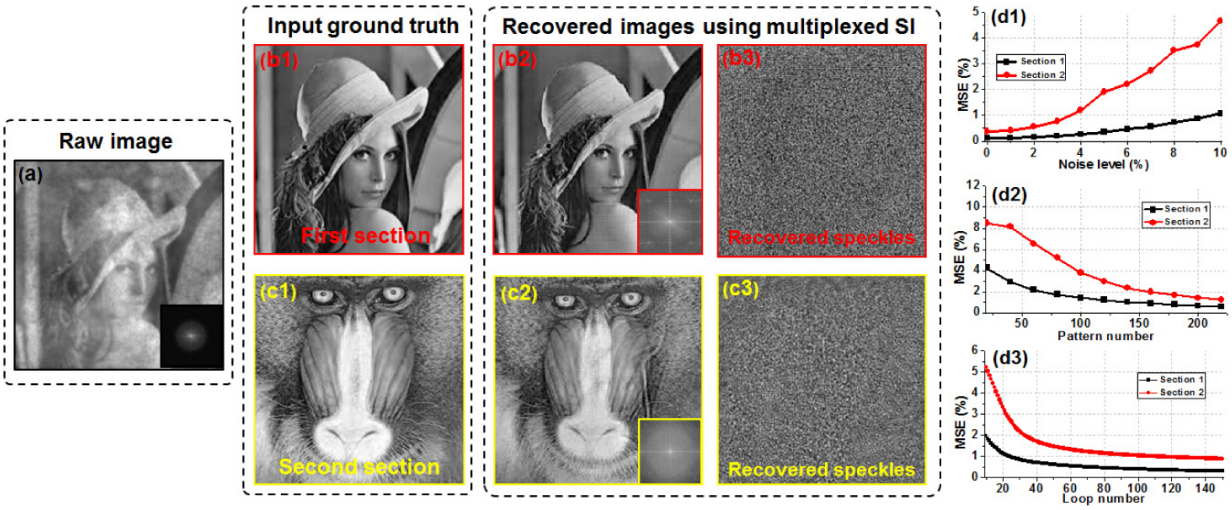

Figure 6-2: Image recovery of different z sections using the multiplexed-SI scheme. (a) The low-resolution acquisition under unknown speckle illumination and its Fourier spectrum. (b1) and (c1): the input ground truth at two different z sections. (b2) and (c2): the recovered images using the multiplexed-SI. (b3) and (c3): the recovered speckles at two different z-sections. The MSE is plotted as a function as noise (d1), pattern number (d2), and loop number (d3).

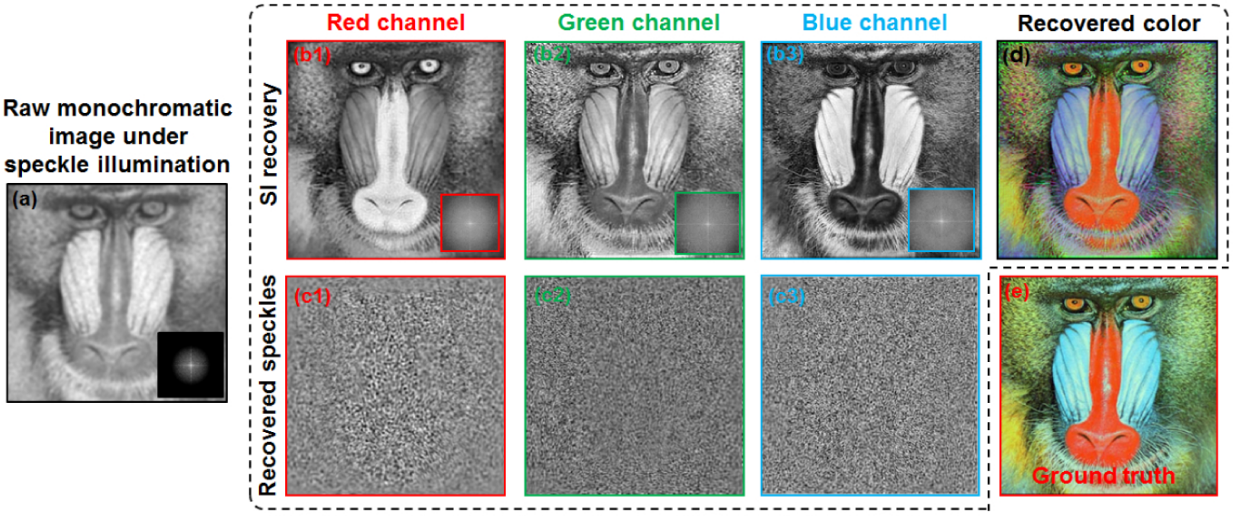

Figure 6-3: Image recovery of different spectral bands using the multiplexed-SI scheme. (a) The low-resolution acquisition under unknown speckle illumination. Inset shows the corresponding Fourier spectrum. The recovered images (b) and

speckles (c) using the multiplexed-SI with 50 loops. (d) The recovered color image by combining three channels. (e) The input ground truth.

In the second simulation, we assume the object contains three different color channels (red, green, and blue), and the captured images represent a mixture of these three channels, as described by Eq. (6.1). Fig. 6-3(a) shows the raw image under speckle illumination and the corresponding Fourier spectrum. We have added 1% noise in the raw images in this simulation. For the monochromatic raw image in Fig. 6-3(a), we cannot see any spectral information of the sample. We then translate the speckle patterns to 220 different positions and generate the corresponding mixtures similar to the first example. The recovered objects and speckles using the multiplexed-SI scheme are shown in Fig. 6-3(b) and 6-3(c). The recovered color combination and the ground truth of the three-color channels are shown in Fig. 6-3(d)-(e).

6.3 Higher dimensional imaging demonstration

We have performed two experiments to validate the reported imaging scheme. The first experiment aims to separate spectral bands using the proposed multiplexed-SI. As shown in Fig. 6-4(a), we used a video projector to project an unknown color speckle patterns and translate it to 114 positions. We used a monochromatic CCD camera to capture the corresponding images. Fig. 6-4(b) shows a low-resolution monochromatic image of the color object. Figure 6-4(c1)-(c3) shows the color channels of the object under uniform R/G/B illuminations. Figure 6-4(d1)-(d3) show the recovered red, green, blue channels using the multiplexed-SI scheme. Figure 6-4(e1)-(e3) show the recovered speckles. In Fig. 6-4(c4) and (d4), we combined the three channels and show the comparison between the color image under uniform illumination and the multiplexed-SI recovery. The high-resolution ground truth is shown in Fig. 6-4(f). The corresponding line traces are also shown for comparison in Fig. 6-4(g). Based on the dip-to-dip feature (~0.4 mm) highlighted in Fig. 6-4(g), the effective NA is ~0.00058 and it is ~1.7 times higher than the measured NA of the imaging

system. We can see that, the multiplexed-SI scheme is able to recover the color image of the sample using monochromatic acquisitions and achieve resolution improvement.

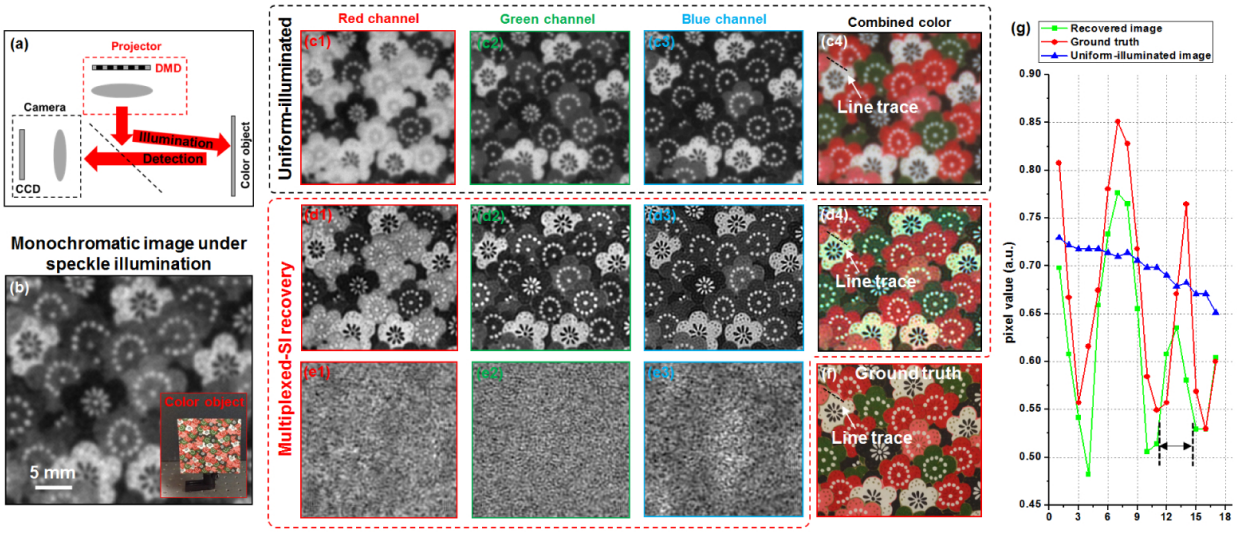

Figure 6-4: Experimental validation of the multiplexed-SI scheme. (a) The experimental setup. A video projector is used to project translated unknown color speckles on the sample. (b) The raw monochromatic acquisition of the color object (Visualization 1). (c) The images under uniform illumination. The multiplexed-SI recovered images (d) and speckle patterns (e). We used 20 loops for recovery. (f) The ground truth of the object. (g) Lines traces of (c4), (d4), and (f).

The second experiment aims to separate two different sections using the multiplexed-SI scheme. We used two pathology sections as the object and put this object close to a diffuser. The transmitted light from the diffuser forms speckles patterns on the two-layer object. Since the diffuser is placed closer to layer 1, the projected pattern on layer 1 is denser than that on layer 2. We then translated the object to 224 different positions and captured the corresponding image using a microscope system with two Nikon photographic lenses (with a NA of 0.005), as shown in Fig. 6-5(a) and (b). Fig. 6-5(c1)-(c3) show the uniform-illumined image, our recovery, and the ground truth of layer 1 respectively. Fig. 6-5(d) shows the images of layer 2. The line traces of a small feature is shown in Fig. 6-5(e) for comparison. For Fig. 6-5(c1) and (d1), we removed the other layer to capture images of the single layer (layer 2 is in-focus and layer 1 is out-of-focus).

We can see that, the proposed imaging scheme is able to recover information in z-direction and improve the resolution. We can also see that, the shadow from layer 1 can be seen from the layer-2 recovery in Fig. 6-5(d2). This effect is due to the fact that we does not model the interaction between different modes.

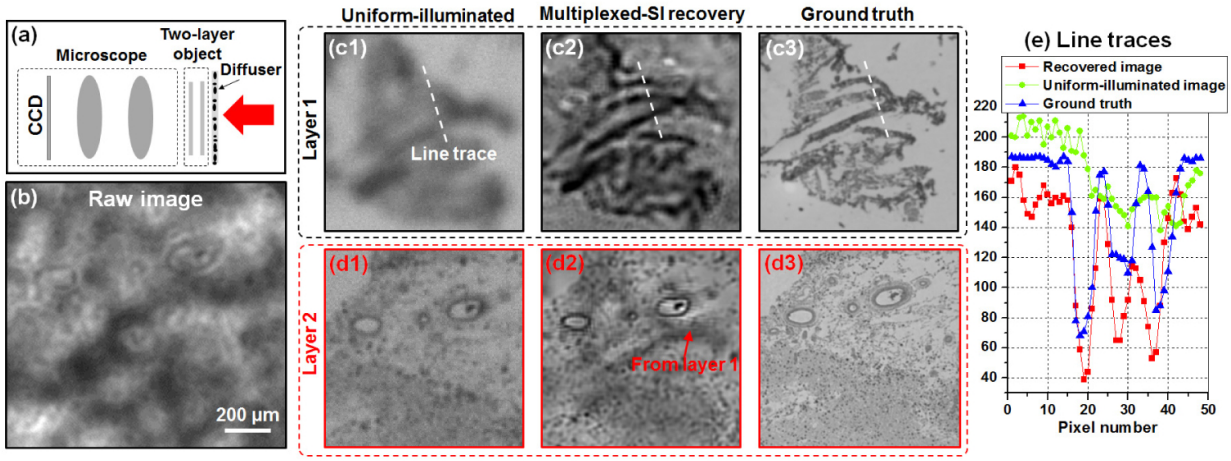

Figure 6-5: (a) Imaging setup, where a two-layer was used as the object. (b) The captured raw image with 0.005 NA, representing incoherent mixture of the two sections. Uniform-illuminated, our recovery, ground truth of layer 1 (c1)-(c3) and layer 2 (d1)-(d3). We used 30 loops in the recovery process. (e) Line traces of small features in (c1)-(c3).

6.4 Discussion

We have discussed an imaging framework for recovering higher dimensional image data and improving lateral resolution at the same time. In the reported framework, unknown speckle patterns are used for incoherent sample illumination and the corresponding acquisitions are used for information recovery. The major contribution of this work is to model the acquired images as an incoherent mixture of higher dimensional data. To the best of our knowledge, this is new to the structure illumination technique and may find broad applications in incoherent imaging settings where higher dimensional information is mixed in 2D image measurements.

There are several future directions of the reported multiplexed-SI framework. 1) In the reported framework, we did not model the interaction between different modes in the mixture. In other words, we assume different modes are independent of each other. This assumption is valid for information at different spectral bands. For information at different z sections, this assumption is only valid for transparent sample, where emission from one section is independent of other sections. If we can model the interaction between different modes [17], we may be able to extend the reported scheme to handle diffused samples. 2) The relationship between the number of raw image acquisitions and the number of modes we can model in the mixture is currently unknown. This relationship may depend on the information redundancy of different modes. Further research is needed. 3) In the reported framework, we assume the optical transfer function for different imaging modes is known. We can also add one updating step to refine the OTF in the iterative process, similar to Eq. (6.4)-(6.5). Updating OTF in the iterative process may be useful to handle unknown sample-induced aberrations.

Bibliography

[1] M. G. Gustafsson, "Surpassing the lateral resolution limit by a factor of two using structured illumination microscopy," Journal of microscopy 198, 82-87 (2000).

[2] M. G. Gustafsson, L. Shao, P. M. Carlton, C. R. Wang, I. N. Golubovskaya, W. Z. Cande, D. A. Agard, and J. W. Sedat, "Three-dimensional resolution doubling in wide-field fluorescence microscopy by structured illumination," Biophysical journal 94, 4957-4970 (2008).

[3] E. Mudry, K. Belkebir, J. Girard, J. Savatier, E. Le Moal, C. Nicoletti, M. Allain, and A. Sentenac, "Structured illumination microscopy using unknown speckle patterns," Nature Photonics 6, 312-315 (2012).

[4] S. Dong, P. Nanda, R. Shiradkar, K. Guo, and G. Zheng, "High-resolution fluorescence imaging via pattern-illuminated Fourier ptychography," Optics Express 22, 20856-20870 (2014).

[5] H. Yilmaz, E. G. van Putten, J. Bertolotti, A. Lagendijk, W. L. Vos, and A. P. Mosk, "Speckle correlation resolution enhancement of wide-field fluorescence imaging," Optica 2, 424-429 (2015).

[6] J. Min, J. Jang, D. Keum, S.-W. Ryu, C. Choi, K.-H. Jeong, and J. C. Ye, "Fluorescent microscopy beyond diffraction limits using speckle illumination and joint support recovery," Scientific reports 3(2013).

[7] O. Wagner, A. Schwarz, A. Shemer, C. Ferreira, J. García, and Z. Zalevsky, "Superresolved imaging based on wavelength multiplexing of projected unknown speckle patterns," Applied Optics 54, D51-D60 (2015).

[8] S. Dong, P. Nanda, K. Guo, J. Liao, and G. Zheng, "Incoherent Fourier ptychographic photography using structured light," Photon. Res. 3, 19-23 (2015).
[9] C. B. Müller and J. Enderlein, "Image Scanning Microscopy," Physical Review Letters 104, 198101 (2010).
[10] G. P. J. Laporte, N. Stasio, C. J. R. Sheppard, and D. Psaltis, "Resolution enhancement in nonlinear scanning microscopy through post-detection digital computation," Optica 1, 455-460 (2014).
[11] I. J. Cox, C. J. Sheppard, and T. Wilson, "Super-resolution by confocal fluorescent microscopy," Optik 60, 391-396 (1982).
[12] A. Jost, E. Tolstik, P. Feldmann, K. Wicker, A. Sentenac, and R. Heintzmann, "Optical Sectioning and High Resolution in Single-Slice Structured Illumination Microscopy by Thick Slice Blind-SIM Reconstruction," PLoS ONE 10, e0132174 (2015).
[13] R. Ayuk, H. Giovannini, A. Jost, E. Mudry, J. Girard, T. Mangeat, N. Sandeau, R. Heintzmann, K. Wicker, and K. Belkebir, "Structured illumination fluorescence microscopy with distorted excitations using a filtered blind-SIM algorithm," Optics letters 38, 4723-4726 (2013).
[14] P. Thibault and A. Menzel, "Reconstructing state mixtures from diffraction measurements," Nature 494, 68-71 (2013).
[15] D. J. Batey, D. Claus, and J. M. Rodenburg, "Information multiplexing in ptychography," Ultramicroscopy 138, 13-21 (2014).
[16] S. Dong, R. Shiradkar, P. Nanda, and G. Zheng, "Spectral multiplexing and coherent-state decomposition in Fourier ptychographic imaging," Biomedical Optics Express 5, 1757-1767 (2014).
[17] A. M. Maiden, M. J. Humphry, and J. M. Rodenburg, "Ptychographic transmission microscopy in three dimensions using a multi-slice approach," Journal of the Optical Society of America A 29, 1606-1614 (2012).

Chapter 7 Multilayer fluorescence imaging on a single-pixel detector

7.1 Background

A critical challenge for fluorescence imaging is the loss of high frequency components in the detection path. Such a loss can be related to the limited numerical aperture of the detection optics, aberrations of the lens, and tissue turbidity. Here, we report an imaging scheme that integrates three innovations to tackle this challenge: 1) multilayer sample modeling [1, 2], 2) ptychography-inspired recovery procedures [3-6], and 3) lensless single-pixel detection [7]. In the reported scheme, we directly placed a 3D sample on top of a lensless single-pixel detector; no lens is used at the detection path.

We then used a known mask to generate speckle patterns in 3D and scanned this known mask to different positions for sample illumination. The sample was then modeled as multiple layers and the captured 1D fluorescence signal was used to recover multiple sample images along the z axis. Different from the previous lensless fluorescence imaging demonstrations [8, 9], the achievable resolution of the reported scheme is determined by the speckle size of the illumination patterns, where we encode the 3D sample information into 1D fluorescence measurements. We note that, the general idea of encoding sample information using non-uniform illumination patterns is not new [10-16]. It has been demonstrated, among others, in structured illumination microscopy for improving the resolution beyond the diffraction limit [16]. In the reported approach, however, we combine the pattern-illumination strategy with single-pixel detection scheme for multiplexed lensless fluorescence imaging. In particular, we propose a multilayer single-pixel imaging framework for recovering 3D sample information from 1D fluorescence signals. Different from

compressive sensing scheme [7], the proposed recovery framework is inspired and modified from the multiplexed ptychographic algorithms [2-5], where we switch between the spatial and Fourier domains in an iterative manner. In the spatial domain, we update the multilayer sample estimate using the illumination patterns from the known mask. In the Fourier domain, we update the central pixel of the Fourier spectrum using the measured single-pixel fluorescence signals. The proposed single-pixel updating process in the Fourier domain, to the best of our knowledge, is novel and compatible with existing ptychographic and phase retrieval algorithms.

7.2 Multilayer single-pixel imaging scheme and simulation results

In the reported scheme, we directly place a 3D sample on top of a single-pixel detector. The forward imaging model can be described as follows:

$$I_n = \sum_{x,y,m} Object_{layer\_m}(\mathrm{x},\mathrm{y}) \cdot P_{mn}(\mathrm{x},\mathrm{y}) \tag{7.1}$$

where $Object_{layer\_m}$(x, y) represents the mth-layer object image in the x-y domain, P_{mn}(x, y) represents the nth illumination pattern for object layer m, and I_n represents the 1D measurement from the single-pixel detection (a photodiode). The summation in Eq. (7.1) represents the signal summation over the x-y-z domain (summation over 'm' is the same as the summation of multilayer images at the z direction). Therefore, the detected 1D signal in our scheme represents a mixture of the object at different layers. The goal of the recovery process is to recover the multilayer object images $Object_{layer\_m}$(x, y) from single-pixel measurements I_n. The recovery process starts with initial guesses of the object images at different layers $Object_{layer\_m}$(x, y). Second, we define I_{pm} and I_{tm}: $I_{pm}(\mathrm{x},\mathrm{y}) = Object_{layer\_m}(\mathrm{x},\mathrm{y}) \cdot P_{mn}(\mathrm{x},\mathrm{y})$, $I_{tm} = \sum_{x,y} I_{pm}(\mathrm{x},\mathrm{y})$. We note that, I_{pm}(x,y) is a function of x and y while I_{tm} presents the total signal energy of illumination pattern encoded layer m of the object.

Third, we update I_{tm} using the measurement I_n: $I_{tm}^{update} = I_{tm}(I_n / \sum_m I_{tm})$. Fourth, we update the I_{pm}(x,y) in the Fourier domain using the following equation:

$$\mathrm{F}\left(I_{pm}^{updated}(\mathrm{x},\mathrm{y})\right) = \mathrm{F}\left(I_{pm}(\mathrm{x},\mathrm{y})\right)\cdot(1-\delta(\mathrm{x},\mathrm{y})) + I_{tm}^{updated}\cdot\delta(\mathrm{x},\mathrm{y}) \tag{7.2}$$

where $\delta(\mathrm{x},\mathrm{y})$ denotes the 2D discrete delta function. The key idea of Eq. (7.2) is to use the total signal energy at layer m to update the central pixel of the Fourier spectrum of I_{pm}(x,y). This updating step, to the best of our knowledge, is novel and compatible with existing ptychographic algorithms. Finally, we update the m^{th} layer object image in the spatial domain, similar to the previous pattern-illuminated algorithm [5]:

$$Object_{layer\_m}^{updated}(\mathrm{x},\mathrm{y}) = Object_{layer\_m}(\mathrm{x},\mathrm{y}) + \frac{P_{mn}(\mathrm{x},\mathrm{y})}{(\max(P_{mn}(\mathrm{x},\mathrm{y})))^2}(I_{pm}^{updated}(\mathrm{x},\mathrm{y}) - I_{pm}(\mathrm{x},\mathrm{y})) \tag{7.3}$$

The updating process will be repeated for all n single-pixel measurements and the entire process is terminated until convergence, which can be measured by the difference between two successive recoveries. In a practical implementation, we can simply terminate it with a predefined loop number, typically 150-200.

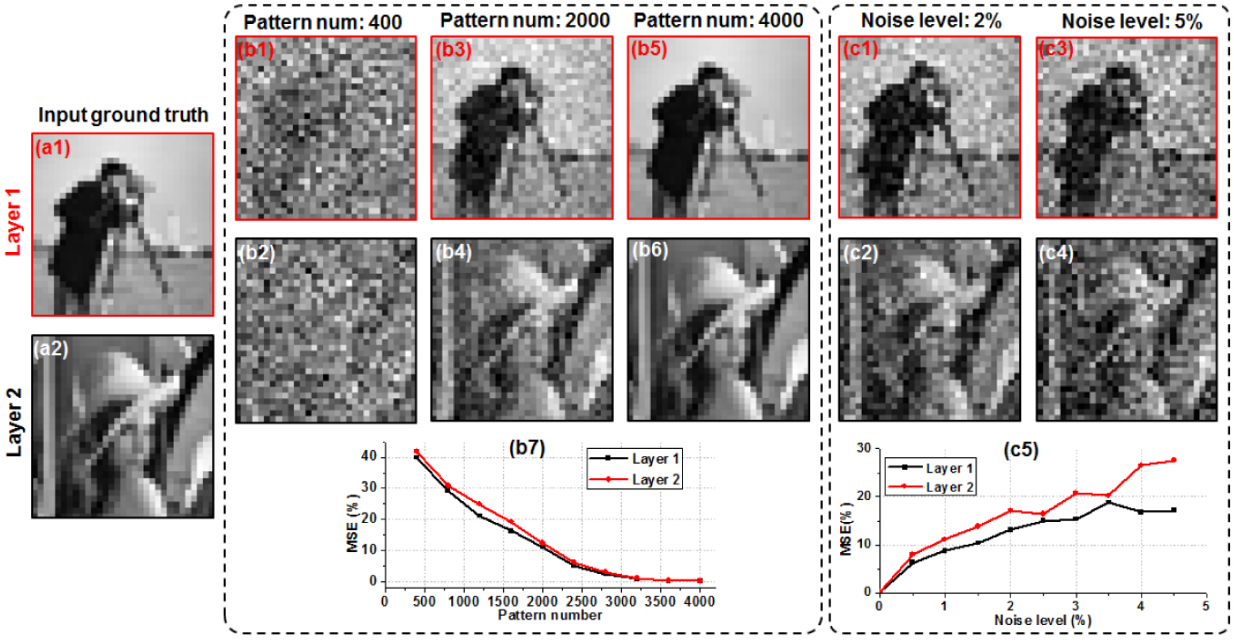

Figure 7-1: Simulation of the multilayer single-pixel imaging scheme. (a) The input two-layer object. (b) The recovered results using different number of illumination patterns. (c) The recovered results with different levels of additive noises. MSE is used as a metric to quantify the results in (b7) and (c5).

We will first validate the reported approach using simulations. In Fig. 7-1, we simulated a two-layer object (Fig. 7-1(a), 31 by 31 pixels) separated by 10 microns and illuminated by non-uniform patterns from a random mask (the illumination angle is 45 degrees). We then scanned the mask to different positions and simulated the 1D captured signals using Eq. (7.1). Based on the single-pixel recovery process discussed above, we can then recover the object images at different layers using the 1D signals. In Fig. 7-1(b), we show the recovery of the two layers using different number of illumination patterns. Figure 7-1(b7) quantifies the result using the mean square error (MSE). We can see that, the image quality increases when we use more patterns and saturates at ~3000 patterns. The total number of independent pixels for this two-layer object is 1922, and thus, the oversampling factor is 3000/1922 = 1.56. Such a data redundancy may be necessary when we separate different object states from the 1D mixtures. Further investigation along this line is highly desired. In Fig. 7-1(c), we show the recovered images with different noise levels. Figure 7-1(c5) quantifies the noise performance using MSE, and as expected, the imaging performance gradually degrades as the noise increases.

In Fig. 7-2, we investigated the relationship between the number of layers in our model and the number of illumination patterns we need for the reconstruction. Figure 7-2(a) shows the imaging performances with respect to different numbers of illumination patterns and object layers. We need more illumination patterns when the number of object layers increases. Based on the MSE metric in Fig. 7-2(a), their relationship is linear. In other words, if we double the object layers in our model, we also need to double the number of illumination patterns for a successful

reconstruction. In Fig. 7-2(b), we used a 3D confocal neural cell data as the ground truth and simulated the single-pixel measurements using Eq. (7.1). We then modeled the cell with 10 layers and recover the images using the single-pixel meansurements.

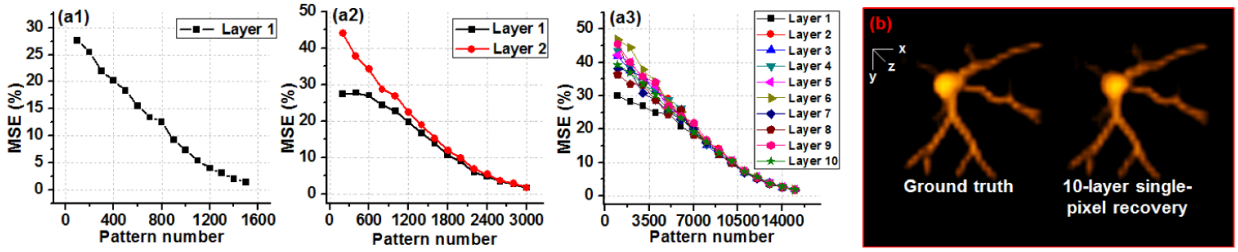

Figure 7-2: Imaging performance of the multilayer imaging scheme with respect to different numbers of object layers and illumination patterns. MSE is used to quantify the imaging performance with 1 layer (a1), 2 layers (a2), 10 layers (a3). (b) 10-layer single-pixel recovery of a 3D neural cell.

We investigated the achievable resolution of the reported scheme in Fig. 7-3, where we used patterns with different speckle feature sizes (i.e., different illumination NAs) for sample illumination. Figure 7-3(a) shows the input resolution target. Figure 7-3(b) and 7-3(c) show illumination patterns with two different speckle sizes and their corresponding recoveries. We can see that, the achievable resolution of our imaging scheme is determined by the spatial-frequency support of the illumination pattern. In Fig. 7-3(d), we further quantify the imaging performance for the cases of two different speckle sizes. As expected, a higher resolution of the recovered image requires a larger number of illumination patterns.

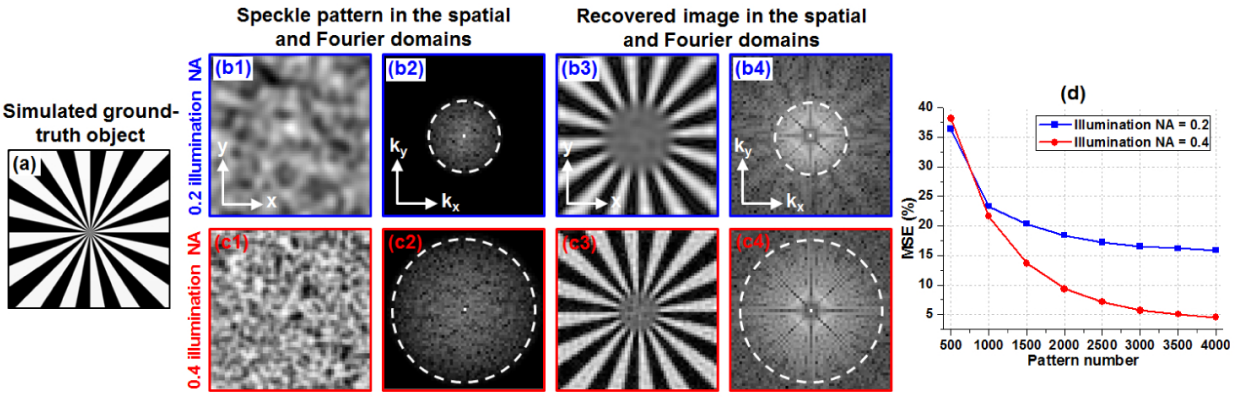

Figure 7-3: Achievable resolution of the reported imaging scheme. (a) The input resolution target. (b) and (c): speckles with two different feature sizes and their corresponding recoveries. (d) MSE is used to quantify the imaging performance for the cases of two different speckle sizes.

7.3 Experimental validation

We have performed three experiments to validate the reported imaging scheme. In the first experiment, we used a microscope setup with a 1X objective lens and a single pixel detector (Si photodiode; active area: 10 mm by 10 mm) for image acquisition, as shown in Fig. 7-4(a). In this experiment, we prepared two-layer fluorescence samples using orange fluorescence microspheres (size range: 1 - 5 μm; peak emission wavelength: 606 nm) deposited on two glass slides. The separation of these two layers is ~2 mm. We used a 40-mW 532 nm laser diode and a known chromium mask for generating sample illumination. The incident angle is ~45 degrees in this experiment and the feature size of the chromium mask is ~0.3 mm. We placed a fluorescence bandpass filter at the detection path (centered at 635 nm with 60-nm bandwidth). We scanned the mask to 1000 different spatial positions and captured the corresponding fluorescence signals using the single-pixel detector. The 1D signals were then used to recover the two-layer objects as shown in Fig. 7-4(b1)-(b2) and 7-4(c1)-(c2). As a comparison, we also replaced the single-pixel detector with a CCD and the captured images are shown in Fig. 7-4(b3) and 7-4(c3). We note that, the

experiment in Fig. 7-4 directly points to a development for scanning confocal microscope, where single-pixel detector is used for image acquisition. We can, for example, model the single-pixel data as a mixture of multiple layers (no pinhole is needed in this case) and recover the 3D images with one x-y scan.

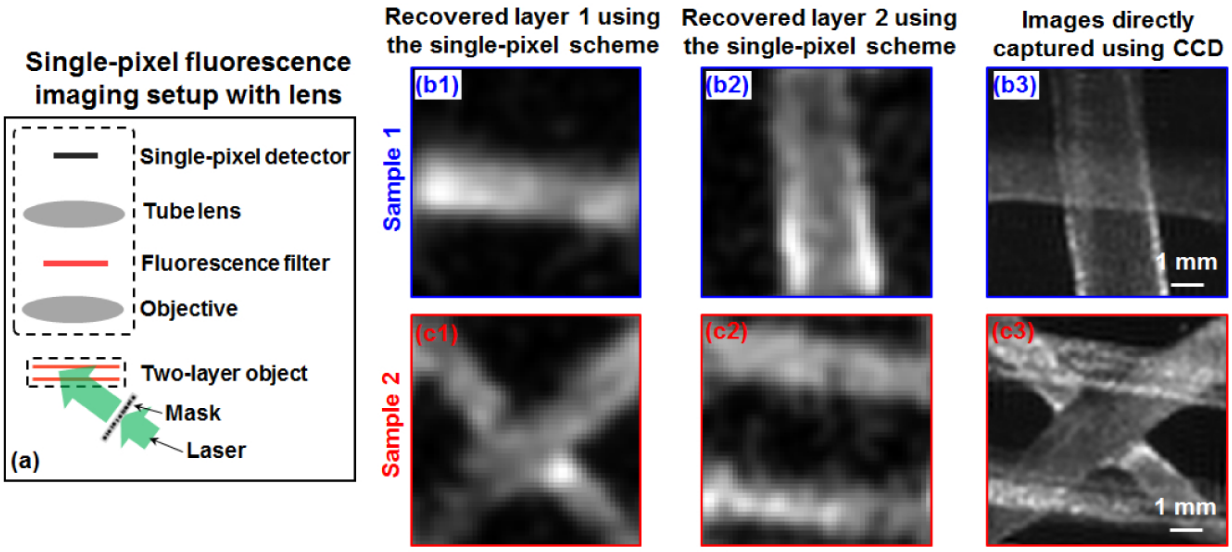

Figure 7-4: Multilayer single-pixel imaging scheme using a lens setup. (a) The experimental setup. The fluorescence imaging results of sample 1 (b) and 2 (c).

In the second experiment, we validate the reported imaging scheme using a lensless setup, as shown in Fig. 7-5(a). In this experiment, we prepared a 4-layer fluorescence objects using the same fluorescence microspheres. The separation of different layers is ~2 mm and we directly place this 4-layer object on top of the single-pixel detector. The incident angle of the speckle patterns is ~70 degrees. The distance between the first layer and the active sensing surface of the detector is ~5 mm and a fluorescent filter is placed in between. Figure 7-5(b) shows the recovered images of the 4 layers and the ground-truth images are shown in Fig. 7-5(c). Figure 7-5(d) shows the 3D visualization of our recovery and the ground truth.

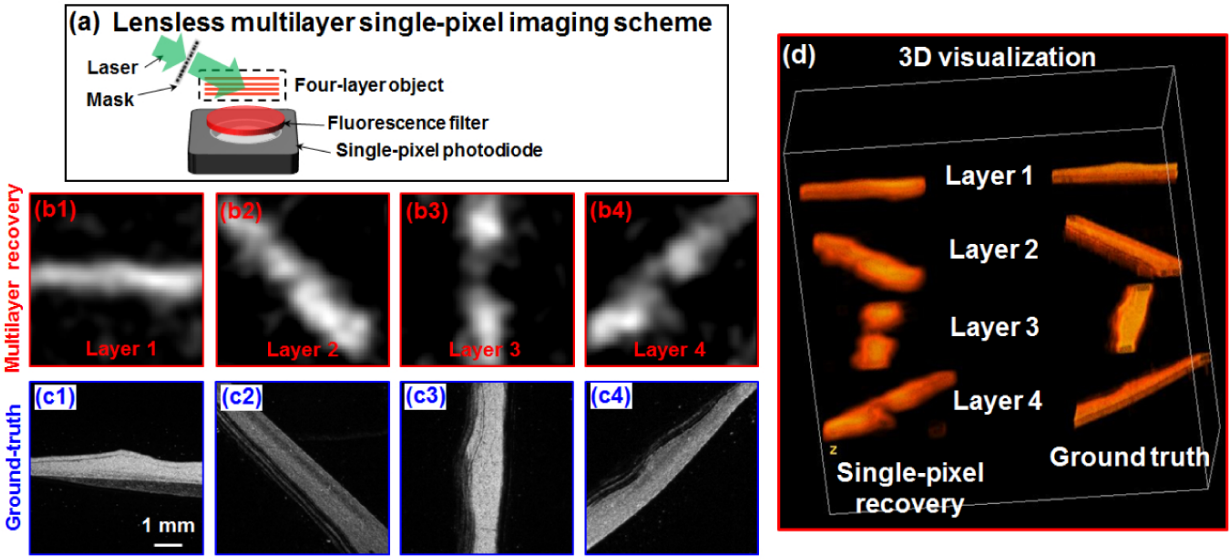

Figure 7-5: Multilayer single-pixel imaging scheme using a lensless setup. (a) The experimental setup. We scanned the mask to 2000 different spatial positons and captured corresponding 1D fluorescence signal for recovery. The recovered images (b) and ground truth (c) of the 4 sample layers. (d) 3D visualization of the recovered images and the ground truth.

The reported scheme is not limited to the recovery of multiple layers of fluorescence samples; it can also be used to recover sample images at multiple wavelengths. Fig. 7-6 shows the results of recovering R/G/B channels of a color object. The experimental setup is similar to that of Fig. 7-4. In this experiment, we used a projector to generate known 1500 color speckle patterns for sample illumination, as shown in Fig. 7-6(a). The monochromatic 1D signals from the single-pixel detector were then used to recover the R/G/B channels in Fig. 7-6(b) and the ground truth images are shown in Fig. 7-6(c).

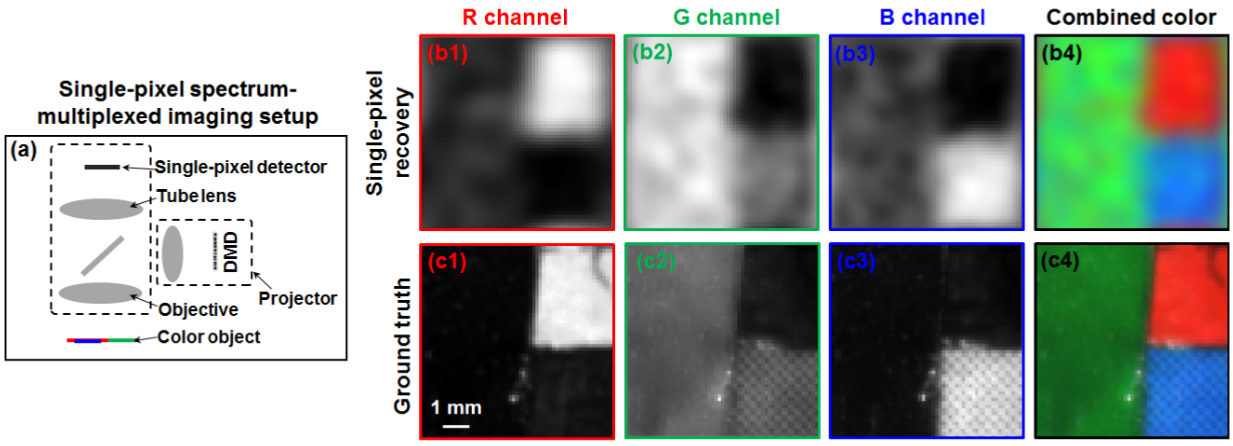

Figure 7-6: Spectrum-multiplexed single-pixel imaging scheme using a lens setup. (a) The experimental setup. (b) The recovered images of different color channels using the reported scheme. (c) The ground-truth images of the color object.

7.4 Discussion

We have proposed and validated a single-pixel detection scheme for multilayer fluorescence imaging. The reported scheme integrates multilayer sample modeling, ptychography-inspired recovery procedures, and lensless single-pixel detection to tackle the challenge of fluorescence imaging from a new perspective. There are several important implications of the reported scheme. 1) In a conventional laser scanning confocal microscope, we use a single pixel detector (photomultiplier tube) with a confocal pinhole for image acquisition. The confocal pinhole is for rejecting fluorescence signals that are not from the focal position. We can use the reported single-pixel recovery scheme for scanning confocal microscope. In this case, we can remove the confocal pinhole and model the captured single-pixel fluorescence signal as a mixture of signals from different sample layers. Based on a single x-y scan, we may be able to recover multiple layers of the sample. Effort along this direction is ongoing. 2) The reported scheme can be used for lensless single-pixel 3D fluorescence imaging. By using a high-speed photomultiplier tube, we can, for example, detect the fluorescence lifetime signal of the sample. 3) One challenge for deep tissue

fluorescence imaging is tissue turbidity. We may be able to combine the reported scheme with memory effect of the tissue to tackle this challenge. In this case, one can scan speckle patterns by slightly changing the incident angles using high-speed Glavo mirrors. The fluorescence signals from the single-pixel detector can then be used to jointly recover the multilayer fluorescence samples and the speckle patterns [5, 17].

Bibliography

[1] A. M. Maiden, M. J. Humphry, and J. M. Rodenburg, "Ptychographic transmission microscopy in three dimensions using a multi-slice approach," Journal of the Optical Society of America A 29, 1606-1614 (2012).
[2] S. Dong, K. Guo, S. Jiang, and G. Zheng, "Recovering higher dimensional image data using multiplexed structured illumination," Optics express 23, 30393-30398 (2015).
[3] P. Thibault and A. Menzel, "Reconstructing state mixtures from diffraction measurements," Nature 494, 68-71 (2013).
[4] D. J. Batey, D. Claus, and J. M. Rodenburg, "Information multiplexing in ptychography," Ultramicroscopy 138, 13-21 (2014).
[5] S. Dong, P. Nanda, R. Shiradkar, K. Guo, and G. Zheng, "High-resolution fluorescence imaging via pattern-illuminated Fourier ptychography," Optics Express 22, 20856-20870 (2014).
[6] S. Dong, R. Shiradkar, P. Nanda, and G. Zheng, "Spectral multiplexing and coherent-state decomposition in Fourier ptychographic imaging," Biomedical Optics Express 5, 1757-1767 (2014).
[7] M. F. Duarte, M. A. Davenport, D. Takhar, J. N. Laska, T. Sun, K. E. Kelly, and R. G. Baraniuk, "Single-pixel imaging via compressive sampling," IEEE Signal Processing Magazine 25, 83 (2008).
[8] A. F. Coskun, I. Sencan, T.-W. Su, and A. Ozcan, "Lensless wide-field fluorescent imaging on a chip using compressive decoding of sparse objects," Optics Express 18, 10510-10523 (2010).
[9] A. F. Coskun, T.-W. Su, and A. Ozcan, "Wide field-of-view lens-free fluorescent imaging on a chip," Lab on a Chip 10, 824-827 (2010).
[10] S. Pang, C. Han, J. Erath, A. Rodriguez, and C. Yang, "Wide field-of-view Talbot grid-based microscopy for multicolor fluorescence imaging," Optics express 21, 14555-14565 (2013).
[11] S. A. Arpali, C. Arpali, A. F. Coskun, H.-H. Chiang, and A. Ozcan, "High-throughput screening of large volumes of whole blood using structured illumination and fluorescent on-chip imaging," Lab on a Chip 12, 4968-4971 (2012).
[12] I. J. Cox, C. J. Sheppard, and T. Wilson, "Super-resolution by confocal fluorescent microscopy," Optik 60, 391-396 (1982).
[13] C. B. Müller and J. Enderlein, "Image Scanning Microscopy," Physical Review Letters 104, 198101 (2010).
[14] E. Mudry, K. Belkebir, J. Girard, J. Savatier, E. Le Moal, C. Nicoletti, M. Allain, and A. Sentenac, "Structured illumination microscopy using unknown speckle patterns," Nature Photonics 6, 312-315 (2012).

[15] J. Min, J. Jang, D. Keum, S.-W. Ryu, C. Choi, K.-H. Jeong, and J. C. Ye, "Fluorescent microscopy beyond diffraction limits using speckle illumination and joint support recovery," Scientific reports 3(2013).
[16] M. G. Gustafsson, "Surpassing the lateral resolution limit by a factor of two using structured illumination microscopy," Journal of microscopy 198, 82-87 (2000).
[17] N. Chakrova, R. Heintzmann, B. Rieger, and S. Stallinga, "Studying different illumination patterns for resolution improvement in fluorescence microscopy," Optics express 23, 31367-31383 (2015).

Chapter 8 Multimodal imaging with a liquid crystal display

Illumination engineering is critical for getting high-resolution, high-quality images in microscope settings. In a typical microscope platform, the condenser lens provides sample illumination that is uniform and free from glare. The associated condenser diaphragm can be used to adjust the illumination numerical aperture. In this chapter, we report a programmable condenser lens for active illumination control. In our prototype setup, we used a $15 liquid crystal display as a transparent spatial light modulator and placed it at the back-focal-plane of the condenser lens. By setting different binary patterns on the display, we can actively control the illumination and the spatial coherence of the microscope platform. We demonstrated the use of such a simple scheme for multimodal imaging, including bright-field microscopy, dark-field microscopy, phase-contrast microscopy, 3D tomographic imaging, and super-resolution Fourier ptychographic imaging. The reported illumination engineering scheme is cost-effective and compatible with most existing platforms. It enables a turnkey solution with high flexibility for researchers in various communities. From the engineering point-of-view, the reported illumination scheme may also provide new insights for the development of multimodal microscopy and Fourier ptychographic imaging.

8.1 Background

The condenser lens system is a ubiquitous component of conventional microscope platforms for uniform sample illumination. It typically consists of a high numerical aperture (NA) condenser lens and a condenser diaphragm placed at the back-focal plane of the lens [1]. This condense diaphragm allows for adjustment of the optimal illumination aperture, which defers with different microscopy techniques. In bright-field microscopy, the illumination NA needs to be matched to

the collection NA by adjusting the size of the condenser diaphragm. In dark-field microscopy, an aperture stop is placed at the condenser diaphragm to ensure the illumination NA is larger than the collection NA. In phase-contrast microscopy, a ring aperture is placed at the condenser diaphragm to match to the ring-shape phase plate of the objective lens. In short, each microscopy technique requires vastly different condenser illumination. Currently, these requirements are met by physical adjustment of condenser diaphragms and, in some cases, a need for specialized condenser apertures. However, with the maturity of liquid crystal display in consumer electronics, there exists an opportunity for cost-effective, active digital control of the illumination system.

We report the use of a $15 liquid crystal display to achieve programmable condenser illumination control. In our prototype setup, we placed the display at the back-focal-plane of the condenser lens. By setting different binary patterns on the display, we can actively control the illumination and the spatial coherence of the microscope platform. To demonstrate the versatility of the reported scheme, we use the prototype platform for multimodal microscopy imaging, including bright-field microscopy, darkfield microscopy, phase-contrast microscopy [2, 3], 3D tomographic imaging [4], and super-resolution Fourier ptychographic imaging [5]. Essentially, the liquid crystal display severs as a transparent spatial light modulator (SLM) in the reported scheme. The use of SLM in microscopy has drawn many attentions in recent years [6]. However, the focus of these techniques is to place the SLM at the detection path to modulate the pupil function or to project intensity patterns onto the sample. To the best of our knowledge, the modulation of the condenser illumination has not been reported before. We also note that, the active illumination control for microscopy setting is not a new concept. For example, an LED array can be used for active sample illumination [4, 5, 7-10]. The reported scheme here, however, has some important advantages over the previous demonstrations: 1) it is cost-effective and is compatible with most existing compound microscopes. The only modification required is the addition of a low-cost liquid crystal display

at the condenser diaphragm. 2) The liquid crystal display provides a large degree of freedom for illumination engineering. As a reference, a typical liquid crystal display used for consumer electronic provides more than 400 pixels per inch, which is the equivalent of 800 by 800 pixels over a condenser diaphragm of ~ 2 inches. This provides orders of magnitudes improvement in degrees of freedom, over the previously demonstrated LED array approach, for the purpose for the spatial and coherence control of microscope illumination. 3) The illumination intensity of the reported scheme is determined by the light source of the microscope platform. We can use one or multiple high-power light sources to increase the photon budget. For the LED array approach, it is difficult to increase the illumination power since it scales with the size of LED elements. 4) In the reported scheme, the illumination from the condenser lens is a plane wave modulated by the active liquid-crystal-display aperture. In contrast, the previously demonstrated LED approach essentially provides an array of spherical wave illumination, necessitating a plane wave approximation of splitting the entire image into small tiles [5]. 5) Finally, in the reported scheme, the intensity of the light source does not fluctuate as we set different patterns on the display. For the LED array approach, one needs to calibrate for the intensity differences between LED elements and the intensity fluctuations over time. In addition, engineering the condenser aperture using a display is more efficient when illuminating the sample with a large incident angle. For the LED array approach, no lens is placed between the LED array and the sample, and as such, less than 8% of the LED emission from the edge of the array can be delivered to the sample.

In summary, the reported illumination engineering scheme provides a turnkey solution with high flexibility for researchers in various communities. From the engineering point-of-view, it may also provide new directions for the development of multimodal microscopy including the recently developed Fourier ptychographic imaging approach. This chapter is structured as follows: in section 8.2, we will present the

prototype setup of the reported illumination scheme. In section 8.3, we will demonstrate the use the reported scheme for multimodal microscopy. Finally, we will summarize the results and discuss future directions.

8.2 Microscope illumination with LCD

The reported illumination engineering scheme is shown in Fig. 8-1(a), where a low-cost liquid crystal display is used as a transparent SLM and placed at the back-focal plane of the condenser lens. By showing different binary patterns on the display, we can achieve different microscopy imaging modalities, as shown in Fig. 8-1(b).

For bright field microscopy, we can display a circular pattern as shown in Fig. 8-1(b), where the pixel transmission is turned off outside the circle. The diameter of the pattern can be adjusted to match to different NAs of the objective lenses. Such an adjustment process is similar to adjusting the size of condenser diaphragm in conventional microscope platforms. However, in the reported scheme, this process is performed without any mechanical switching. Similar to the bright-field microscopy, we can also display a complementary pattern for darkfield microscopy. In this case, the pixel transmission was turned off within the circle. As such, no direct transmission light is able enter the objective lens. This darkfield imaging process is similar to adding a darkfield aperture stop at the condenser diaphragm. Again, in the reported scheme, no mechanical switching is needed.

A more interesting microscopy modality is the phase contrast (or phase gradient) imaging. In the reported scheme, we can display two complementary semicircular patterns at the liquid crystal display (Fig. 8-1(b)) and capture two images I_1 and I_2 using conventional objective lenses. The phase contrast image of the sample can then be recovered by $2(I_1-I_2)/(I_1+I_2)$ [3, 7]. Essentially, this phase-contrast imaging modality is similar to the scanning differential phase contrast system [11] where a split-detector or a quadrant diode is placed in the Fourier plane of the collector and the image is formed by subtracting intensities recorded by two halves of the detector. The phase-contrast imaging scheme shown in Fig. 8-1(b) is a reciprocal

system by placing the semicircular aperture stop in the condenser diaphragm instead of the Fourier plane. We also note that, in conventional phase contrast microscopy, one needs to place a ring-aperture at the condenser diaphragm to match the phase plate ring in the phase contrast objective lens. In the reported scheme, we can simply show a ring pattern on the liquid crystal display where the pixel transmission is turned off outside the ring pattern.

The reported scheme can also be used to perform 3D tomographic imaging. We have previously demonstrated such an 3D tomographic imaging modality using an LED array [4]. In the reported scheme, we can simply show a scanning aperture pattern on the liquid crystal display (Fig. 8-1(b)). For each position of the aperture, the illumination is a plane wave with an oblique incident angle. Therefore, by showing a scanning aperture on the display, we effectively illuminate the sample with different incident angles. Based on all captured images, we can perform 3D tomographic reconstruction to recover images at different sections. We note that, this imaging modality requires the direct transmission light (zero order light) enters the collection optics. Thus, the scanning aperture is restricted within the NA of the collection optics, i.e., the yellow circle in Fig. 8-1(b).

Lastly, we can also use the reported scheme for super-resolution Fourier ptychographic imaging, a recently developed computational imaging approach [5]. In brief, FP illuminates the sample with different oblique incident angles and captures the corresponding intensity images using a low-NA objective lens. The captured images are then synthesized in the Fourier domain to recover a high-pixel-count sample image that surpasses the diffraction limit of the employed optics [5, 12-18]. The recovery process of FP switches between the spatial and the Fourier domain. In the spatial domain, the captured images are used as the intensity constraint for the solution. In the Fourier domain, the confined pupil function of the objective lens is used as the support constraint for the solution. This pupil function constraint is digitally panned across the Fourier space to reflect the angular variation of its illumination. In the reported scheme, we can simply

show a scanning aperture across the liquid crystal display (Fig. 8-1(b)). Different from the 3D imaging case, the illumination NA needs to be larger than the collection NA for super resolution imaging. Therefore, the scanning aperture will not be restricted by the NA of the objective lens, as shown in Fig. 8-1(b).

The experimental setup of reported scheme is shown in Fig. 8-1(c). In this platform, we used a conventional microscope platform (Olympus CX41) with a low-cost liquid crystal display (1.8 inch, 160 by 128 pixels, Amazon, $15). We removed the back light of the display and used it as a transparent SLM. To build the prototype platform, we only need to place the display at the back focal plane of the condenser lens, as shown in Fig. 8-1(c). No other modification is needed. Therefore, the reported platform provides a turnkey solution for researchers in different communities.

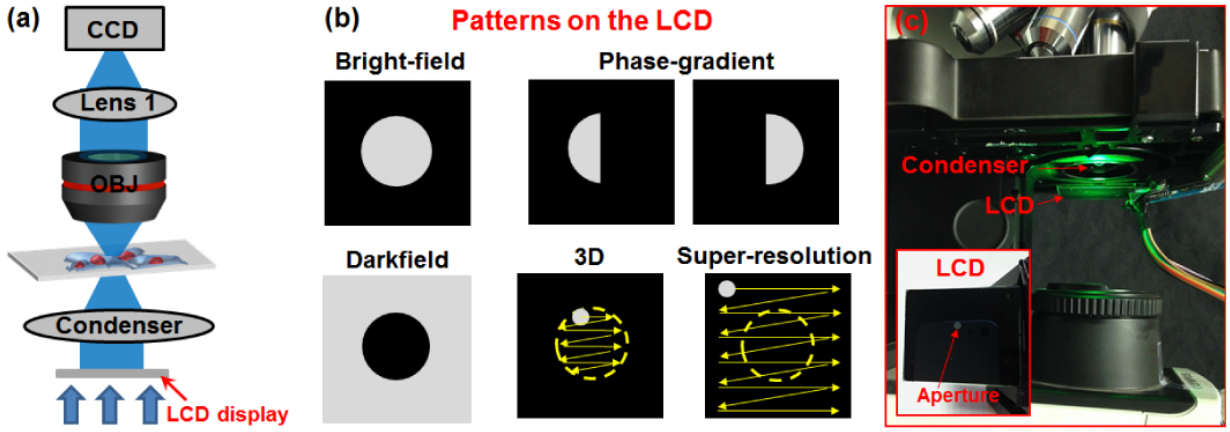

Figure 8-1: (a) The reported scheme using a low-cost liquid crystal display at the condenser diaphragm. (b) Different patterns can be displayed for achieving different microscopy modalities. (c) The experimental setup with a green LED as the light source. A $15 liquid crystal display (with back light removed) is placed at back-focal plane of the condenser lens. Media 1 shows the different patterns on the display.

8.3 Multimodal imaging demonstration

We have tested the reported scheme for multimodal microscopy imaging. Figure 8-2(a) and (b) show the bright-field and dark-field images of a starfish embryo sample. We note that, for the dark-field image in Fig. 8-2(b), we capture a reference image by setting the display to the 'off state' and subtract this reference image to enhance the contrast. Figure 8-2(a1)-(a3) shows bright-field images with different illumination NAs, corresponding to different degrees of the spatial coherence. Fig. 8-2(c)-(d) show the phase gradient (contrast) images along different directions for the same sample. For each of these phase contrast images, we captured two raw images corresponding to the two complementary half-circular patterns at the display, and processed them as discussed in the previous section. We used a 10X, 0.25 NA lens in this experiment.

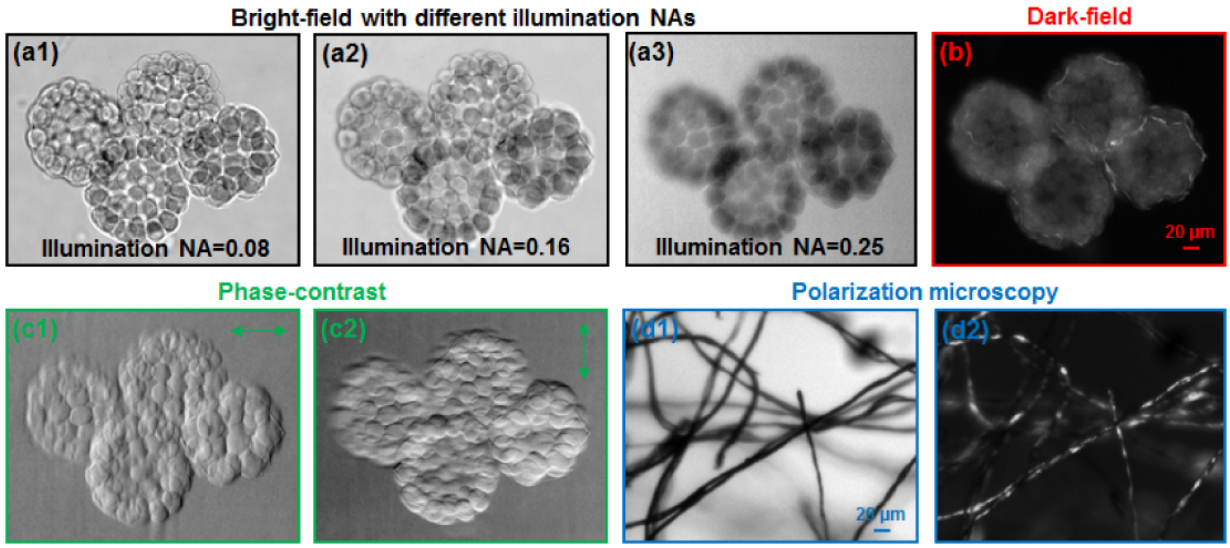

Figure 8-2: (a) Bright-field, (b) Dark-field, (c) Phase-contrast imaging using reported scheme. (c1) and (c2) shows the phase gradient images along two different directions.

Figure 8-3 shows the 3D tomographic imaging capability of the reported platform. In this experiment, we captured 49 images by showing a scanning aperture pattern on the display. We used a 10X, 0.25 objective lens in this demonstration. We then used the captured images to recover images at different

sections. The reconstruction process is the same as tomographic reconstruction reported before [4]. From Fig. 8-3, we can see that different parts of the starfish embryo sample are in-focus at different recovered sections.

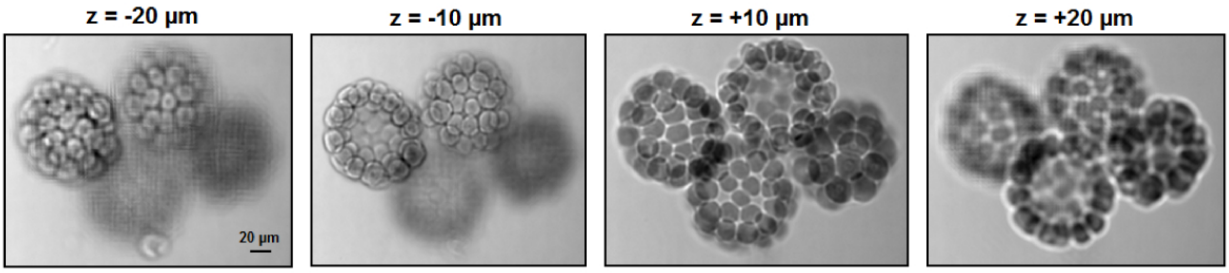

Figure 8-3: 3D tomographic reconstruction using the reported scheme. We captured 49 images by setting a scanning aperture at the transparent liquid crystal display. These images are used to recover sample images at different sections.

Lastly, we also tested the reported platform for super-resolution Fourier ptychographic microscopy. The image acquisition process is similar to that of the 3D tomographic imaging case. However, in this case, the illumination NA needs to be larger than the collection NA to achieve the super-resolution imaging capability. In our implementation, we captured 121 raw images corresponding to a scanning aperture pattern at different positions on the display. We used a 4X, 0.1 NA objective in the acquisition process and the captured images were then synthesized in the Fourier domain to increase the synthetic NA to ~0.5. Figure 8-4(a1) shows the raw image of an USAF resolution target and Fig. 8-4(a2) shows the recovered image with a synthetic NA of 0.5. We also tested the reported platform for biological samples. Figure 8-4(b1) and 8-4(c1) show the raw images of a pathology slide and a mouse brain section. The corresponding super-resolution recoveries are shown in Fig. 8-4(b2) and 8-4(c2). This super-resolution imaging experiment demonstrated the high flexibility of the reported illumination engineering scheme.

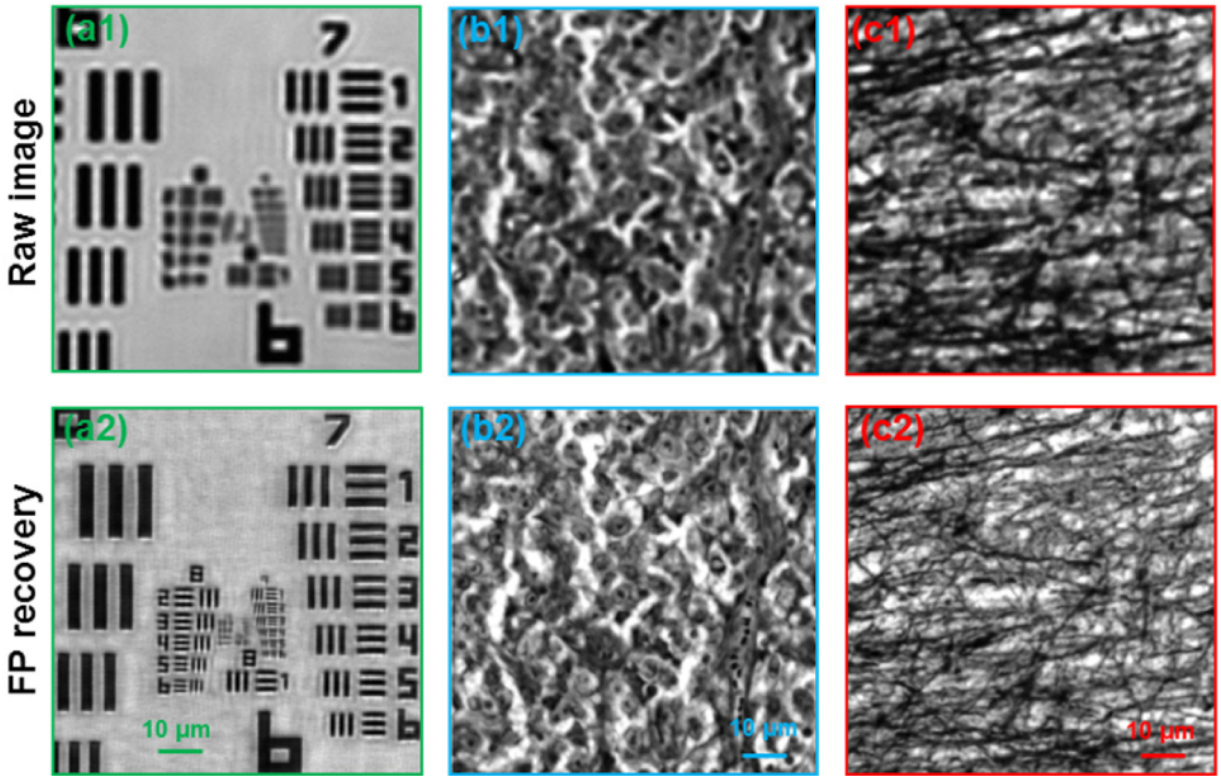

Figure 8-4: Super-resolution imaging using the reported scheme. We captured 121 images by setting a scanning aperture at the transparent liquid crystal display. These images are used to recover super-resolution images using the Fourier ptychographic algorithm. (a1)-(c1) Raw images for a USAF resolution target, a pathology slide, and a mouse brain section. (a2)-(c2) Recovered super-resolution images of the samples.

8.4 Discussion

We have demonstrated a simple and effective approach for microscopy illumination engineering. The reported approach is cost-effective and compatible with most existing platforms. At the application front, we have demonstrated it for multimodal imaging capabilities, including bright-field microscopy, darkfield microscopy, phase-contrast microscopy, 3D tomographic imaging, and super-resolution Fourier ptychographic imaging. The reported scheme may find applications in phase tomography, where angle-varied plane waves are used for sample illumination [19]. It can

also be used in field-portable Fourier ptychographic microscope for active illumination control [13]. The liquid crystal display can also be placed at the Fourier plane of a 4f system to perform aperture-scanning Fourier ptychographic imaging for 3D holography and aberration correction [14, 20].

One limitation of the current prototype platform is the low extinction ratio of the liquid crystal display. This ratio is about 300 in our prototype setup, and thus, the 'on-state' transmission is only 300 times higher than that of the 'off-state'. This relative low extinction ratio leads to a residue background of the captured image, especially for images with large incident angles. Although we can subtract this background from the measurements, the noise would remain in the images. One of the future directions is to increase the extinction ratio by putting two displays together. In that case, the extinction ratio would be ~100,000 instead of 300. We also note that, the illumination is polarized in the reported platform. If we placed another polarizer with a different orientation in the detection path, we can add another imaging modality, polarization microscopy, to the reported platform. Finally, we can also use multiplexing scheme to improve the light delivering efficiency. For example, we can scan multiple apertures and/or turn on multiple wavelengths at the same time to increase the photon budget [15, 16].

Bibliography

[1] D. A. Boas, C. Pitris, and N. Ramanujam, Handbook of biomedical optics (CRC press, 2012).
[2] R. Yi, K. K. Chu, and J. Mertz, "Graded-field microscopy with white light," Optics Express 14, 5191-5200 (2006).
[3] S. B. Mehta and C. J. R. Sheppard, "Quantitative phase-gradient imaging at high resolution with asymmetric illumination-based differential phase contrast," Optics Letters 34, 1924-1926 (2009).
[4] G. Zheng, C. Kolner, and C. Yang, "Microscopy refocusing and dark-field imaging by using a simple LED array," Optics Letters 36, 3987-3989 (2011).
[5] G. Zheng, R. Horstmeyer, and C. Yang, "Wide-field, high-resolution Fourier ptychographic microscopy," Nature Photonics 7, 739-745 (2013).
[6] C. Maurer, A. Jesacher, S. Bernet, and M. Ritsch-Marte, "What spatial light modulators can do for optical microscopy," Laser & Photonics Reviews 5, 81-101 (2011).

[7] L. Tian, J. Wang, and L. Waller, "3D differential phase-contrast microscopy with computational illumination using an LED array," Optics Letters 39, 1326-1329 (2014).
[8] G. Zheng, S. A. Lee, Y. Antebi, M. B. Elowitz, and C. Yang, "The ePetri dish, an on-chip cell imaging platform based on subpixel perspective sweeping microscopy (SPSM)," Proceedings of the National Academy of Sciences 108, 16889-16894 (2011).
[9] Z. Liu, L. Tian, S. Liu, and L. Waller, "Real-time brightfield, darkfield, and phase contrast imaging in a light-emitting diode array microscope," Journal of biomedical optics 19, 106002-106002 (2014).
[10] G. Zheng, "Microscopy-Programmable LED array makes microscopes more versatile," Laser Focus World 48, 66 (2012).
[11] D. K. Hamilton and C. J. R. Sheppard, "Differential phase contrast in scanning optical microscopy," Journal of Microscopy 133, 27-39 (1984).
[12] X. Ou, R. Horstmeyer, C. Yang, and G. Zheng, "Quantitative phase imaging via Fourier ptychographic microscopy," Optics Letters 38, 4845-4848 (2013).
[13] S. Dong, K. Guo, P. Nanda, R. Shiradkar, and G. Zheng, "FPscope: a field-portable high-resolution microscope using a cellphone lens," Biomedical Optics Express 5, 3305-3310 (2014).
[14] S. Dong, R. Horstmeyer, R. Shiradkar, K. Guo, X. Ou, Z. Bian, H. Xin, and G. Zheng, "Aperture-scanning Fourier ptychography for 3D refocusing and super-resolution macroscopic imaging," Optics Express 22, 13586-13599 (2014).
[15] S. Dong, R. Shiradkar, P. Nanda, and G. Zheng, "Spectral multiplexing and coherent-state decomposition in Fourier ptychographic imaging," Biomedical Optics Express 5, 1757-1767 (2014).
[16] L. Tian, X. Li, K. Ramchandran, and L. Waller, "Multiplexed coded illumination for Fourier Ptychography with an LED array microscope," Biomedical optics express 5, 2376-2389 (2014).
[17] A. Williams, J. Chung, X. Ou, G. Zheng, S. Rawal, Z. Ao, R. Datar, C. Yang, and R. Cote, "Fourier ptychographic microscopy for filtration-based circulating tumor cell enumeration and analysis," Journal of Biomedical Optics 19, 066007-066007 (2014).
[18] G. Zheng, "Breakthroughs in Photonics 2013: Fourier Ptychographic Imaging," Photonics Journal, IEEE 6, 1-7 (2014).
[19] W. Choi, C. Fang-Yen, K. Badizadegan, S. Oh, N. Lue, R. R. Dasari, and M. S. Feld, "Tomographic phase microscopy," Nature methods 4, 717-719 (2007).
[20] R. Horstmeyer, X. Ou, J. Chung, G. Zheng, and C. Yang, "Overlapped Fourier coding for optical aberration removal," Optics Express 22, 24062-24080 (2014).

Chapter 9 Autofocusing for whole slide imaging system

In this chapter, we report the development of a high-throughput whole slide imaging (WSI) system by adapting a cost-effective optomechanical add-on kit to existing microscopes. Inspired by the phase detection concept in professional photography, we attached two pinhole-modulated cameras at the eyepiece ports for instant focal plane detection. By adjusting the positions of the pinholes, we can effectively change the view angle for the sample, and as such, we can use the translation shift of the two pinhole-modulated images to identify the optimal focal position. By using a small pinhole size, the focal-plane-detection range is on the order of millimeter, orders of magnitude longer than the objective's depth of field. We also show that, by analyzing the phase correlation of the pinhole-modulated images, we can determine whether the sample contains one thin section, folded sections, or multiple layers separated by certain distances - an important piece of information prior to a detailed z scan. In order to achieve system automation, we deployed a low-cost programmable robotic arm to perform sample loading and $14 stepper motors to drive the microscope stage to perform x-y scanning. Using a 20X objective lens, we can acquire a 2 gigapixel image with 14 mm by 8 mm field of view in 90 seconds. The reported platform may find applications in biomedical research, telemedicine, and digital pathology. It may also provide new insights for the development of high-content screening instruments.

9.1 Background

Whole slide imaging (WSI) system is one important tool for biomedical research and clinical diagnosis. In particular, the advances of computer and image sensor technologies in recent years have significantly accelerated the development of WSI systems for high-content screening,

telemedicine, and digital pathology. One important aspect of WSI systems is to maintain the sample at the optimal focal position over a large field of view. Autofocus method for WSI systems is still an active research area due to its great potentials in industrial and clinical applications. There are two main types of autofocus methods in WSI systems: 1) laser-reflection methods and 2) image-contrast-related method. For laser-reflection method [1–3], an infrared laser beam is reflected by the sample surface and creates a reference point for determining the distance between the surface and the objective lens. This method only works well for samples that have a fixed distance off the surface. If a sample varies its location from the surface, this method cannot maintain the optimal focal position. Different from the laser-reflection method, image-contrast-related method [2, 4–6] is able to track topographic variations and identify the optimal focal position through image processing. This method acquires multiple images by moving the sample along the z direction and calculates the focal position by maximizing a figure of merit (such as image contrast, entropy, and frequency content) of the acquired images. Since z-stacking increases the total scanning time, image-contrast-related method achieves better imaging performance by trading off system throughput. However, due to the topographic variation of pathology slides, most WSI systems employ image-contrast-related method for tracking the focus [2].

We developed a WSI platform by adapting an optomechanical add-on kit to a regular microscope. Inspired by the phase detection concept in professional photography [7], we attached two pinhole-modulated cameras at the eyepiece ports for focal plane detection. By adjusting the positions of the pinholes, we can effectively change the view angle through the two eyepiece ports. The focal position can be recovered by calculating the phase correlation of the corresponding pinhole-modulated images. There are several advantages of the reported platform: 1) By deploying a small-sized pinhole in both cameras, autofocusing can reach the millimeter range, orders of

magnitude longer than the objective's depth of field. On the other hand, conventional image-contrast-based method relies on the captured images from the main camera port, which will be blurred out if the sample is defocused by a long distance. 2) The two images captured by the pinhole-modulated cameras provide additional information of the sample's tomographic structure in the z direction. By analyzing the phase correlation curve, we can readily determine whether the sample contains one thin section, folded sections, or multiple layers separated by certain distances. Different z-sampling strategies can then be used in conjunction with the reported method for better image acquisition. For example, we can perform z-stacking for the area that contains folded sections or multiple layers. We can also avoid air burbles by comparing the layered structure with the surrounding areas. 3) One of the major barriers for the adoption of WSI system is the cost. In the reported platform, we used a cost-effective mechanical add-on kit to convert a regular microscope into a WSI system, making it affordable to small research labs. For each x-y position, the reported platform is able to directly move the stage to the optimal focal position; no z-stacking is needed and the focus error will not propagate to other x-y positions. 4) In the reported platform, we employed a cost-effective programmable robotic arm (uArm from Kickstarter) for sample loading. We can easily expand its capability for handling other samples (such as Petri dish) and integrate other image recognition strategies for better and affordable laboratory automation.

This chapter is structured as follows: in section 9.2, we will report the design and the operation principle of the pinhole-modulated camera. In section 9.3, we will report the use of the phase correlation curve for peeking the sample structure in the z direction. In section 9.4, we will report the design of the add-on kit for converting a conventional microscope into a WIS system. Finally, we will summarize the results and discuss the future directions in section 9.5.

9.2 Instant focal plane detection using pinhole-modulated cameras

Inspired by the phase detection concept in professional photography [7], we attached two pinhole-modulated cameras at the eyepiece ports for instant focal plane detection, as shown in Fig. 9-1(a), where the pinhole is inserted at the Fourier plane of the lens. By adjusting the positions of the two pinholes, we can effectively change the view angle of the sample. If the sample is placed at the in-focus position, the two captured images will be identical (Fig. 9-1(b2)). If the sample is placed at an out-of-focus position, the sample will be projected at two different view angles, causing a translational shift in the two captured images (Fig. 9-1(b1) and 9-1(b3)). The translation shift is proportional to the defocus distance of the sample. Therefore, by identifying the translational shift of the two captured images, we can recover the optimal focal position of the sample without a z-scan.

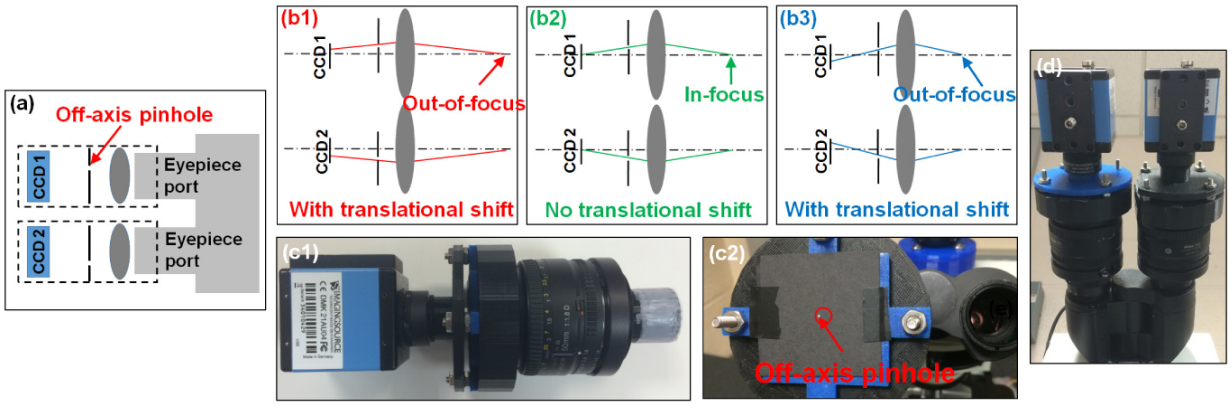

Figure 9-1: (a) Pinhole-modulated cameras for instant focal plane detection. (b) By inserting an off-axis pinhole at the Fourier plane, we can effectively change the view angle of the sample. (c1) A 3D-printed plastic case was used to assemble the pinhole-modulated camera. (c2) The off-axis pinhole was punched by a needle on a printing paper. (d) We attached the assembly to the eyepiece ports of a microscope platform.

The design of the pinhole-modulated camera is shown in Fig. 9-1(c), where we used a 3D-

printed case to assemble a 50 mm Nikon photographic lens (f/1.8), a pinhole, and a CCD detector. We used a needle to punch a hole on a printing paper, as shown in Fig. 9-1(c2). The size of the pinhole is ~0.5 mm, and it locates at ~1.5 mm away from the optical axis. To adjust the position of the pinhole, we increase the off-axis distance until the image vanishes in the camera. The whole module was attached to the eyepiece ports of a microscope (Fig. 9-1(d)).

Figure 9-2 shows the experimental characterization of the instant focal plane detection scheme. By putting the sample at different positions, we can see different translational shift from the two pinhole-modulated images (Fig. 9-2(a) and 9-2(b)). The images captured at the main camera port are shown in Fig. 9-2(c) as a comparison. We can see that, the depth of field of the pinhole modulated images is orders of magnitude longer than that of the high-resolution image captured through the main camera port. Figure 9-2(d) shows the measured relationship between the translational shift and the defocus distance of the sample. For imaging new samples, we first identify the translational shift of the two pinhole-modulated images and then use this calibration curve to recover the focal position.

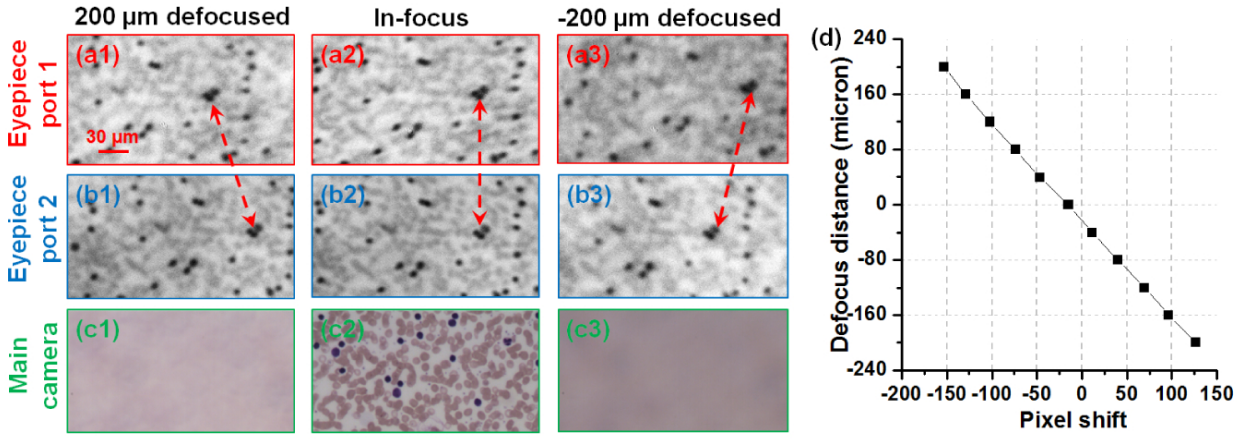

Figure 9-2: The captured images through the pinhole-modulated cameras (a)-(b), and the main camera (c). (d) The measured relationship between the translational shift of the two pinhole-modulated images and the defocus distance.

9.3 Unveiling sample's tomographic structure using the phase correlation curve

In the reported platform, we used phase correlation to identify the translational shift of the two pinhole-modulated images. The use of phase correlation for subpixel registration is an established technique in image processing [8]. We explore the use of phase correlation curve to peek the sample's tomographic structure without a detailed z-scan.

Figure 9-3 demonstrates that, different samples have different characteristics on the phase correlation curves. A thin section renders a single sharp peak (Fig. 9-3(a)) while a sample with folded sections has a peak with a boarder full width at half maximum (FWHM) (Fig. 9-3(b)). For samples with multiple layers, we can see multiple peaks from the curve, as shown in Fig. 9-3(c). In particular, in Fig. 9-3(c), the two layers are separated by 100 μm. The reported platform is able to recover this information over such a long depth of field. The sample information along the z direction is valuable for determining the sampling strategy. For example, we can perform multilayer sampling according to the peaks or the FWHM of the phase correlation curve. Further research is needed to relay the phase correlation characteristics with the sample property [9]. In the reported platform, we simply identify the maximum point of the phase correlation curve to recover the focal position of the sample; no z-scanning was used.

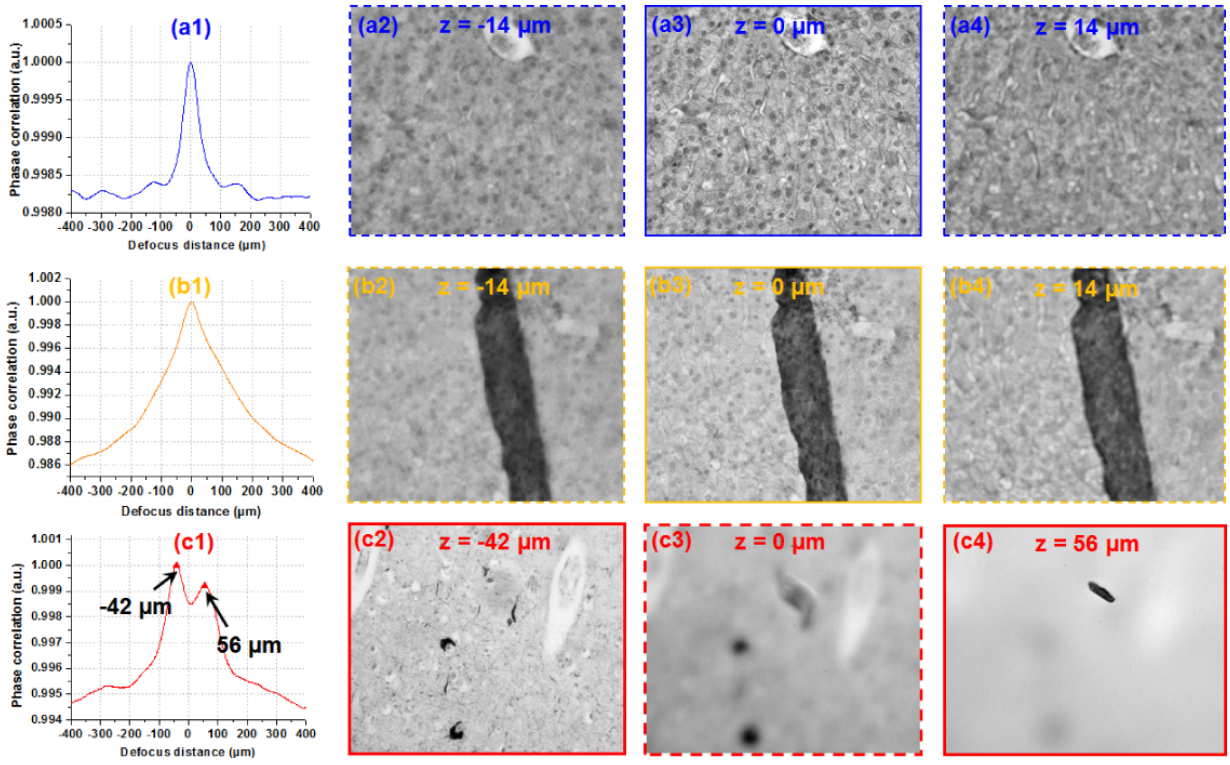

Figure 9-3: Using the phase correlation curve for exploring sample structures at the z direction. Samples with one thin section (a), folded section (b), and two different layers separated by certain distance (c).

9.4 Mechanical design and high-throughput gigapixel imaging

In order to achieve system automation, we used a low-cost programmable robotic arm (uArm, Kickstarter) to perform sample loading and stepper motors (NEMA-17, Adafruit) to drive the microscope stage to perform x-y-z scanning. In our implementation, we used 3D-printed plastic gears to control the focus knob for sample autofocusing, as shown in Fig. 9-4(a). The smallest z-step is 350 nm in our design. If needed, one can change the size ratio of the two mechanical gears in Fig. 9-4(a) to achieve a better z resolution. Figure 9-4(b) shows the mechanical add-on kit for controlling sample scanning in x-y plane and the programmable robotic arm for automatic sample loading. We used Arduino microcontroller to control the scanning process.

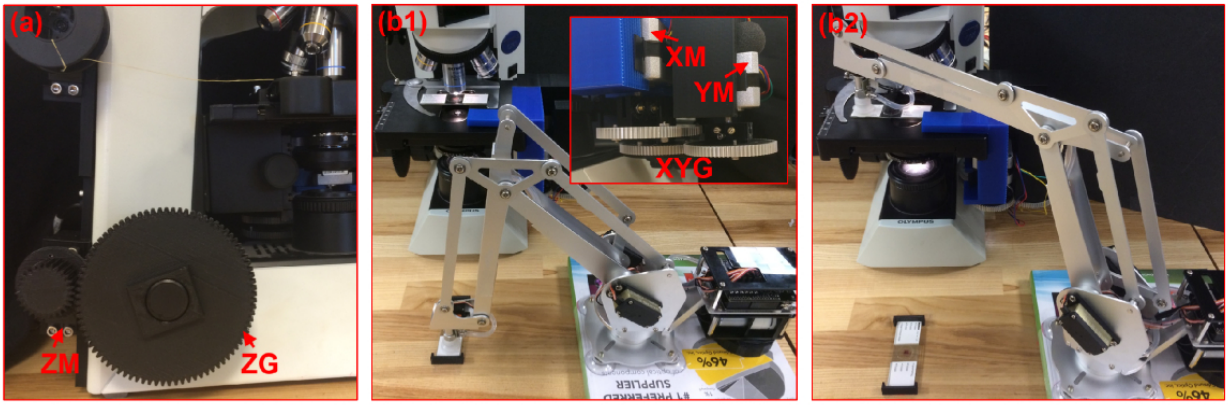

Figure 9-4: Sample loading and mechanical scanning schemes in the reported platform. (a) 3D-printed plastic gear for controlling focus knob. (b) Sample scanning using a mechanical kit and sample loading using a programmable robotic arm. XM: x-axis motor; YM: y-axis motor; XYG: x-y scanning gear group; ZM: z-axis motor; ZG: z-axis scanning gear.

Figure 9-5 shows the gigapixel images captured using the reported platform. In Fig. 9-5(a), we used a 9 megapixel monochromatic CCD camera (Prosilica GT 34000, 3.69 μm pixel size) to capture a pathology slide. Using a 20X, 0.75 numerical aperture objective lens, it took 90 seconds to acquire a 2 gigapixel image with 14 mm by 8 mm field of view. This image contains 340 segments, and the image acquisition of each segment takes ~0.24 second using a regular desktop computer with an Intel i5 processor. The detailed breakdown of the acquisition time is as follow: 1) 0.1 second for the pinhole-modulated cameras to acquires two images from the eyepiece ports; 2) 0.02 second for the calculation of the phase correlation and recover the optimal focal position; 3) 0.04 second to drive the focus knob; 4) 0.02 second to trigger the main camera to capture the high-resolution in-focus image; 5) 0.06 second to drive the x-y stage to another positon. The main speed limitation is located at the data readout from pinhole-modulated cameras. In this early prototype, we used an old camera model (31AU03, IC Capture, 1024 by 768 pixels). A CMOS webcam with faster data readout can reduce the acquisition time of single segment to 0.16 second

(~40% improvement). In Fig. 9-5(b), we use a 1.5 megapixel color CMOS camera (Infinity lite, 4.2 µm pixel size) to acquire a color image of blood smear. The total acquisition time is 16 minutes and the field of view is 15 mm by 15 mm with 2400 segments. The longer acquisition time is caused by the detector size being much smaller than the CCD used in Fig. 9-5(a) and the absence of hardware triggering.

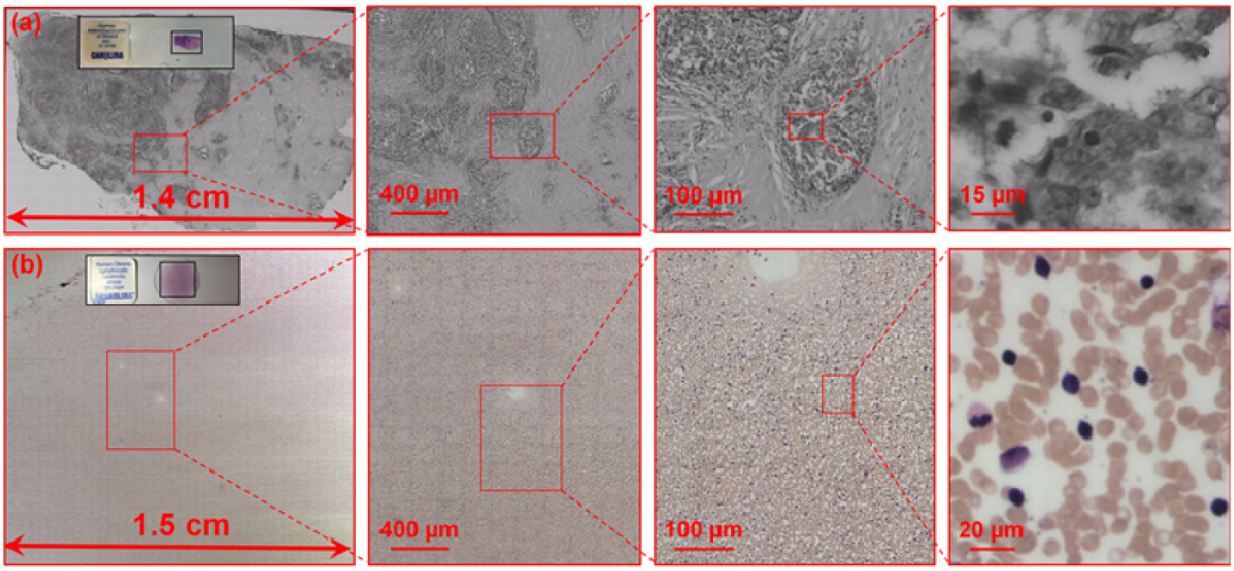

Figure 9-5: Gigapixel images captured by using the reported platform. (a) A captured image of a pathology slide using a 9 megapixel CCD. The field of view is 14 mm by 8 mm and the acquisition time is 90 seconds. (b) A captured image of a blood smear using a 1.5 megapixel color CMOS sensor. The field of view is 15 mm by 15 mm and the acquisition time is 16 minutes.

To test the autofocusing capability, we have also moved the sample to 25 pre-defined z-positions and used the reported approach to recover the z-positions. The standard deviation between the ground truth and our recovery is ~300 nm, much smaller than the depth of field of the employed objective. Finally, we note that, the use of stepper motor to drive microscope is not a new idea [6]; however, integrating it with the proposed autofocusing scheme for high-throughput WSI is new and may find various biomedical applications.

9.5 Discussion

We have demonstrated the use of pinhole-modulated camera for instant focal plane detection. We have developed a WSI add-on kit to convert a regular microscope to a WSI system. For each x-y position, the reported WSI platform is able to directly move the stage to the optimal focal position; no z-stacking in needed for focal plane searching and the focus error will not be accumulated to other x-y positions. By using the reported platform, we demonstrated the acquisition of a 2 gigapixel image (14 mm by 8 mm) in 90 seconds. Compared to laser reflection methods, the reported approach is able to track the topographic variations of the tissue section; neither external laser source nor angle-tracking optics is needed. Compared to image-contrast methods, the reported approach has an ultra-long autofocusing range and requires no z-scanning for focal plane detection. From the cost point of view, the mechanical kit, including the stepper motor and related drivers, costs ~$50 (Amazon). The camera lens at the eyepiece port can be replaced by low-cost eyepiece adapter with 0.5X reduction lens (~$25, Amscope). The pinhole can be inserted into the Fourier plane of the reduction lens. Lastly, we can use low-cost stereo Minoru webcam (~$20, Amazon) or other low-cost webcams at the eyepiece port to capture the pinhole-modulated images. The rest of system remains the same as the regular microscope. The reported design may enable the dissemination of high-throughput imaging/screening instruments for the broad biomedical community. It can also be directly combined with other cost-effective imaging schemes for high-throughput multimodal microscopy imaging [10, 11].

There are several areas we plan to improve in the next phase: 1) due to the large data set we acquire, we use a free software (Image Composite Editor) to perform image stitching off-line. We need to convert the captured data into individual images and manually upload them to the software. The software blindly stitches the image without making use of positional information of individual segments. The entire process takes about 40 minutes for generating the image shown in Fig. 9-5(a).

We plan to develop a memory efficient program to perform stitching during the image acquisition process. 2) The current speed limitation comes from data readout from the pinhole-modulated cameras (15 fps). A camera with higher frame rate can be used to further shorten the acquisition time by 40%. The sensor area and the total number of pixels of the pinhole-modulated camera are not important in reported approach. 3) We used plastic cases in various parts of our prototype to mount the pinhole-modulated camera. Due to the weights of the cameras, stability is a concern for the reported prototype. A metal mount with better optomechanical design is needed in the future (for example, using the commercially available eyepiece adapter with 0.5X reduction lens). 4) The reported method can be used for fluorescence imaging. In this case, the photon budget for the pinhole modulated cameras will be low. We may need to study the effect of shot noise for the phase correlation curve. 5) The use of phase correlation curve for peeking sample's tomographic structures is an unexplored area. Further research is needed to study the phase correlation characteristics and the associated sample properties. 6) In the reported platform, we employed a programmable robotic arm for sample loading. The use of robotic arm for sample loading is not a new idea. However, low-cost and open-source robotic arms are only available very recently. We can expand their capability for handling different samples and integrate other image recognition strategies for better and affordable laboratory automation.

Bibliography

[1] Y. Liron, Y. Paran, N. G. Zatorsky, B. Geiger, and Z. Kam, "Laser autofocusing system for high-resolution cell biological imaging," J. Microsc. 221(2), 145–151 (2006).
[2] M. C. Montalto, R. R. McKay, and R. J. Filkins, "Autofocus methods of whole slide imaging systems and the introduction of a second-generation independent dual sensor scanning method," J. Pathol. Inform. 2(1), 44 (2011).
[3] C.-S. Liu, P.-H. Hu, Y.-H. Wang, S.-S. Ke, Y.-C. Lin, Y.-H. Chang, and J.-B. Horng, "Novel fast laser-based auto-focusing microscope," in Sensors, 2010 IEEE, (IEEE, 2010), 481–485.

[4] S. Yazdanfar, K. B. Kenny, K. Tasimi, A. D. Corwin, E. L. Dixon, and R. J. Filkins, "Simple and robust image-based autofocusing for digital microscopy," Opt. Express 16(12), 8670–8677 (2008).
[5] L. Firestone, K. Cook, K. Culp, N. Talsania, and K. Preston Jr., "Comparison of autofocus methods for automated microscopy," Cytometry 12(3), 195–206 (1991).
[6] L. McKeogh, J. Sharpe, and K. Johnson, "A low-cost automatic translation and autofocusing system for a microscope," Meas. Sci. Technol. 6(5), 583–587 (1995).
[7] A. Kinba, M. Hamada, H. Ueda, K. Sugitani, and H. Ootsuka, "Auto focus detecting device comprising both phase-difference detecting and contrast detecting methods," (Google Patents, 1997).
[8] H. Foroosh, J. B. Zerubia, and M. Berthod, "Extension of phase correlation to subpixel registration," IEEE Trans. Image Process. 11(3), 188–200 (2002).
[9] A. A. S. Awwal, "What can we learn from the shape of a correlation peak for position estimation?" Appl. Opt. 49(10), B40–B50 (2010).
[10] G. Zheng, C. Kolner, and C. Yang, "Microscopy refocusing and dark-field imaging by using a simple LED array," Opt. Lett. 36(20), 3987–3989 (2011).
[11] K. Guo, Z. Bian, S. Dong, P. Nanda, Y. M. Wang, and G. Zheng, "Microscopy illumination engineering using a low-cost liquid crystal display," Biomed. Opt. Express 6(2), 574–579 (2015).